

1 The Electron-Ion Scattering experiment ELISe at the
2 International Facility for Antiproton and Ion Research
3 (FAIR) - a conceptual design study

4 A.N. Antonov, M.K. Gaidarov, M.V. Ivanov, D.N. Kadrev

5 *INRNE-BAS Sofia - Bulgaria*

6 M. Aïche, G. Barreau, S. Czajkowski, B. Jurado

7 *Centre d'Etudes Nucléaires Bordeaux-Gradingnan (CENBG) - France*

8 G. Belier, A. Chatillon, T. Granier, J. Taieb

9 *CEA Bruyères-le-Châtel - France*

10 D. Doré, A. Letourneaux, D. Ridikas, E. Dupont, E. Berthoumieux,
11 S. Panebianco

12 *CEA Saclay - France*

13 F. Reymund, C. Schmitt

14 *GANIL Caen - France*

15 L. Audouin, E. Khan, L. Tassan-Got

16 *IPN Orsay - France*

17 T. Aumann, P. Beller[†], K. Boretzky, A. Dolinskii, P. Egelhof, H. Emling,
18 B. Franzke, H. Geissel, A. Kelic-Heil, O. Kester, N. Kurz, Y. Litvinov,
19 G. Münzenberg, F. Nolden, K.-H. Schmidt, H. Simon, M. Steck, H. Weick

20 *GSI Darmstadt - Germany*

21 J. Enders, N. Pietralla, A. Richter, G. Schrieder

22 *TU Darmstadt - Germany*

23 A. Zilges

24 *University of Cologne - Germany*

25 M.O. Distler, H. Merkel, U. Müller

26 *Johannes Gutenberg University of Mainz - Germany*

27 A. Junghans

28 *FZ Dresden - Germany*

Email address: H.Simon@gsi.de (H. Simon)

29
30
31
32
33
34
35
36
37
38
39
40
41
42
43
44
45
46
47
48
49
50
51
52
53
54
55
56
57
58
59

H. Lenske

Justus-Liebig University Giessen - Germany

M. Fujiwara

RCNP Osaka - Japan

T. Suda

RIKEN - Japan

S. Kato

Yamagata University - Japan

T. Adachi, S. Hamieh, M.N. Harakeh, N. Kalantar-Nayestanaki, H. Wörtche

KVI, University of Groningen - The Netherlands

G.P.A. Berg

KVI, University of Groningen - The Netherlands &

Department of Physics and JINA, University of Notre Dame , USA

I.A. Koop, P.V. Logatchov, A.V. Otboev, V.V. Parkhomchuk, D.N. Shatilov,
P.Y. Shatunov, Y.M. Shatunov, S.V. Shiyankov, D.I. Shvartz, A.N. Skrinsky

BINP Novosibirsk - Russia

L.V. Chulkov, B.V. Danilin[†], A.A. Korshennikov, E.A. Kuzmin,
A.A. Ogloblin, V.A. Volkov

RRC Kurchatov Institute Moscow - Russia

Y. Grishkin, V.P. Lisin, A.N. Mushkarenkov, V. Nedorezov, A.L. Polonski,
N.V. Rudnev, A.A. Turlin

INR Moscow - Russia

A. Artukh, S.N. Ershov, A. Fomichev, M. Golovkov, A.V. Gorshkov,
L. Grigorenko, S. Klygin, S. Krupko, I.N. Meshkov, A. Rodin, Y. Sereda,
I. Seleznev, S. Sidorchuk, E. Syresin, S. Stepantsov, G. Ter-Akopian,
Y. Teterev, A.N. Vorontsov

JINR Dubna - Russia

S.P. Kamerdzhiev, E.V. Litvinova

IPPE Obninsk - Russia

S. Karataglidis

Rhodes University - Faculty of Science - South Africa

60 R. Alvarez Rodriguez, M.J.G. Borge, C. Fernandez Ramirez, E. Garrido,
61 P. Sarriguren, J.R. Vignote

62 *CSIC Madrid - Spain*

63 L.M. Fraile Prieto, J. Lopez Herraiz, E. Moya de Guera, J. Udias-Moinelo

64 *Complutense University of Madrid - Spain*

65 J.E. Amaro Soriano, A.M. Lallena Rojo

66 *Granada University - Spain*

67 J.A. Caballero

68 *Seville University - Spain*

69 H.T. Johansson, B. Jonson, T. Nilsson, G. Nyman, M. Zhukov

70 *Chalmers University of Technology - Sweden*

71 V. Avdeichikov

72 *Lund University - Sweden*

73 K. Hencken, J. Jourdan, B. Krusche, T. Rauscher, D. Kiselev, D. Trautmann

74 *University of Basel - Switzerland*

75 J. Al-Khalili, W. Catford, R. Johnson, P. Stevenson

76 *University of Surrey - United Kingdom*

77 C. Barton, D. Jenkins

78 *University of York - United Kingdom*

79 R. Lemmon

80 *CCLRC Daresbury - United Kingdom*

81 M. Chartier

82 *University of Liverpool - United Kingdom*

83 D. Cullen

84 *University of Manchester - United Kingdom*

85 C.A. Bertulani

86 *Texas A&M University Commerce - USA*

87 A. Heinz

88 *Yale University - USA*

89 **Abstract**

The electron-ion scattering experiment ELISe is part of the installations envisaged at the new experimental storage ring at the international Facility for Antiproton and Ion Research (FAIR) in Darmstadt, Germany. It offers a unique opportunity to use electrons as probe in investigations of the structure of exotic nuclei. The conceptual design and the scientific challenges of ELISe are presented.

90 *Keywords:* eA collider, electron scattering, nuclei far off stability

91 *PACS:* 29.27.-a, 25.30.Bf, 25.30.Dh, 21.10.Ft, 29.20.Dh, 29.30.-h

92 **1. Introduction**

93 The Facility for Antiproton and Ion Research (FAIR) is scientifically and
94 technically one of the most ambitious projects worldwide. It has a broad sci-
95 entific scope allowing forefront research in different sub-disciplines of physics.
96 Because of its great potential for discoveries, the FAIR project has been given
97 highest priority in the NuPECC Long-Range Plan 2004 [1]. One of the sci-
98 entific pillars of FAIR is nuclear-structure physics and nuclear astrophysics with
99 radioactive ion beams. The proposed electron-ion collider (eA Collider) con-
100 sisting of the New Experimental Storage Ring (NESR) and the Electron and
101 Antiproton Ring (EAR) will allow a range of novel studies with stored and
102 cooled beams.

103 The use of electrons as probe provides a powerful tool for examining nuclear
104 structure. The most reliable picture of nuclei originates in electron scatter-
105 ing. The increasing number of publications devoted to theoretical treatments of
106 electron scattering off exotic nuclei [2, 3, 4, 5, 6, 7, 8, 9, 10, 11, 12, 13, 14] sup-
107 ports this assertion and underlines the usefulness of an electron-ion scattering
108 setup for unstable nuclei. However, up to now, this technique is still restricted
109 to stable isotopes. The Electron-Ion Scattering experiment (ELISe) aims at
110 an extension of this powerful method to radioactive nuclei outside the valley
111 of stability. ELISe will be a unique and unprecedented tool for precise mea-
112 surements of nuclear-charge distributions, transition charge and current matrix
113 elements, and spectroscopic factors. This capability will contribute to a variety
114 of high-quality nuclear-structure data that will become available at FAIR.

115 A first technical proposal for an electron-ion collider was made almost twenty
116 years ago at the Joint Institute for Nuclear Research (Dubna) [15]. The ideas
117 of this proposal have been incorporated in and further developed at the RIKEN
118 Rare-Isotope Beam Factory (RIBF) for the so-called Multi-USE Experimental
119 Storage rings (MUSES) [16], as well as at the planned eA collider at FAIR,
120 under the name ELISe [17, 18, 19, 20, 21]. However, none of these projects
121 has been realized up to now. For the RIBF, an alternative setup called SCRIT
122 (Self-Contained Radioactive Ion Target) has been proposed [22]. In SCRIT a

123 circulating beam of electrons scatters off ions stored in a trap. Within foresee-
124 able future, ELISe could be the first and only eA collider for radioactive ion
125 beams worldwide. The ELISe setup provides easy access to different types of
126 electron-nucleus reactions in experiments where scattered electrons are detected
127 in coincidence with reaction products.

128 A cooled beam consisting of radioactive ions stored in the NESR will be
129 brought to collision with an intense electron beam circulating in EAR at the
130 interaction point (IP). Here, a magnetic spectrometer for the detection of scat-
131 tered electrons as well as detector systems for the measurements of reaction
132 products are to be installed.

133 This paper is organized as follows. It describes the physics case for ELISe and
134 explains the conditions and requirements for performing different experiments.
135 We explain the difference between fixed target and colliding beam kinematics
136 and outline the planned design and predicted performance of the eA collider.
137 The major components of ELISe, being planned as multi-purpose setup for these
138 experiments, i.e. an electron and in-ring spectrometer, as well as a luminosity
139 monitor, are characterized and viable concepts for their design are presented.

140 **2. Research objectives**

141 The central goal in nuclear physics is the construction of a theoretical frame-
142 work capable of describing consistently all nuclear systems from the deuteron
143 two-body case to infinite nuclear matter, going through every finite nucleus
144 with its many degrees of freedom and modes of excitation and decay. This
145 ambition is also the driving force for experimental investigations of nuclei near
146 the limits of stability. In the past two decades, substantial progress towards
147 this goal has been made due to the progress in developments of radioactive
148 beams. Intensive studies of the structure of nuclei near the drip lines are car-
149 ried out at several laboratories as GSI in Darmstadt (Germany), GANIL in
150 Caen (France), ISOLDE at CERN (Switzerland), JINR in Dubna (Russia),
151 NSCL at Michigan State University (USA) and RIKEN (Japan). The studies
152 involve nucleus-nucleus or nucleon-nucleus interactions as well as decay studies
153 and different means to determine their ground state properties. Building on
154 the great progress in the experimental and theoretical investigations (see, for
155 example, the reviews [23, 24]), novel experimental methods and observables will
156 most certainly enhance the opportunities leading to a better understanding of
157 the structure of nuclei near the limits of stability and in general.

158 Electron scattering, as in ELISe, offers unique and widely recognized ad-
159 vantages for the study of nuclear structure (see reviews [25, 26, 27, 28, 29]).
160 Interactions with electrons are well described by the most accurate theory in
161 physics - quantum electrodynamics (QED). The coupling is weak, so that mul-
162 tiple scattering effects are strongly suppressed, such that perturbations of the
163 initial state of the nucleus are minimal. The ability to vary momentum and
164 energy transferred to the nucleus, independently, allows mappings of spatial dis-
165 tributions of the constituent particles. Since electrons are point particles, they
166 offer excellent spatial resolution, and can additionally be tuned to the scale of a

167 process under study. Electron scattering, as it will be performed at ELISE, will
 168 thus add important new observables to investigate radioactive nuclear species.

169 To mention selected physics aspects (see also Table 1), these experiments
 170 will give access to

- 171 • charge-density distributions, in particular root-mean-square (r.m.s.) radii,
 172 of exotic nuclei from elastic electron scattering,
- 173 • new specific collective modes of excitation with selectivity to multipolarities
 174 via inelastic electron scattering, and
- 175 • internal nucleon-nucleon correlations and nuclear structure from quasi-free
 176 scattering, such as nucleon ($e, e'N$) or cluster ($e, e'c$) knockout.

177 *2.1. Elastic electron scattering: charge density distributions, charge radii*

178 Neglecting Coulomb distortion, i. e. in first order Born approximation (BA),
 179 the cross section for the scattering of an electron off a nucleus is given by

$$d\sigma/d\Omega = d\sigma/d\Omega_{\text{Mott}} F^2(q). \quad (1)$$

180 Here $d\sigma/d\Omega_{\text{Mott}}$ is the cross section in BA for the scattering off a point nu-
 181 cleus with spin zero and $F(q)$ is the form factor, which contains the information
 182 about the nuclear charge distribution $\rho(r)$. To be specific: The form factor is
 183 the Fourier transform of the latter.

184 Since BA is not sufficiently precise for the scattering off nuclei with larger Z ,
 185 the cross section has to be calculated by solving the Dirac equation numerically
 186 with the Coulomb potential from $\rho(r)$, for which an ansatz has to be made for
 187 this purpose. The common method is the calculation of the phase shifts of the
 188 electron wave in the Coulomb potential of $\rho(r)$ [30], it is therefore called "phase
 189 shift" or, thinking of the distorted electron waves, "DW" method.

190 The charge distribution is determined from measured cross sections by fitting
 191 the free parameters of the ansatz for $\rho(r)$ to the data. Several aspects of the
 192 information gained by such experiment are easier to catch by looking at the
 193 form factor (some details of how one gets it will be discussed in section 4.2).

194 The existing information on charge densities obtained from electron scatter-
 195 ing experiments for more than 300 nuclides is reviewed in [31, 32]. These data,
 196 confined to the valley of stability, show oscillations in r.m.s. radii, surface thick-
 197 nesses, and interior densities as a function of atomic number [33, 34]. The r.m.s.
 198 charge radius, can be extracted in a model-independent way from experimental
 199 data at low q from the expansion

$$F_{\text{ch}}(q) \sim 1 - \frac{\langle r^2 \rangle}{3!} q^2 + \frac{\langle r^4 \rangle}{5!} q^4 + \dots \quad (2)$$

200 The surface thickness, defined as the distance where $\rho_{\text{ch}}(r)$ drops from 90% to
 201 10% of its central value, is also accessible from the extracted form factor. For
 202 unstable nuclei, no data on the shapes of the nuclear surfaces exist, and here
 203 ELISE could provide a first insight. A central-density depression was observed

204 in several nuclei [35], even including light nuclei [36]. Such a depression is pre-
 205 dicted for proton-rich [12, 14] and superheavy [37, 38, 39] nuclei. The origin of
 206 this is due to Coulomb effect, the underlying shell and single particle structure
 207 as well as short-range correlations (see for example Ref. [35, 40] and references
 208 therein). The systematics of the charge-density distributions with the inclusion
 209 of nuclei having extreme proton-neutron asymmetry forms a basis for investiga-
 210 tions addressing both the structure of nuclei and the properties of bulk nuclear
 211 matter. An example of the latter is the determination of nuclear compressibility
 212 from experimental nuclear radii and binding energies [41].

213 The most realistic description of elastic electron-scattering cross sections can
 214 be achieved by solving the Dirac equation, and performing an exact phase-shift
 215 analysis [30]. This method has been chosen, e.g. in Ref. [7]. Using the DW
 216 method, the modulus of the charge form factor can be determined from the
 217 differential cross section. Its sensitivity to changes in the charge distribution
 218 is demonstrated in Fig. 1, taken from Ref. [7], where Ni isotopes are shown
 219 as example. The proton densities presented in Fig. 1 were obtained from self-
 220 consistent HF+BCS mean-field calculations with effective NN interactions in
 221 a large harmonic-oscillator basis [42] by using a density-dependent Skyrme pa-
 222 rameterization. In the same figure, the squared moduli of charge form factors,
 223 which are obtained from solving the Dirac equation numerically, are presented.
 224 Following this prescription, electron scattering is computed in the presence of a
 225 Coulomb potential induced by the charge distribution of a given nucleus. The
 226 intrinsic charge distribution of the neutron is included into these calculations.
 227 Two codes were used for the numerical evaluation of the form factors: the first is
 228 taken from Ref. [43] which follows Ref. [30] and the second has been discussed in
 229 Ref. [44]. The results of both calculations were found to be in good agreement.
 230 The nuclear charge form factor $F_{ch}(q)$ has been calculated as follows

$$F_{ch}(q) = \left[F_{point,p}(q)G_{Ep}(q) + \frac{N}{Z}F_{point,n}(q)G_{En}(q) \right] F_{c.m.}(q), \quad (3)$$

231 where $F_{point,p}(q)$ and $F_{point,n}(q)$ denote the form factors related to the point-like
 232 proton and neutron densities $\rho_{point,p}(\mathbf{r})$ and $\rho_{point,n}(\mathbf{r})$, respectively [7]. These
 233 densities correspond to wave functions where the positions \mathbf{r} of the nucleons are
 234 defined with respect to the center of the potential in the laboratory system. In
 235 order to let $F_{ch}(q)$ correspond to the density distributions in the center-of-mass
 236 coordinate system, a factor $F_{c.m.}(q)$ is introduced (e.g. [45, 46, 47]) in two
 237 commonly used ways:

$$F_{c.m.}(q) = e^{(qR)^2/6A}, \quad (4)$$

238 where R stands for the root-mean square radius of the nucleus, or

$$F_{c.m.}(q) = e^{(qb)^2/4A}, \quad (5)$$

239 where b denotes the harmonic-oscillator parameter. For shell-model potentials
 240 different from harmonic-oscillator, Eqs. (4) and (5) are approximations.

241 Equation (3) with a c.m. correction of form (4) [47] was used to compute
 242 the modulus squared of the form factor that can be extracted also from experi-
 243 mental data. In Eq. (3) $G_{Ep}(q)$ and $G_{En}(q)$ denote Sachs proton and neutron
 244 electric form factors, respectively, and are taken from one of the most recent
 245 phenomenological parameterizations [48]. Actually, there is no significant differ-
 246 ence between this recent parameterization and the most traditional one of
 247 Refs. [49, 50, 51] for the momentum-transfer range considered in this work
 248 ($q < 4 \text{ fm}^{-1}$).

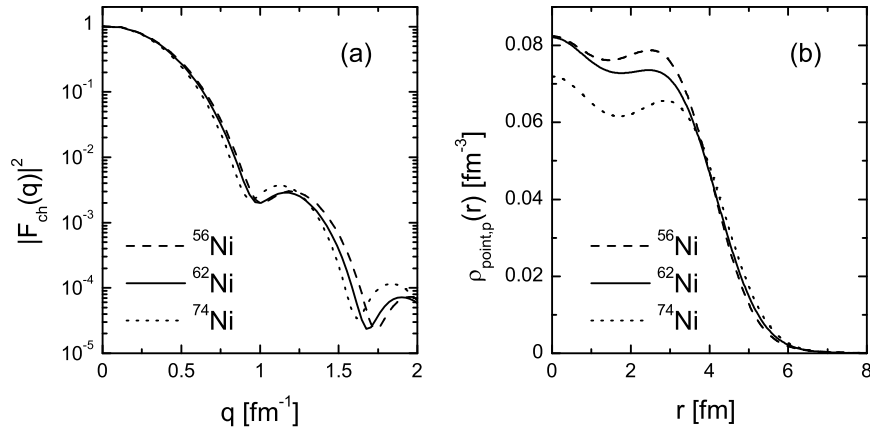


Figure 1: Modulus squared of charge form factors (panel (a)) calculated by solving the Dirac equation with HF+BCS proton densities (panel (b)) for the unstable doubly-magic ^{56}Ni , stable ^{62}Ni and unstable ^{74}Ni isotopes [7]. In the calculation of the moduli, the intrinsic charge distribution of the neutron was taken into account; see text for more details.

249 In general, it has been found that with increasing number of neutrons in a
 250 given isotopic chain the the minima of the curves of the charge form factor are
 251 shifted towards smaller values of the momentum transfer [7]. This is due mainly
 252 to the enhancement of the proton densities in the peripheral region and to a
 253 minor extent to the contribution from the charge distribution of the neutrons
 254 themselves. By accounting for the Coulomb distortion of the electron waves, a
 255 filling of the Born zeros is observed when the DW method is used (in contrast
 256 to plane-wave Born approximation).

257 As evident from Eq. (2), the r.m.s. radius is accessible from measurements
 258 at very low q -values where the cross sections are large. An accurate determi-
 259 nation of the charge distributions to e.g. extract the surface thickness from
 260 measured differential cross sections, requires a high precision measurement in a
 261 wide region of transferred momentum, at least up to the second maximum. As
 262 a further example, we quote the formation of so-called bubbles in exotic nuclei
 263 as discussed in Ref. [12], where the depletion of the central part of the charge
 264 distribution is attributed to a depopulation of s -states. It is also argued that

265 cross-section measurements to the second form-factor minimum, already pro-
266 vide information on the depletion of the central density. The data obtainable
267 with ELISE can provide for the first time precise information on the charge dis-
268 tribution of radioactive nuclei through form-factor measurements. These data
269 could subsequently be used to benchmark theoretical models for the structure
270 of exotic nuclei.

271 *2.2. Inelastic scattering: giant resonances, decay channels, astrophysical appli-* 272 *cations*

273 Inelastic electron scattering has proven to be a powerful tool for studying
274 properties of excited states of nuclei, in particular their spins, parities, and
275 the strength and structure of the transition densities connecting the ground
276 and excited states (see e.g. Ref. [25]). Although important information also is
277 available from other types of experiments, as for example, hadron scattering,
278 pickup and transfer reactions, charge-exchange reactions, the electron-scattering
279 method has unique features. This is the only method which can be used to
280 determine the detailed spatial distributions of the charge transition densities
281 for a variety of single-particle and collective transitions. These investigations
282 provide a stringent test of the nuclear many-body wave functions [26, 27].

283 Due to its strong selectivity, collective and strong single-particle excitations
284 can be studied particularly well in electron scattering. Electric and magnetic
285 giant multipole resonances are of special interest, and several of them have been
286 discovered and studied using electron scattering (see Ref. [28] and references
287 therein).

288 When approaching the neutron drip-line, there is a characteristic increase in
289 the difference between neutron and proton density distributions. Apart from di-
290 rect measurements using elastic scattering as described in the last section, where
291 electron and hadron scattering results are combined to extract the neutron-skin
292 density distribution, also complementary indirect methods are available. The
293 difference in radii of the neutron and proton density distributions is accessi-
294 ble via studies of giant dipole resonances (GDR) by inelastic scattering of an
295 isoscalar probe or spin- dipole resonances by charge-exchange reactions. The
296 cross section of these processes strongly depends on the relative neutron-skin
297 thickness [52, 53]. This quantity is of great importance due to direct relations
298 between the neutron-skin thickness and properties of the nuclear matter EOS
299 such as the symmetry-energy coefficient and the nuclear incompressibility. The
300 energy of the isoscalar giant monopole-resonance can be used to deduce the
301 compressibility of nuclear matter, which is directly related to the curvature of
302 the EOS. Hence data from inelastic electron scattering can provide an independ-
303 ent test of this quantity in addition to those obtained from the nuclear radius
304 (elastic scattering) and the binding energy (see Ref. [41]). Magnetic dipole exci-
305 tations (M1) arise due to changes in the spin structure of the nucleus and orbital
306 angular motion of its constituents. Along with decay studies, the measured M1
307 distributions from electron scattering could provide information about the nu-
308 clear Gamow-Teller strength distribution. The latter is important for reliably
309 extracting inelastic neutrino-nucleus cross sections [54], which are important

310 in certain astrophysical scenarios, such as neutron stars or core-collapse super-
311 novae.

312 The low-energy dipole strength located close to the particle-emission thresh-
313 old is a general feature in many isospin-asymmetric nuclei [55]. This mode is
314 known as the Pygmy Dipole Resonance (PDR), and has been explained as being
315 generated by oscillations of weakly bound neutrons with respect to the isospin
316 symmetric core in neutron-rich nuclei (see Review [56]). Thus, in exotic nuclei
317 the PDR modes should be especially pronounced.

318 The origin of approximately one half of the nuclides heavier than iron ob-
319 served in nature is explained by the r-process. The existence of pygmy reso-
320 nances has important implications on theoretical predictions of radiative neutron-
321 capture rates in the r-process nucleosynthesis, and consequently on the calcu-
322 lated elemental abundance distribution in the universe. This was studied using
323 calculations and fits to the properties of neutron-rich nuclei involved in this
324 process [57]. The inclusion of the PDR increases the r-process abundance-
325 distributions for nuclei around $A = 130$ by about two orders of magnitude
326 (Fig. 6 in [57]) as compared with the case where only the GDR was taken into
327 account. The result of the calculations strongly depends on the competition
328 between the open decay channels.

329 In heavy nuclei, the r-process path is expected to be limited by fission, and
330 the fission process is treated only very schematically in network calculations.
331 Therefore electro-induced fission giving access to a multipole decomposition of
332 the fission cross sections will allow to refine models of the fission process, to
333 study the nuclear structure involved, and to serve as an improved input for r-
334 process calculations [58] since fission is one of the decay channels of the excited
335 nucleus. ELISE will be an ideal experiment for electro-fission studies. Mea-
336 surements of coincidences between the scattered electron and the nuclear decay
337 products represent the most powerful tool available for precise determinations
338 of multipole excitation functions even when the resonance strength is spread
339 over a wide excitation energy range [59]. The proton and neutron numbers of
340 fission fragments and their kinetic energies as a function of the excitation energy
341 can be determined. Such complete experimental information will enable, for the
342 first time, studies of the influences of neutron and proton shells as well as of
343 pairing correlations on fission dynamics. Also, fission barriers of exotic nuclei
344 can be determined precisely.

345 *2.3. Quasi-free scattering (QFS): shell structure, spectral functions, spectro-* 346 *scopic factors*

347 High-resolution exclusive ($e, e'p$) experiments offer the possibility to study
348 individual proton orbits [60, 61, 62]. In Ref. [61] the momentum distribution for
349 'single'-particle states were thus determined. These were fitted by combinations
350 of bound-state wave-functions generated in a Woods-Saxon potential. Thereby,
351 the r.m.s. charge radii and the depletion of the spectroscopic factors could be de-
352 termined. This can be used to observe knockout from regions inside the nucleus
353 with essentially different densities. The observed spectroscopic strength for va-
354 lence shells, obtained with ($e, e'p$) reactions, are surprisingly small, sometimes

355 by 30-50%, compared to values of shell model calculations. It is believed that
 356 this is due to effects of short-range correlations [63, 64]. For asymmetric nuclei
 357 neutron-proton interactions lead to a reordering of shells [65]. It is therefore
 358 important also to characterize deeper lying levels. Measured momentum dis-
 359 tributions will help to identify the angular momentum and quantum numbers
 360 of the involved shells. Effects of final-state interactions and meson-exchange
 361 currents can be substantially reduced by choosing parallel kinematics [67, 68].
 362 The quasi-free ($e, e' p$) scattering-condition $Q^2/2m\omega_0 \approx 1$ in the eA collider¹–
 363 where Q denotes the four momentum transfer and ω_0 the energy loss– can be
 364 realized already at moderately forward scattering angles between 50° and 60° .
 365 Exclusive measurements should therefore be possible for light elements, where
 366 the achievable luminosities are close to $10^{29} \text{ cm}^{-2}\text{s}^{-1}$, as will be shown later in
 367 this paper. Occupation probabilities and spectroscopic factors can be obtained
 368 in the region of resolved states. Another access to correlations in the nuclear
 369 interior is provided by cluster knock out ($e, e'c$) [3] that yields information on
 370 momentum distributions and cluster spectroscopic factors of clusters inside nu-
 371 clei.

372 In inclusive electron scattering in the quasi-free region, an average over all
 373 available orbits can be measured [66] by the shape of the obtained spectrum.
 374 Inclusive measurements are likely to be feasible for medium and heavy nuclei at
 375 achievable luminosities of $10^{28} \text{ cm}^{-2}\text{s}^{-1}$.

376 3. Kinematics of colliding beams

377 This section describes the kinematics of colliding beams and the design pa-
 378 rameters of the electron spectrometer. It is compared to a conventional labo-
 379 ratory system where the electron beam strikes a fixed target. The scattering
 380 process is described in a polar coordinate system with the axis along the elec-
 381 tron beam axis where the polar angle is the scattering angle θ . In the following,
 382 this system is referred to as kinematics F. The boosted center-of-mass (c.m.) of
 383 the colliding beams into the laboratory frame leads to kinematical conditions
 384 that are very different compared to conventional experiments.

385 The equations in this section are calculated in the limit of zero electron mass.
 386 In this limit the total energy of the electron is equal to its kinetic energy and
 387 momentum ($E_e = T_e = p_e$)². The numerical estimates given in this section
 388 assume counter-propagating i.e. colliding beams of 0.74 GeV/nucleon ions and
 389 0.5 GeV electrons (referred to as kinematics C). The energy of electrons in
 390 kinematics F corresponding to that of colliding beam kinematics in the c.m. is

¹For the simulation calculation (QFS on ^{12}C), going beyond the scope of this work, ω_0 was taken to be 135 MeV. Protons are then emitted in backward direction in a small cone with angles ranging from 160° to 165° . The required proton resolution for resolving states varies from about 1 % to 3 % at 300 MeV and 800 MeV, respectively. The $A - 1$ -Fragments fall within the acceptance of the in-ring spectrometer, described later in this paper.

²Natural units $c = 1$, $\hbar = 1$ are used in the following.

Table 1: Required luminosities for different studies. The achievable values predicted for the ELISE setup will be discussed in section 4 on page 14. The given values are based on rate estimates for – at most – 4 week measurements.

Reaction	Deduced quantity	Target nuclei	Luminosity $\text{cm}^{-2}\text{s}^{-1}$
elastic scattering at small q	r.m.s. charge radii	light medium	10^{24}
first minimum in elastic form-factor	density distribution with 2 parameters	light medium heavy	10^{28} 10^{26} 10^{24}
second minimum in elastic form-factor	density distribution with 3 parameters	medium heavy	10^{29} 10^{26}
giant resonances	position, width, strength, decays	medium heavy	10^{28} 10^{28}
quasi-elastic scattering	spectroscopic factors, spectral function, momentum distributions	light	10^{29}

391 given by

$$T_e(F) = \sqrt{\frac{1+\beta}{1-\beta}} T_e(C), \quad (6)$$

392 where $\beta = p_A/E_A$ is the ion velocity. Thus, a 0.5 GeV electron in kinematics C
393 corresponds to a 1.64 GeV electron in kinematics F.

394 Table 2 gives the kinematical equations for two types of kinematics for an
395 electron scattering experiment. It can be shown that while the energy of elasti-
396 cally scattered electrons in kinematics F is almost independent of the scattering
397 angle, the electron energy in kinematics C depends strongly on scattering angle
398 and increases from $p_{e'} = p_e$ to $p_{e'} \approx (1+\beta)/(1-\beta)p_e$ when the angle increases
399 from 0° to 180° , i.e. from 0.5 GeV at zero degree to ≈ 5 GeV in backward
400 direction. Furthermore, while in kinematics F the energy separation between
401 elastically and inelastically scattered electrons is approximately equal to the
402 excitation energy (E^*) of the recoiling ion, in kinematics C this separation is
403 reduced by a factor of $\sqrt{(1-\beta)/(1+\beta)} \approx 0.3$.

404 These two features of kinematics C make it difficult to resolve elastically and
405 inelastically scattered electrons³.

³Table 2 demonstrates that the separation between elastic and inelastic peaks in the spec-
trum is much larger in the case of co-propagating beams. However, several other parameters
are not in favor of this geometry. For example, the length \mathcal{L} of interaction zone (IZ) is deter-
mined by $\mathcal{L} \approx l/(1\pm\beta)$, where l is the ion-bunch length, + corresponds to counter-propagating
beams and – to co-propagating beams. For co-propagating beams $\mathcal{L} = 50$ cm, which is ten

Table 2: Kinematics of colliding beams. Here, p_e , $p_{e'}$ are the momenta of incoming and scattered electrons, θ is the electron scattering angle relative to the electron beam direction, $\beta = p_A/E_A$, $\delta = \sqrt{(1-\beta)/(1+\beta)}$, $E_A = \sqrt{M^2 + p_A^2}$ is the total energy of incident ions, and E^* the excitation energy of the recoil ion.

F	C
Conventional kinematics ($\beta = 0$)	Counter-propagating beams ($\beta > 0$)
Scattered electron momentum	
$p_{e'} = \frac{p_e - E^*}{1 + 2\frac{p_e}{M} \sin^2 \frac{\theta}{2}}$	$p_{e'} = \frac{p_e - \delta E^*}{1 + 2\frac{p_e - p_A}{M} \delta \sin^2 \frac{\theta}{2}}$
Momentum transfer	
$q^2 = \frac{4p_e^2 \sin^2 \frac{\theta}{2}}{1 + 2\frac{p_e}{M} \sin^2 \frac{\theta}{2}}$	$q^2 = \frac{4p_e^2 \sin^2 \frac{\theta}{2}}{1 + 2\delta\frac{p_e - p_A}{M} \sin^2 \frac{\theta}{2}}$
Resolution (momentum dependence)	
$\Delta E^* \approx - \left(1 + 2\frac{p_e}{M} \sin^2 \frac{\theta}{2} \right) \Delta p_{e'}$	$\Delta E^* \approx - \left(\frac{1}{\delta} + 2\frac{p_e - p_A}{M} \sin^2 \frac{\theta}{2} \right) \Delta p_{e'}$
Resolution (angular dependence)	
$\Delta E^* \approx - \frac{p_e p_{e'}}{M} \sin \theta \Delta \theta$	$\Delta E^* \approx - \frac{(p_e - p_A) p_{e'}}{M} \sin \theta \Delta \theta$

Table 3: Comparison of colliding beam and conventional fixed-target kinematics. Calculations were performed assuming counter-propagating beams of 0.74 GeV/nucleon ^{50}Co and 0.5 GeV electrons. In fixed-target kinematics this is equivalent to a 1.642 GeV electron beam. Here, θ and $p_{e'}$ are the scattering angle and the scattered-electron momentum. The quantities $\frac{\partial E^*}{\partial \theta} \Delta \theta$ and $\frac{\partial E^*}{\partial p} \Delta p$ show the sensitivity of the excitation energy determination to the uncertainties in the scattering angle and in the scattered-electron momentum ($\Delta \theta = 1$ mrad and $\frac{\Delta p}{p} = 10^{-4}$).

q GeV/c	Kinematics C				Kinematics F			
	θ deg.	$p_{e'}$ GeV/c	$\frac{\partial E^*}{\partial \theta} \Delta \theta$ MeV	$\frac{\partial E^*}{\partial p} \Delta p$ MeV	θ deg.	$p_{e'}$ GeV/c	$\frac{\partial E^*}{\partial \theta} \Delta \theta$ MeV	$\frac{\partial E^*}{\partial p} \Delta p$ MeV
0.1	11.4	0.504	0.15	-0.16	3.5	1.642	-0.004	-0.16
0.2	22.7	0.518	0.30	-0.16	7.0	1.642	-0.007	-0.16
0.3	33.5	0.540	0.44	-0.16	10.5	1.642	-0.010	-0.16
0.4	43.9	0.572	0.59	-0.16	14.0	1.642	-0.014	-0.16
0.5	53.7	0.613	0.73	-0.16	17.5	1.642	-0.017	-0.16
0.6	62.8	0.662	0.87	-0.16	21.1	1.642	-0.021	-0.16

406

The strong variation of the scattered electron energy with angle results in

times larger than for counter-propagating beams.

407 an extreme sensitivity to the uncertainty in the polar angle determination. It is
 408 shown in Table 3, to be a factor of 40 larger for a ^{50}Co beam colliding with 0.5
 409 GeV electrons than in a fixed-target kinematics with equivalent electron energy
 410 (1.64 GeV). This factor increases to about 400 for beams of ^{132}Sn . The sensi-
 411 tivity to the uncertainty in absolute value of the scattered electron momentum
 412 is about the same in both systems.

413 The colliding beam kinematics, however, allows identifying the residual nucle-
 414 us in coincidence with the scattered electron. Reaction products, including
 415 nucleons and γ -rays, can be detected using specific sub-detector systems. In
 416 addition, the detector setup allows to identify A and Z for the fragments, as
 417 shown in section 6. Their momenta and energies can be determined and the
 418 reaction kinematics can be reconstructed. This, in turn, allows a unique classi-
 419 fication of the observed reaction. In addition, the use of the coincidence method
 420 results in a strong reduction of the unavoidable radiative background seen in
 421 conventional inclusive electron-scattering experiments.

422 4. Conceptual design of the electron-nucleus collider at NESR

423 The conceptual layout of the collider facility is presented in Fig. 2. It consists
 424 of two rings with different circumferences: the electron ring EAR with electron
 425 energies between 0.2 and 0.5 GeV, and the ion ring NESR, which will operate
 426 at a set of discrete energies between 0.2 GeV/nucleon up to 0.74 GeV/nucleon.
 427 The electron ring is filled with electrons from a pulsed linac. NESR is supplied
 428 with pre-cooled fragment beams from a dedicated Collector Ring (CR) which is
 429 capable of cooling the secondary beams stochastically to primary beam quality
 430 within approximately 1.5 s.

431 The electron ring is placed outside the main ion ring, so that a bypass beam
 432 line connects NESR with EAR and provides sufficient space for the electron spec-
 433 trometer and a recoil detector system. The ion and electron beam trajectories
 434 intersect at an interaction point (IP) around which the electron spectrometer
 435 as well as auxiliary detectors for measuring the reaction products are placed.
 436 The IP is also viewed along the straight section through bore holes in the dipole
 437 magnets, that allow for installing the luminosity monitor described in section 7.

438 4.1. General considerations

439 The main parameters for the two rings and a hypothetical neutron-rich ura-
 440 nium isotope, with $A/Z = 2.7$ and kinetic energy 0.74 GeV/nucleon (this energy
 441 corresponds to a velocity $\beta_A = 0.8303$ and a rigidity of 12.5 Tm), are listed in
 442 Table 4. The ratio between the revolution frequencies of electrons and ions n
 443 should be an integer. Beam-beam effects require that n is as small as possible.
 444 An acceptable value for the highest ion energy 0.74 GeV/nucleon is $n = 5$. Then
 445 a discrete set of other possible energies is: 0.3587 GeV/nucleon ($n = 6$), 0.2254
 446 GeV/nucleon ($n = 7$). If the circumference of the NESR orbit is taken to be
 447 222.916 m, then 53.693 m are required for the circumference of the EAR. For
 448 the proposed beam-optics both beams are flat at IP, with horizontal beam sizes

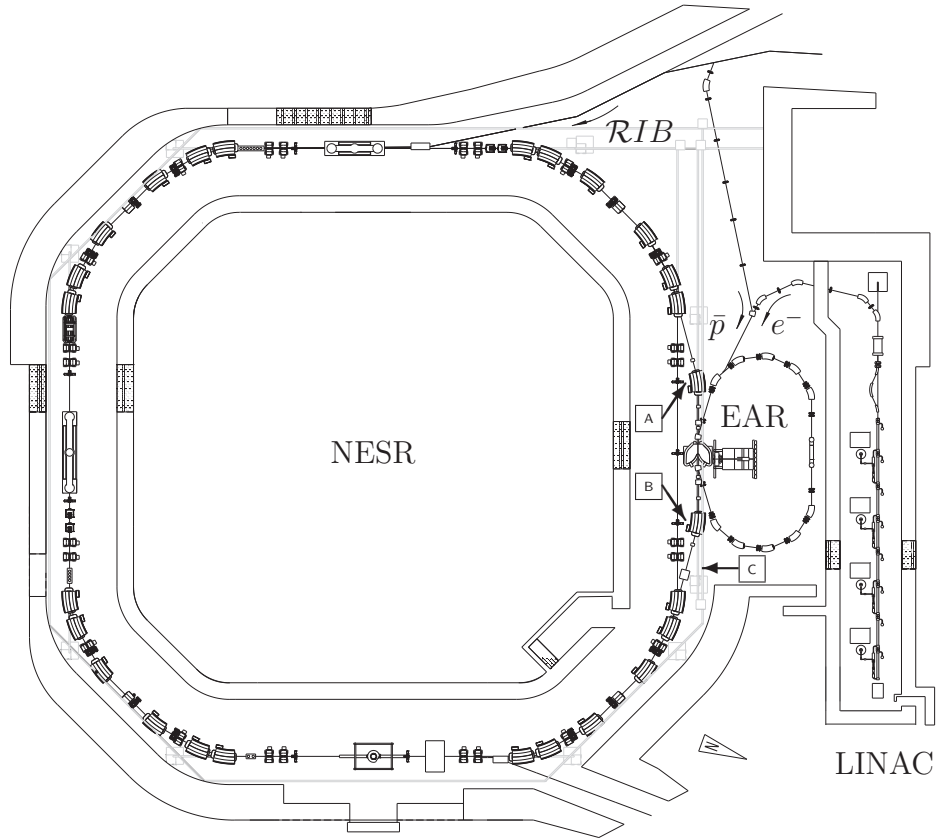


Figure 2: Schematic layout of the New Experimental Storage Ring (NESR, circumference 222.9 m) for Rare Isotope Beams (RIB) and the Electron Antiproton Ring (EAR, circumference 53.7 m). Electrons with energies ranging from 125 MeV to 500 MeV will be provided by an electron linac and stored in the EAR. Antiprotons can be directed from a dedicated collector ring (not shown) into the EAR via a separate beam line. The intersection between EAR and NESR is equipped with an electron spectrometer setup which will be discussed in the following. The free space opposing the spectrometer can be equipped with experiment specific detectors. The arrow at [C] points to the place where an optical bench is situated, from which the intersection can be viewed through a 10 cm hole in the dipole magnet. A luminosity monitor, based on bremsstrahlung detection, discussed in section 7, and LASER installations for atomic physics experiments can be installed here. For a detailed discussion of the bypass section ([A]-[B]) see text.

449 of $\sigma_x = 210 \mu\text{m}$ and $220 \mu\text{m}$ and vertical beam sizes of $\sigma_y = 85 \mu\text{m}$ and $87 \mu\text{m}$
 450 for the EAR and NESR, respectively.

451 The momentum spread of the electron beam at the interaction zone restricts
 452 the achievable resolution for the transferred energy and momentum in electron
 453 scattering experiments considerably. The momentum spread of the beam is
 454 shown in Fig. 3 as function of the electron energy. It depends mainly on two

Table 4: General parameters of the electron-nucleus collider assuming a 0.74 GeV/nucleon uranium beam.

	units	EAR	NESR
Circumference	m	53.693	222.916
Bending Radius, R	m	1.75	8.125
Maximum energy	GeV, GeV/nucleon	0.5	0.74
Revolution frequency, F_e, F_A	MHz	5.585	1.117
Number of bunches, n_e, n_A		8	40
Bunch population, N_e, N_A	particles	$5 \cdot 10^{10}$	$0.86 \cdot 10^7$
Bunch length, σ_s	cm	4	15
Beam size at IP, $\sigma_{x,y}$	μm	210; 85	220; 87
Momentum spread, $\frac{\Delta p}{p}$	%	$3.6 \cdot 10^{-2}$	$4 \cdot 10^{-2}$
Beam divergence at IP, $\sigma_{x0,y0}$	mrad	0.22; 0.58	0.22; 0.58
Beta function at IP, $\beta_{x,y}$	cm	100; 15	100; 15
Laslett tune shift, $\Delta\nu$			0.08
Luminosity	$\text{cm}^{-2}\text{s}^{-1}$	10^{28}	

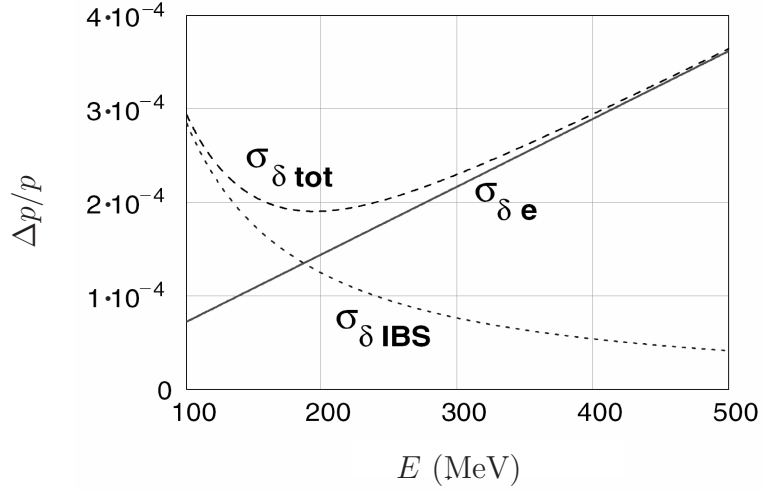


Figure 3: Dependence of the electron-beam momentum spread $\frac{\Delta p}{p}$ on the electron-beam energy E . Here $\sigma_{\delta e}$ denotes the contribution to the momentum spread from statistical fluctuations due to synchrotron radiation, $\sigma_{\delta IBS}$ is caused by intra-beam scattering, and $\sigma_{\delta tot}$ denotes the total momentum spread.

455 effects: (i) intra-beam scattering (IBS) and (ii) statistical fluctuations due to
456 synchrotron radiation. IBS is an effect where collisions between particles bring
457 charged particles closer to thermal equilibrium in a bunch and generally causes
458 the beam size and the beam-energy spread to grow. This effect limits as well

Table 5: Luminosities L for 0.74 GeV/nucleon ion beams for several reference nuclei. Here, $T_{1/2}$ is the half-life of the nucleus at rest, τ its total life time, and N the total number of ions stored in the NESR storage ring.

Element	$T_{1/2}$, s	τ , s	N	L , $\text{cm}^{-2}\text{s}^{-1}$
^{11}Be	13.8	35.6	$2.1 \cdot 10^{10}$	$2.4 \cdot 10^{29}$
^{35}Ar	1.75	4.5	$8.5 \cdot 10^7$	$1.7 \cdot 10^{27}$
^{55}Ni	0.21	0.5	$2.0 \cdot 10^7$	$4.0 \cdot 10^{27}$
^{71}Ni	2.56	6.5	$4.3 \cdot 10^7$	$1.1 \cdot 10^{27}$
^{93}Kr	1.29	3.3	$6.6 \cdot 10^6$	$1.8 \cdot 10^{28}$
^{132}Sn	39.7	68.2	$1.2 \cdot 10^9$	$1.9 \cdot 10^{28}$
^{133}Sn	1.4	3.5	$7.3 \cdot 10^6$	$2.0 \cdot 10^{26}$
^{224}Fr	199	59.2	$3.2 \cdot 10^8$	$8.6 \cdot 10^{27}$
^{238}U	10^{17}	60	$6.0 \cdot 10^{10}$	$1.0 \cdot 10^{28}$

459 luminosity and lifetime. IBS gives a relationship between the size of the beam
460 and the number of particles it contains, and leads therefore to a limit for the
461 maximally achievable luminosity [69]. The emission of quanta in synchrotron
462 radiation is a Poisson process. This process leads to a decrease of the mean
463 energy of electrons due to radiation losses [70] and to an increase of the energy
464 spread in a bunch caused by statistical fluctuations.

465 Assuming transverse Gaussian distributions for the bunches, the luminosity
466 (L) in a collider is given by

$$L = F_e n_e \frac{N_e N_A}{4\pi\sigma_x\sigma_y}. \quad (7)$$

467 Thus, options for a substantial increase of luminosity include the reduction of
468 beam sizes at the interaction zone $\sigma_{x,y}$ and/or an increase of bunch population
469 (N_e , N_A), number of colliding bunches n_e (or n_A) and revolution frequencies
470 F_e (or F_A). However, the decrease of $\sigma_{x,y}$ or an increase of N_e , N_A unavoid-
471 ably also increases the intra-beam scattering, and beam-beam forces which lead
472 to collective (coherent) and incoherent beam-beam instabilities and thus to a
473 reduction of the luminosity. In the case of a very intense ion beam, the space-
474 charge effect results in an upper limit of the luminosity $L_{\text{sp.ch.}}$, which does not
475 depend on the number of ions in the bunches, is given by

$$L_{\text{sp.ch.}} = F_e n_e \frac{A}{Z^2} \frac{N_e \Delta\nu \gamma^3 \beta^2}{4\pi r_p \sqrt{\beta_x \beta_y}} \frac{2\sqrt{2\pi}\sigma_s}{R}, \quad (8)$$

476 where r_p is the classical proton radius, β and γ are the Lorentz factors. For the
477 other variables, see definitions in Table 4.

478 Apart from the above-mentioned limitations leading to a flat plateau of
479 maximally achievable luminosities, as can be seen in Fig. 4, the production and
480 preparation of secondary beams strongly influence the total number of unsta-
481 ble isotopes available for experimental studies at the outer part of the nuclear

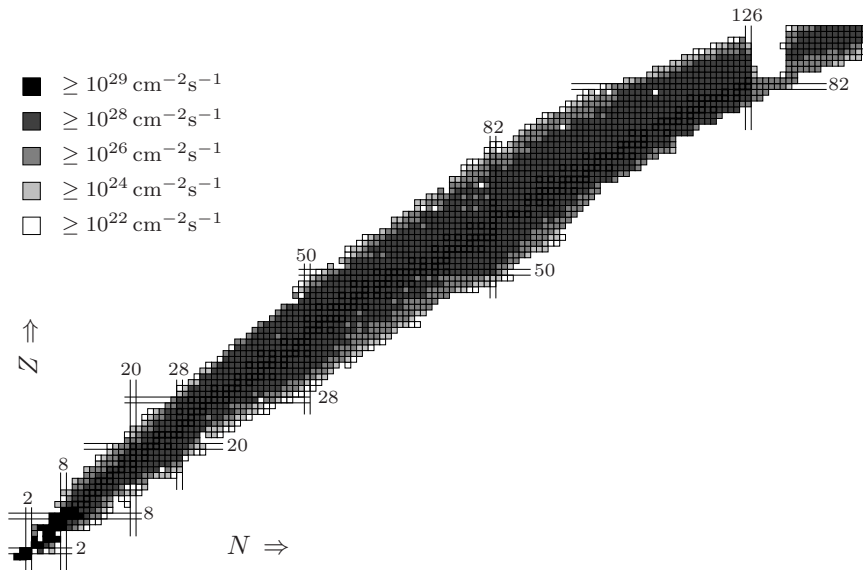


Figure 4: Maximum achievable luminosities for individual 0.74 GeV/nucleon ion beams at the interaction zone. Shown is the luminosity as function of the charge Z and the neutron number N according to the grey scale code shown in the upper left corner. Stable isotopes and magic numbers are labeled and distinguished by extended lines. A central plateau is visible, which drops rapidly at the edges where the most unstable and short-lived nuclei that can be studied with ELISE are situated. These luminosities comfortably suit to the requirements given in Table 1 on page 12 for a wide range of isotopes far from the valley of beta-stability. The simulation calculation takes fully into account, (i) production and separation process, (ii) transport through separator and beam lines, (iii) cooling and storage in the storage rings, and (iv) decay losses. For details, see text.

482 landscape. Table 5 shows a selection of the the numerical results as depicted
 483 also in Fig. 4.

484 (i) We start with an optimized production scheme, taking the maximum for
 485 the yield [71] and including the acceptance of the Super FRagment Separator
 486 (Super-FRS) [72] for fission and fragmentation reactions, whilst the available
 487 primary beams are varied. The mass-resolution [73] in the separator depends
 488 on the choice of the niobium degraders that are used in order to distinguish
 489 differently charged ions using the $B\rho-\Delta E-B\rho$ method in the Super-FRS via
 490 the expression:

$$(x|\delta_m) = -\frac{D_i}{M_i} \cdot \frac{d}{r_i} \cdot \frac{L_m}{\lambda}, \quad (9)$$

491 where $(x|\delta_m)$ is the variation of the position with ion mass, e.g. on a slit
 492 system, D_i denotes the dispersion, M_i the magnification and d/r_i the normalized
 493 degrader thickness for a given stage of the separator. The quantity L_m/λ relates
 494 to the stopping power of the degrader material. The degrader thickness is then

495 optimized with respect to the losses expected from electromagnetic dissociation
496 and nuclear reactions in the degrader material with an iterative procedure. The
497 total electromagnetic dissociation cross section is approximated using a model
498 where particular nuclei disintegrate via excitation to their giant dipole resonance
499 (GDR). The GDR resonance energy is taken from a parameterization [28] that
500 is based on experimental data. To calculate the cross section, we use 120% of
501 the Thomas-Reiche-Kuhn sum rule and the computed number of virtual E1-
502 photons. For that, the minimal impact parameter b_{min} , which is also used
503 to estimate the nuclear cross section, is obtained from the systematics [74] by
504 Benesh, Cook and Vary.

505 (ii) Subsequently, the transport and injection efficiency into the CR-ring
506 is taken into account by using a parameterization that is extracted from vari-
507 ous ion-optical simulation calculations [75] and depends on production process,
508 mass, and charge of the secondary beam particle.

509 (iii) Finally, nuclear and atomic life times are taken into account in order to
510 provide a reliable prediction of the number of cooled ions in the NESR storage
511 ring. Cooling and preparation of ions in the NESR is designed to take place in
512 at most two synchrotron (SIS100/300) cycle times, i.e. within 1.3 or 2.6 seconds.
513 The nuclear losses have been computed taking the information available from
514 the Lund/LBNL [76] database. The appropriate time dilation is taken into
515 account. For longer-lived ions (10 s to minutes) it is possible to further increase
516 intensity by stacking, i.e. injecting several cycles from the synchrotron into the
517 storage ring in case the production yield is limiting the number of stored ions.
518 Different stacking methods and associated parameters are still being studied
519 [77] and have not yet been included into the simulation calculation.

520 (iv) Atomic processes in the storage ring, when ions interact with electrons
521 of the electron cooler and the rest gas, are another important source of losses to
522 be taken into account. Electron capture from the electron cooler in particular
523 radiative recombination for fully stripped ions and the recombination processes
524 (Non Resonant electron Capture, NRC and Resonant Electron Capture, REC)
525 due to interaction with rest gas electrons can be calculated [78, 79, 80] with
526 good precision. Losses also occur when the charge state and, therefor, the
527 magnetic rigidity of the ions change so that they fall outside of the acceptance
528 of recirculating ions. The total life time τ in the ring is given by

$$\frac{1}{\tau} = \frac{1}{\tau_{\text{nuclear}}} + \frac{1}{\tau_{\text{atomic}}} \quad , \quad (10)$$

529 where τ_{nuclear} is the nuclear lifetime, see (iii), and τ_{atomic} is the atomic lifetime.
530 Numerical values for τ for selected isotopes can be found in Table 5 on page 17.

531 4.2. Physics performance: elastic scattering

532 As an example what can be achieved with ELISE, the results of two simula-
533 tions are shown in Fig. 5 for two the stable nuclei, ^{12}C and ^{208}Pb , which have
534 very large differences in their charge-density distributions.

535 The Fourier-Bessel parameters with which the "true" cross sections are cal-
536 culated are taken from [31]. These cross sections were obtained with the code

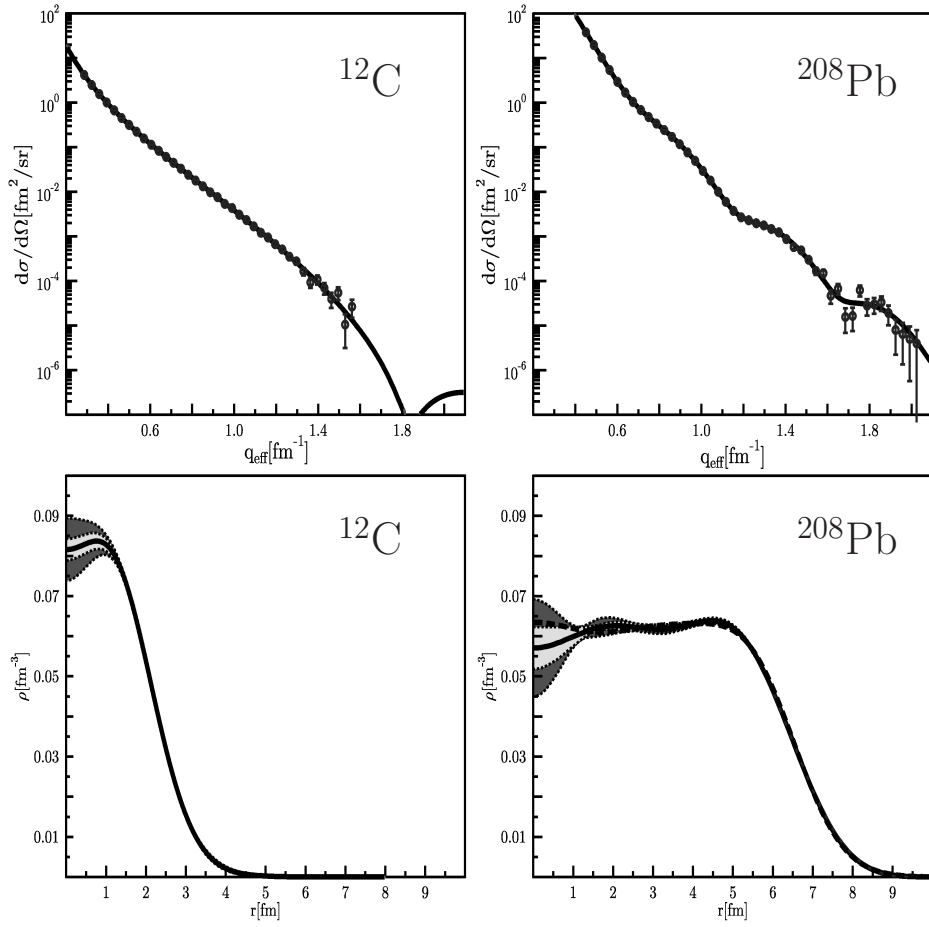


Figure 5: Results of the simulations for two hypothetical measurements to obtain the charge-density distributions of ^{12}C and ^{208}Pb with a luminosity of $10^{28} \text{ cm}^{-2}\text{s}^{-1}$, a solid angle of 100 msr and a running time of 4 weeks. The curves in the upper panels present the "true" cross sections obtained from the known parameters. The data are simulated data points generated around the curve with their statistical errors. In the lower panels, the corresponding charge-density distributions (solid curve) obtained from the simulated data are shown with the corresponding error bands. The dashed curve in the lower-right panel shows the initial charge distribution for reference. For the carbon case both curves are indistinguishable. See text for further details.

537 MEFICAL [81] that uses a distorted-wave approach. They were subsequently
 538 randomized with the expected statistics for a 4 week run, and with a luminosity
 539 of $10^{28} \text{ cm}^{-2}\text{s}^{-1}$ assuming a solid angle of 100 msr to obtain the "experimental"
 540 data points shown in the figure. These points were then fitted using the code
 541 MEFIT [81]. The output of this code is the parameters of the charge-density
 542 distribution. In the fit, an exponential fall-off as upper limit for the cross section

543 outside the measured region was assumed.

544 The inner-shaded areas in the lower panels of the figure result from the "sta-
545 tistical" uncertainties of the measurement and the outer-shaded areas represent
546 the fact that one does not measure to infinite momentum transfers and thus
547 creates an error in the Fourier transform. The results of the fit (solid curve)
548 can be compared directly with the original distributions used to generate the
549 "data" (dashed curve). As can be seen in the figure, with a modest solid angle
550 of 100 msr, a running time of 4 weeks, and a luminosity of $10^{28} \text{ cm}^{-2}\text{s}^{-1}$, one
551 can already have results for charge-density distributions which can be compared
552 to results of theoretical models.

553 The sensitivity of the simulated experiment indicated by the given error
554 band should be compared to the theoretical predictions presented by Grasso et
555 al. [14], where e.g. a central depletion by 50% in the nucleus ^{34}Si is expected
556 due to its particular nuclear structure. The shown result would clearly allow to
557 confirm or abandon such a forecast.

558 *4.3. Bypass design*

559 The bypass region is shown in detail in Fig. 6. The arrangement of magnetic
560 elements is symmetric with respect to the interaction point. The first two dipoles
561 are placed symmetrically around the IP at a distance of 1.9 m, leaving enough
562 space for installing the electron spectrometer. Both are used to separate the
563 orbits of ions and electrons. As electrons and ions have opposite electric charges
564 and move in opposite directions both orbits are deflected to the left by the
565 separation dipoles. The magnetic field in the dipoles has to be adapted to the
566 energy of the electron beam in order to bend the electrons to a fixed angle
567 (16.5°) before entering the EAR. The bending angle for ions depends on the
568 ion-beam energy and varies between 0.8° and 3.0° . Just in front of the bending
569 magnets two pick-up systems are installed in order to measure the beams orbits.
570 Two additional dipoles are placed exclusively in the ion path, allowing for an
571 orbit correction depending on the particular electron and ion beam energies.
572 The following quadrupole doublets combine the beta-functions in the IP and
573 in the ring and focus into the adjacent large dipole stages. These subsequently
574 bend the ions by 15° , and eventually, the ion trajectory unites with the original
575 ion orbit in the NESR.

576 The bypass is exclusively used in the collider mode. In this case, as shown
577 in Fig. 12 on page 30, the two last NESR magnets of NESRs dipole triplets in
578 the arcs are switched off in order to direct the ions into the bypass region. The
579 straight sections connecting the NESR with the EAR provide about 7 meters of
580 free space. The section before the interaction zone at position **B** in Fig. 6 will
581 be used to install an additional RF-cavity exclusively used for the preparation
582 of bunches for the collider mode. The section following position **A** is part of
583 the in-ring spectrometer setup described in section 6 on page 29.

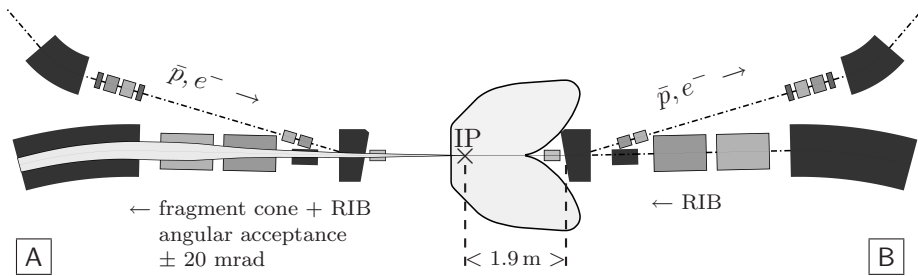


Figure 6: Interaction zone with the interaction point IP in the bypass section of the NESR. The labels **A** and **B** correspond to those in Fig. 2 on page 15. The bore holes along the beam axis for the viewports in the large dipole stages have been omitted in the drawing. Fragments emerging from the interaction zone are transported to a 7 m long straight section after the dipole (at position **A**) providing a sufficiently long time-of-flight path for the in-ring detectors system (see section 6).

584 5. Electron spectrometer

585 5.1. Challenges to be met

586 The technological challenge for the eA collider results from the simultaneous
 587 requirement for large acceptance and high momentum resolution. In addition,
 588 the spectrometer should allow for tracking the position of the reaction vertex
 589 inside the reaction zone. Existing magnetic spectrometers only partially fulfill
 590 these specifications. For instance, the electron spectrometers at the universities
 591 of Darmstadt [82] and Mainz [83] and at the research center TJNAF [84] meet
 592 the requirements with respect to momentum and angular resolution. They
 593 can handle reaction zones extending up to 10 cm, but only have a moderate
 594 acceptance of < 40 msr.

595 Existing toroidal and solenoidal spectrometers, e.g. HADES [85], BLAST [86]
 596 and BELLE [87], that cover 2π in azimuthal angle ϕ , provide the required ac-
 597 ceptance but only modest resolution. The main limitations for the resolution
 598 arise from energy and angular straggling of electrons in the tracking detectors.
 599 A large-acceptance spectrometer has advantages, but further research and devel-
 600 opment are needed for a suitable design, which can satisfy both experimental
 601 requirements as discussed above. Due to the fact that differential cross sections
 602 for electron scattering decrease rapidly with the angle of the scattered electron,
 603 an ideal electron spectrometer should cover 2π in azimuthal angle but needs
 604 to provide a moderate acceptance in scattering angle of about $\theta = 10^\circ - 20^\circ$
 605 only. The considerations have shown that magnetic dipole-based spectrometers
 606 designed for the collider with an acceptance up to about 100 msr can be built
 607 at a reasonable cost [88].

608 5.2. Large-angle dipole spectrometer

609 5.2.1. Spectrometer with large azimuthal acceptance

610 The restricted luminosity of the collider can be partially compensated by a
 611 large acceptance of the electron spectrometer. We consider first a spectrom-

612 eter with an extraordinarily large azimuthal acceptance, being compared to
 613 typical magnetic spectrometer installations. A spectrometer consisting of two
 614 quadrupoles and one dipole (QQD type) is a promising candidate for this pur-
 615 pose. The layout for such a spectrometer is shown in Fig. 7. The first quadrupole
 616 magnet with large aperture is located as close as possible to the IP.

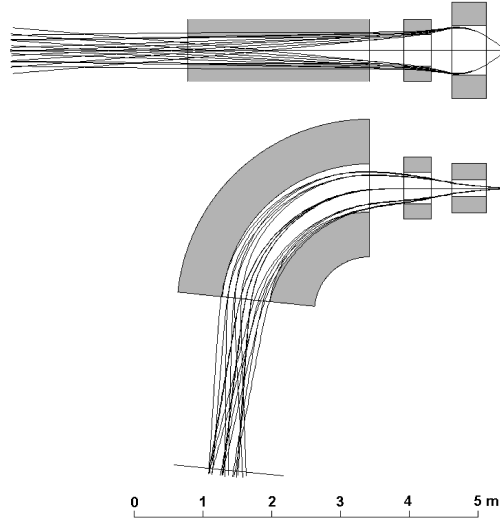


Figure 7: Side view (top) and top view (bottom) of the QQD-spectrometer with large azimuthal acceptance.

617 The rectangular aperture of the first quadrupole magnet is 72 cm in vertical
 618 and 24 cm in horizontal direction. The field gradient is 8.1 T/m. Because
 619 of the very high current density ($\approx 70 \text{ A/mm}^2$) reached, the coils have to be
 620 super-conducting. A very large acceptance in vertical angles $\approx \pm 34^\circ$ is achieved
 621 due to the strong vertical focusing force of the quadrupole. However, the first
 622 quadrupole magnet defocuses the horizontal motion. In order to compensate
 623 this effect, a second quadrupole magnet focusing horizontally and defocusing
 624 vertically is installed. This quadrupole magnet is a normal-conducting type
 625 with a field gradient of about 1.7 T/m. The dipole magnet placed downstream
 626 from the two quadrupole magnets analyzes the scattered electron momentum.
 627 For an arbitrarily chosen bending angle of the dipole magnet, the electron rays
 628 can be focused both horizontally and vertically at the focal plane by tuning the
 629 strengths of the quadrupole magnets.

630 The result of a ray-tracing calculation is shown in Fig. 7: 27 rays with 3
 631 magnetic rigidities (1.9, 2.0, and 2.1 Tm), for 3 horizontal angles ($+4^\circ$, 0° , and
 632 -4°) and 3 vertical angles ($+34^\circ$, 0° , and -34°) are shown. The acceptance
 633 exceeds 1200 mrad for the central momentum, but it is smaller at both edges
 634 of the momentum range. The horizontal angular acceptance is about 200 mrad.

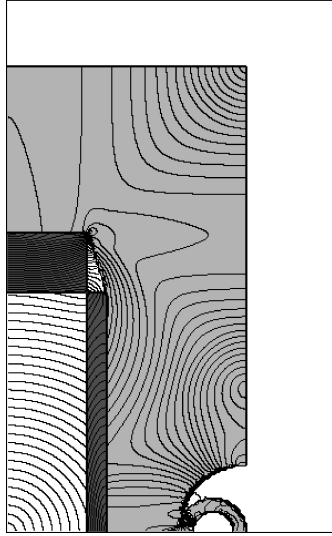


Figure 8: Three-dimensional magnetic field calculation for the first super-conducting Panofsky quadrupole of the QQD-spectrometer with large azimuthal acceptance. Contours of the field strength are shown in 0.1 Tesla steps. The quality of the quadrupole field is demonstrated by their equidistant and concentric appearance.

635 The spectrometer, as shown in Fig. 7, is optimized for measurements around a
 636 scattering angle of 90° , but can also be rotated around the IP to cover smaller
 637 angles. In order to allow measurements at smaller scattering angles, the first
 638 quadrupole magnet is made as slim as possible. For these requirements, a super-
 639 conducting Panofsky magnet, employing current sheets bound by iron, rather
 640 than shaped pole faces to establish the field, is the most suitable selection. A
 641 quarter of the first quadrupole magnet is shown in Fig. 8. The trimming of
 642 the side yoke is shown, which provides space for the beam pipe when QQD
 643 spectrometer is set at the minimal scattering angle of 50° . The most forward
 644 angle achievable with the QQD spectrometer depends on a compact magnetic
 645 shield. In the considered design, two cylindrical layers of magnetic shield cover
 646 the vacuum pipe of the colliding beams. The outer and inner radii of the shield
 647 are assumed to be 40 mm and 20 mm, respectively. The outer and inner shell
 648 thicknesses are then 13 mm and 5 mm, respectively. The shield suppresses
 649 the penetration of magnetic field through the side yoke of the magnet. A two-
 650 dimensional calculation shows that the detrimental magnetic field along the
 651 beam line is most serious at the front face of the quadrupole magnet where the
 652 conductor is not shielded by the yoke of the magnet in contrast to the side face.
 653 Without magnetic shield, the magnetic flux density at the nearest position to
 654 the pipe was calculated to be about 0.4 T. With the double-layered cylindrical
 655 shield, the field strength could be reduced to a safe value of about 0.003 T.

656 The performance of the spectrometer can be summarized as follows:

- 657 • The spectrometer provides an extraordinarily large vertical angle accep-
658 tance of 1200 mrad.
 - 659 • The acceptance in horizontal angle is about 200 mrad.
 - 660 • The spectrometer can be used for measurements in a range of scattering
661 angles from about 50° to more than 100° .
- 662 Selected properties of the magnetic elements are given in Table 6.

Table 6: Some properties of the elements for the QQD spectrometer with large azimuthal acceptance.

First quadrupole magnet			
horizontal aperture	24 cm	vertical aperture	72 cm
yoke width	72 cm	yoke height	140 cm
length	50 cm	field gradient	8.1 T/m
Second quadrupole magnet			
bore diameter	46 cm	field gradient	1.7 T/m
length	40 cm		
Dipole magnet			
gap	38 cm	bending angle	84°
mean orbit radius	180 cm	magnetic field	1.0 T

663 *5.2.2. Spectrometer with a large range of scattering angles.*

664 The second, more versatile system under consideration is an electron spec-
665 trometer composed of a deflection magnet (DM) where two vertical dipole mag-
666 nets (VM) can be placed symmetrically on both sides of the DM. The spectrom-
667 eter is schematically shown in Fig. 9 (only one VM is shown in this figure). The
668 DM magnet can be seen as a pair of dipoles with an opposite magnetic field
669 that are coupled together. The DM acceptance in vertical angle is ± 150 mrad.
670 The specific shape of DM ensures a deflection of the scattered electron in the
671 horizontal plane towards $\approx 90^\circ - \theta_{e'}$ i.e. perpendicular to the beam axis, for
672 scattering angles $\theta_{e'}$ ranging from about 10° to 60° . The inner regions can be
673 kept field free by appropriate shielding to avoid interference with the circulating
674 beams. Initially the pre-deflection system (DM) will be followed by the vertical
675 dipole spectrometer (VM) at the side of the DM facing inside the EAR. Elec-
676 trons that are elastically scattered to the same polar angle but with different
677 azimuthal angles are focused in the focal plane of the spectrometer. Calculated
678 trajectories for 500 MeV electrons elastically scattered off a 0.74 GeV/nucleon,
679 $A = 100$ ion, with transferred momenta of 400 and 600 MeV/c (43.91° and
680 62.82°), and assuming a 2 T field and a gap width of 25 cm for the VM, are
681 shown in Fig. 9. The VMs is equipped with two-dimensional coordinate detector
682 systems and a scintillator array. All detectors and foils are located outside the

683 vacuum chamber of the magnet system in order to minimize distortions from
 684 straggling.

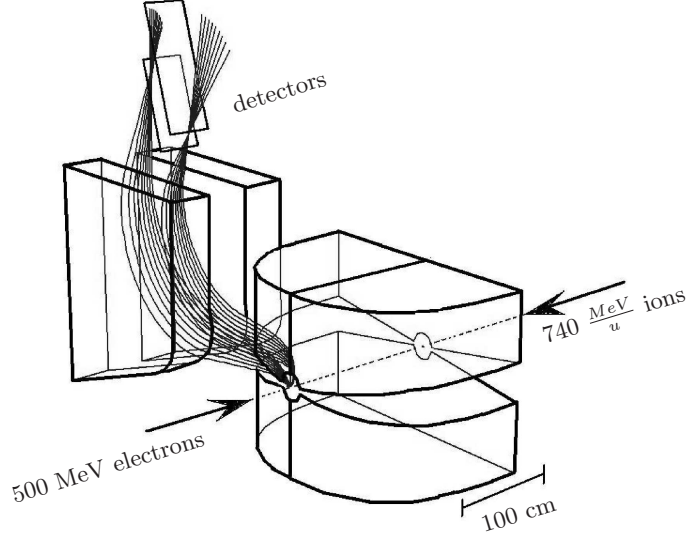


Figure 9: Schematic view of the electron spectrometer consisting of a pre-deflection magnet and a vertical-dipole spectrometer. Trajectories are shown for 500 MeV electrons elastically scattered off 0.74 GeV/nucleon, A=100 ions with a momentum transfer of 400 and 600 MeV/c (43.91° and 62.82°), respectively. The focal plane detectors are located outside the vacuum chamber of the magnet system.

685 Full three-dimensional Monte Carlo simulations have been performed to estimate the achievable resolution of the proposed spectrometer. The calculations
 686 were made in two steps. During the first stage, electron trajectories were generated according to the design parameters for momentum spread and beam size
 687 of the electron beam. Aiming at a pure characterization of the spectrometer no cross sections were taken into account in the simulations. The coordinates
 688 of electron-trajectory intersections with the detector planes were subsequently determined. The obtained hit coordinates were distributed randomly according
 689 to the response function of the detectors also including the angular and energy straggling of electrons in the materials. These results were stored as sequential
 690 vectors. The vectors were then used as input for the second stage where a back-tracking routine was applied in order to reconstruct the electron energy $T_{e'}$,
 691 the polar angle $\theta_{e'}$, the azimuthal angle $\varphi_{e'}$ and the position of the interaction point along the z-axis $z(IP)$. For this procedure, the x and y-coordinates of the
 692 interaction point were taken to be zero. Further simulations have shown that the result remains nearly the same if the small transverse extent of the electron
 693 beam (see Table 4) is also taken into account. The result of these studies is that all parameters $T_{e'}$, $\theta_{e'}$, $\varphi_{e'}$ and $z(IP)$ can be reconstructed with satisfying
 694 accuracy from the four parameters of the hits in the two planes of focal-plane detectors. These results are shown in Figs. 10 and 11 for the case of a large
 695 momentum transfer (between 400 MeV/c and 600 MeV/c) where the kinematics
 696
 697
 698
 699
 700
 701
 702
 703
 704
 705

706 for colliding beams is most unfavorable for the reconstruction.

707 Disentangling elastic and inelastic scattering in colliding beam kinematics is
 708 challenging. The angular range of electrons passing through the VM is about
 709 20° for energies between 560 and 660 MeV. The difficulty is to resolve the peaks
 710 separated by only a few hundred keV. This is illustrated in Fig. 10 (left panel)
 711 where the thickness of the displayed line is determined by the energy difference
 712 of electrons scattered elastically or inelastically with $E^* = 1.5, 3.0$ MeV.

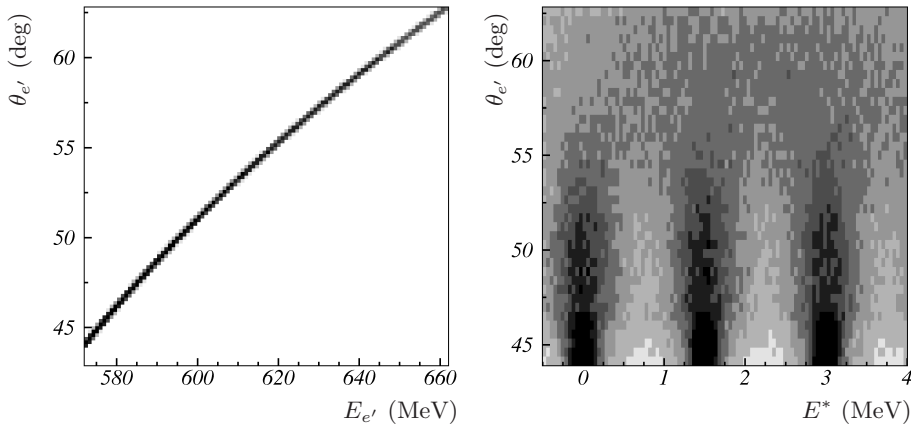


Figure 10: Left panel: Angle versus energy-range covered for a particular setting of the vertical dipole. The curve is obtained in Monte Carlo simulations where 500 MeV electrons scatter off 0.74 GeV/nucleon ions with $A = 100$. Elastic and inelastic ($E^* = 1.5, 3.0$ MeV) scattering events contribute to the observed seemingly unresolved line. The presented range in scattering angles poses the worst case scenario for reconstructing the excitation energy. Right panel: Polar angle dependence of the recovered excitation energy. A back-tracking routine was used for the reconstruction. Distortions due to momentum spread in the beam, finite beam size, straggling effects and position resolutions of the detectors are present.

713 In order to account for the extent of the interaction zone $\sigma_z \approx 5$ cm, the first
 714 two-dimensional coordinate detector is put in the plane where the trajectories
 715 with different azimuthal angles constitute a focus for a given polar angle. The
 716 second detector is placed in parallel to the first detector at a distance of 50 cm.
 717 The spatial resolution of the first detector is assumed to have a Gaussian dis-
 718 tribution with a standard deviation of $50 \mu\text{m}$. This detector and the separation
 719 foil result in an angular straggling of 1 mrad. The resolution of the detector
 720 at the second plane is taken to be $100 \mu\text{m}$. The calculations demonstrate the
 721 possibility to satisfy all experimental requirements with this spectrometer setup
 722 (see also Fig. 11).

723 5.3. Coordinate detectors

724 The use of coordinate detectors based on straw tubes [89] has several ad-
 725 vantages. Cross talk is minimized, since the cells are isolated from each other.
 726 A channel with a broken sense wire can easily be switched off without turning

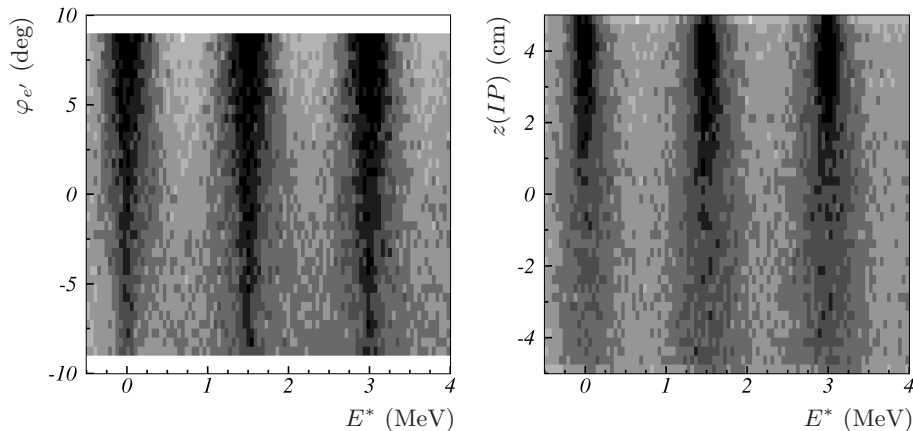


Figure 11: Left panel: Dependence of the reconstructed excitation energy on azimuthal angle. Right panel: Dependence of the reconstructed excitation energy on the position of the interaction point. Parameters of Monte Carlo calculations are the same as in Fig. 10. The picture shows a clear dependence of the achievable E^* resolution on $z(IP)$ position and $\varphi_{e'}$ angle.

727 off all channels. Straw tubes can be designed to withstand pressure and can be
 728 placed in vacuum. The inner pressure not only keeps tubes round and inflexible
 729 but also results in better resolution. The resolution of tracks is almost indepen-
 730 dent of the incident angle and angular corrections are not necessary when the
 731 drift distance is calculated from the drift time, as with usual drift chambers.

732 A prototype straw-tube assembly has been built and put into operation at
 733 the GSI detector laboratory. The prototype design is based on Kapton tubes
 734 covered with a $0.2 \mu\text{m}$ aluminum layer. The tubes are 60 cm in length and
 735 feature a 7.5 mm inner diameter and a total tube-wall thickness of $126 \mu\text{m}$. The
 736 tubes are filled with Ar/CO₂ (80%/20%) at atmospheric pressure and operate
 737 at 1850 V. Detailed studies are currently in progress. Straw tubes filled with
 738 quench gases can be operated at even higher pressure ($\approx 4 \text{ atm}$) and a higher
 739 voltage ($\approx 4 \text{ kV}$); see Ref. [90]. Saturated streams in this mode are initiated
 740 with high efficiency by a single electron with a gain factor of about $5 \cdot 10^5$. The
 741 achieved average spatial resolution of a single tube is $50 \mu\text{m}$ [90].

742 The second position-sensitive detector system under consideration is the use
 743 of vertical drift chambers instead of two layers of x, y -coordinate detectors.
 744 These chambers allow to measure two coordinates of the electron trajectory
 745 crossing the detector plane (x, y) as well as polar and azimuthal angles (θ, ϕ)
 746 of the electron trajectory. Existing chambers provide a resolution close to the
 747 requirements: $\delta x < 100 \mu\text{m}$, $\delta y < 200 \mu\text{m}$, $\delta\theta < 0.3 \text{ mrad}$, $\delta\phi < 1 \text{ mrad}$. Such
 748 a system is routinely used at the MAMI facility [91] and at TU Darmstadt.
 749 Therefore, the already existing designs could be easily adapted to meet the
 750 requirements of the ELISE experiment.

751 It is foreseen to place a plastic scintillation system after the focal plane

752 of the spectrometer. This system consists of 2 modules (plastic scintillation
753 bars, $120 \times 10 \times 4 \text{ cm}^3$) viewed by two photomultiplier tubes from opposite
754 sides coupled with optical pads to the attached light guides. The expected
755 intrinsic time resolution will thus be about 0.1 - 0.2 ns. The bunch timing
756 signals of the NESR will be used for time-of-flight measurements. It is already
757 sufficient to use only one module to detect scattered electrons. The second
758 module is introduced in order to decrease background. The scintillation bars can
759 be manufactured from NE-102 material. Such systems have been successfully
760 used in different experiments to measure electrons with high efficiency and good
761 timing resolution [92].

762 6. In-ring detectors

763 The detection of reaction products is another task required of the ELISE
764 facility. A detector setup placed behind the straight bypass section ($\boxed{\text{A}}-\boxed{\text{B}}$, see
765 Fig. 2) using the first bending dipole as spectrometer magnet for heavy ions is
766 foreseen to be used for this task. The detectors will operate in coincidence with
767 the scattered electrons. They will allow to disentangle different reaction chan-
768 nels in the case of inelastic scattering experiments (e.g. excitation of particle
769 unstable states, quasi-free scattering, electro-fission) and provide means to clean
770 the electron energy spectra from radiative tails originating from other reaction
771 channels.

772 Cooled heavy-ion beams circulate in the NESR with a momentum spread of
773 $\Delta p/p \approx 10^{-4}$ and with an emittance of about $1\pi \text{ mm mrad}$. The design and
774 settings of the magnetic devices are thus governed by the requirement to keep
775 a high-quality ion beam stored. Therefore, the degrees of freedom in building
776 a large acceptance system for the ions emerging from the interaction zone are
777 rather limited. The current design for the bypass shown in Fig. 6 on page 22
778 allows for the detection of fragments in a $\pm 20 \text{ mrad}$ cone which is sufficient
779 for performing the most demanding electro-fission experiments, thanks to the
780 kinematical forward focusing.

781 A possible version of the in-ring detector layout is shown in Fig. 12 together
782 with trajectories calculated for fragments with different magnetic rigidities in
783 steps of 1%.

- 784 • The detector array at position 1 in Fig. 12 allows for the reaction tagging
785 by particle identification for ions (e.g. $(e, e'n)$ via $(e, e'^{A-1}Z)$).
- 786 • The two arrays at positions 2 and 3 provide in addition a fragment track-
787 ing with moderate momentum resolution (by time-of-flight measurements,
788 and with an acceptance $\Delta B\rho/B\rho \approx \pm 7\%$). The obtained resolution is
789 high enough to identify also fission fragments with their large momentum
790 spread.
- 791 • The detector array at position 4 implements the same tasks with even
792 better resolution but further reduced acceptance.

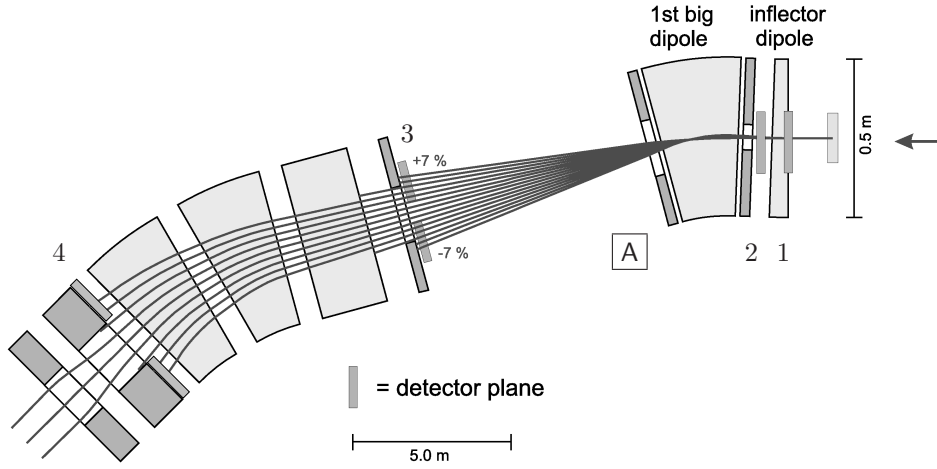


Figure 12: Ion trajectories calculated for different magnetic rigidities through the first bending and adjacent straight section behind the interaction zone. These trajectories are shown for 7 steps of 1% deviation in magnetic rigidity in positive and negative direction from the nominal magnetic rigidity of the circulating beam, respectively. Label **A** refers to the position shown in the previous setup figures 2 and 6.

793 Simulation calculations show, that a resolution of $\Delta p \approx 20 \text{ MeV}/c$, cor-
 794 responding to about 0.5 MeV missing energy resolution, can be achieved for
 795 both longitudinal and transverse momenta in the case of quasi-free scattering
 796 (e,e'p) for a 500 MeV electron beam interacting with 740 MeV/nucleon oxygen
 797 isotopes. In addition, a time-of-flight resolution of 35ps FWHM is needed to
 798 separate fission fragments by mass reliably. First measurements have shown,
 799 that this time resolution can be reached by using quenched scintillator material
 800 viewed with fast photomultipliers.

801 Detectors located near the circulating beam in the first two planes (1 and 2 in
 802 Fig. 12) should be UHV compatible and should be thin enough in order to avoid
 803 distortions caused by multiple scattering inside the detector material. The first
 804 choice is an array of 100 μm thick CVD (chemical vapor deposition) diamond
 805 micro-strip detectors. Alternatively, 100 μm thick silicon detectors would also
 806 meet the requirements, however, they are more sensitive to irradiation. Both
 807 detector types can provide 0.1 mm resolution for the ion hit positions. Compared
 808 to Si-based detectors, a diamond detector has excellent merits in terms of high
 809 radiation resistance, low leakage current, high operation temperature and high
 810 chemical inertia. The expected resolutions for these assemblies are $\Delta p/p \approx$
 811 10^{-3} and 1 mrad for the momentum and angle measurements, respectively, in
 812 accordance with the previously shown example.

813 Since the detectors can only be positioned after the beam preparation dur-
 814 ing setup or cooling phase in the NESR is completed, the detector arrays are
 815 subdivided into two parts, each one mounted on a remotely controlled driving
 816 device. They are designed to be removable in vertical direction and the range

817 is kept adjustable according to the beam emittance. Scattered ions can then be
818 detected starting from a minimum scattering angle of about 1 mrad.

819 A halo around the ion beam stored in the NESR could potentially damage
820 the detectors. Another source of radiation are beam ions leaving the orbit after
821 scattering off the counter-propagating electrons or ions that undergo atomic
822 charge-changing reactions in the rest gas. Calculations have shown that for a
823 luminosity of $10^{29} \text{ cm}^{-2}\text{s}^{-1}$ the count rate, normalized to the detector area, will
824 not exceed $10^4 \text{ cm}^{-2}\text{s}^{-1}$ for detectors placed at a distance of 10 mm from the
825 NESR beam axis. This estimate means that neither the diamond nor the silicon
826 detectors will show any essential damage even after three years of continuous
827 operation.

828 The existing experimental storage ring (ESR) at GSI is equipped with gas de-
829 tectors, scintillators, silicon-strip detector arrays, and diamond detectors. The
830 experience obtained during operation of ESR will be used and existing tech-
831 niques will be extended to satisfy the specific demands of the eA collider.

832 7. Luminosity monitor

833 Elastic electron scattering is always accompanied by the process of brems-
834 strahlung, involving emission of photons. A radiative tail of lower-energy elec-
835 trons appears in the electron energy spectrum, e.g. due to bremsstrahlung, lead-
836 ing to an extension of the electron energy spectrum below the elastic scattering
837 peak [93]. Bremsstrahlung is therefore commonly used to monitor luminos-
838 ity. The angular and energy distributions of the bremsstrahlung are shown in
839 Fig. 13. The narrow angular distribution ($\Delta\theta_\gamma \approx 1/\gamma_e$ rad) allows for diagnostic
840 and adjustment of the electron beam position.

841 The presence of rest gas in NESR, even on a level of $3 \cdot 10^{-11}$ mbar, is a source
842 of $500 N_\gamma/\text{s}$ background bremsstrahlung of photons with energies larger than
843 100 MeV for the electron-beam parameters given in Table 4. As can be seen
844 in Fig. 13 in panel 2, the effect of screening by orbital electrons leads to strong
845 changes in the bremsstrahlung spectrum. This effect allows in principle for a
846 correction for the rest-gas background contribution by precise measurements of
847 the shape of the γ -spectra. Bremsstrahlung intensities of γ -rays with energies
848 larger than 100 MeV are given in Table 7 for several reference nuclei with a
849 kinetic energy of 0.74 GeV/nucleon. In this table, L_B denotes the luminosity
850 where the γ -ray background due to the rest-gas becomes equal to the amount
851 of bremsstrahlung caused by the presence of the ion beam. We neglect the
852 ionization of the residual gas in the vacuum chamber by the circulating electron
853 bunches. The ionization creates positive ions which under certain circumstances
854 become trapped in the potential well of the stored electron beam [94]. The effect
855 is suppressed due to the counter-propagating beam of positive ions moving along
856 the same trajectory.

857 For the luminosity measurement using bremsstrahlung a system capable of
858 detecting high energy photons is needed. The PbWO_4 crystal is distinguished by
859 its fast decay time (6/30 ns at 440/530 nm), a high density (8.28 g/cm^3) and its
860 radiation hardness. Thus, it is an excellent γ -detector also due to its favorable

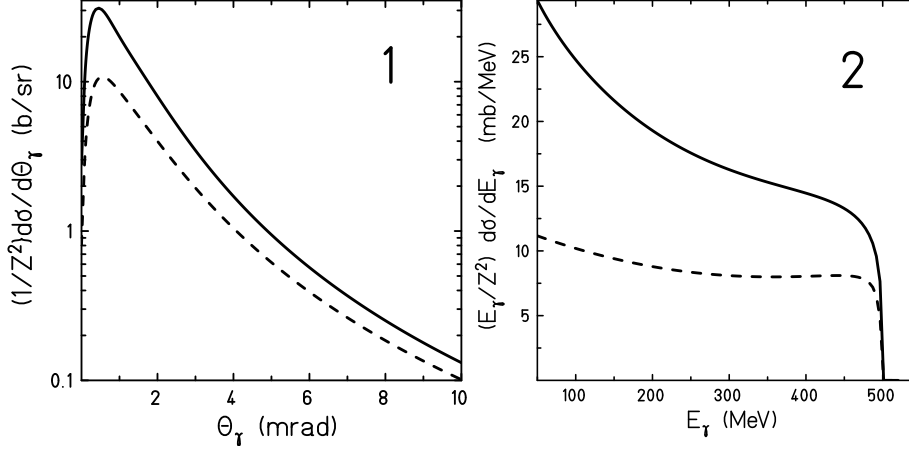


Figure 13: Angular (panel 1) and energy (panel 2) distributions of bremsstrahlung emitted by the electron beam. The distributions are given for scattering off 0.74 GeV/nucleon ions (solid curve) and on rest-gas nuclei (dashed curve). In the latter case, the effect of the screening of the nucleus by atomic electrons is taken into account.

Table 7: Bremsstrahlung intensity for γ -rays with energies higher than 100 MeV (ion beam kinetic energy 0.74 GeV/nucleon). Here, σ_B is the cross section for producing bremsstrahlung at the given conditions, and L_B is the value where the γ -background caused by rest-gas in the storage ring becomes equal to the amount of bremsstrahlung induced by the ion beam.

Ion beam	Luminosity $\text{cm}^{-2} \text{s}^{-1}$	σ_B barn	Yield N_γ 10^3s^{-1}	L_B $\text{cm}^{-2} \text{s}^{-1}$
^{11}Be	$2.4 \cdot 10^{29}$	0.48	115.2	$1.1 \cdot 10^{27}$
^{35}Ar	$1.7 \cdot 10^{27}$	9.7	16.5	$5.3 \cdot 10^{25}$
^{55}Ni	$4.0 \cdot 10^{27}$	23	94.1	$2.2 \cdot 10^{25}$
^{71}Ni	$1.1 \cdot 10^{27}$	23	25.9	$2.2 \cdot 10^{25}$
^{93}Kr	$1.8 \cdot 10^{28}$	38	700	$1.3 \cdot 10^{25}$
^{132}Sn	$1.9 \cdot 10^{28}$	75	1425	$7.0 \cdot 10^{24}$
^{133}Sn	$2.0 \cdot 10^{26}$	75	15.0	$7.0 \cdot 10^{24}$
^{224}Fr	$8.6 \cdot 10^{27}$	227	1953	$2.3 \cdot 10^{24}$
^{238}U	$1.0 \cdot 10^{28}$	254	2539	$2.0 \cdot 10^{24}$

861 optical, physical and chemical properties, accounting for its long- term stability.
862 The radiation length (x_0) of the crystal is less than 1 cm, where x_0 is linked
863 to the total energy loss $E(x)$ by $E(x) = E_0 \exp(-x/x_0)$. A material thickness
864 corresponding to $20x_0$ is sufficient to absorb about 99% of the induced showers.
865 The crystals are characterized by a very small Molière radius (≈ 2 cm) which
866 describes the transverse extension of the showers due to multiple scattering

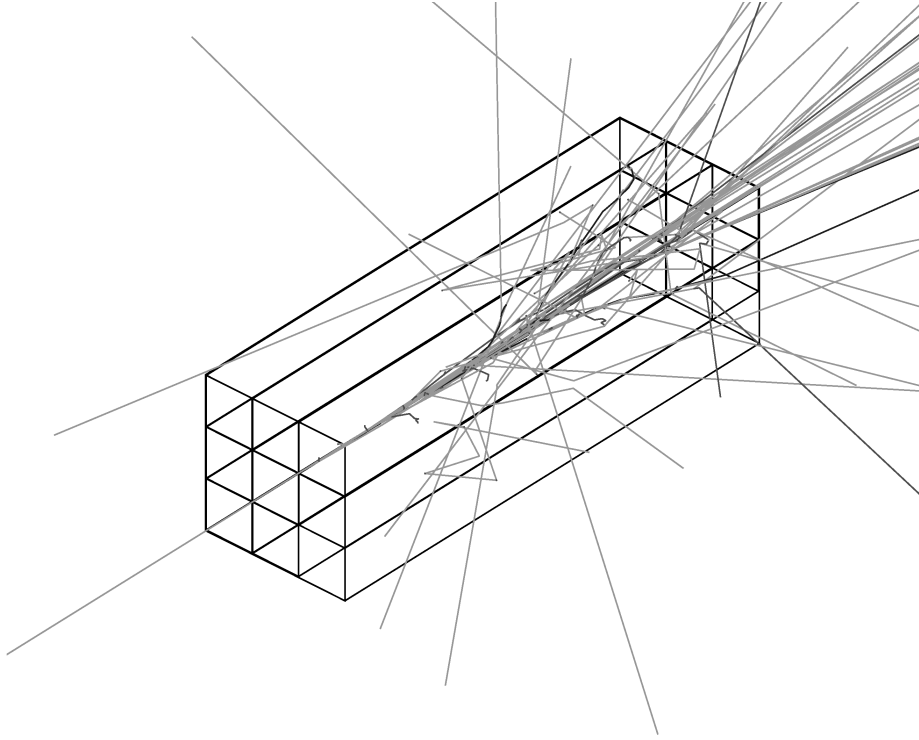


Figure 14: Shower created in a stack of 3×3 PbWO_4 crystals by one 300-MeV-gamma ray (GEANT4 simulation calculation). The geometry used for the calculations is the same as described in the text.

867 of low energy electrons inside the material. More than 99% of the shower is
 868 situated within 3 Moliere radii bounds. The application of these detectors for
 869 γ -spectroscopy from tens of MeV up to several hundred MeV with good energy
 870 ($\sigma_E/E = (1.7/\sqrt{E[\text{GeV}]} + 0.6)\%$) and spatial resolution ($\sigma_{x,y} \leq 5$ mm) is
 871 feasible [95].

872 The luminosity monitor will be built as a 3×3 matrix of PbWO_4 scintillators
 873 ($20 \times 20 \times 200$ mm³), and placed about 8–10 m from the interaction point (see
 874 Fig. 2 on page 15, [C]). The bremsstrahlung beam then illuminates mainly
 875 the central cell of the matrix. The detector array covers the dominant part of
 876 the radiation cone. A simulated shower created by one 300-MeV-gamma ray
 877 is shown in Fig. 14. An Avalanche Photo Diode (APD) readout is currently
 878 foreseen which achieves a suitable energy resolution, if the diode is being cooled
 879 down to a well stabilized ($\Delta T = 0.1^\circ\text{C}$) temperature.

880 **8. Data acquisition and handling**

881 There are several specific demands on the ELISe data acquisition and online
882 analysis, as the experiment is an integral part of the NESR/EAR accelerator
883 complex. The detection system in the ELISe experiment will be used to monitor
884 the achieved beam quality, and to optimize the beam settings accordingly. A
885 strong coupling to the accelerator control system requires stable operation of
886 the detector systems with their associated slow-control components and online
887 analysis. Furthermore, it is mandatory that these systems can be operated
888 without detailed knowledge about their components by the accelerator staff.
889 Since ELISe will act as a data source for the accelerator controls, we foresee
890 strict compliance to the given interfaces and timing definitions and will provide
891 pre-analysis, e.g., profile, luminosity and emittance information.

892 At the same time, the experimental data treatment will require complete
893 event-wise data recording at the highest possible rates in the electron tracking
894 system. The tracker will be read out by dedicated front-end electronics (e.g.
895 [96]) coupled to a flexible (FPGA, DSP, CPU based) readout system that will
896 perform the first analysis steps on-line. In such a way, a considerable data reduction
897 coming from this fixed installation within the experiment can be achieved.
898 We plan to run a trigger-less, data-driven system. The front-end acquisition
899 system will also allow for further data and background reduction by using local
900 trigger information in order to define regions of interest in the data stream.
901 The concept for the actual data readout, event building, transfer and long-term
902 storage is based on a scalable and standardized system (e.g. [97]) provided by
903 GSI/FAIR, see also [98].

904 **9. Summary**

905 The proposed electron-ion collider will provide a unique experimental facility
906 for FAIR. The ELISe experiment is part of the core program [99] of the FAIR
907 facility.

908 It becomes feasible due to the intense pulsed beams from the FAIR syn-
909 chrotrons, allowing for an optimized storage-ring operation. Luminosity esti-
910 mates have been presented in this paper and the collider kinematics has been
911 discussed. It turns out that the large center-of-mass energy for the electrons
912 leads to small center-of-mass angles for a particularly chosen momentum trans-
913 fer. The expected cross sections are thus sizable and will largely compensate
914 the seemingly poor luminosities achievable for collider experiments.

915 A major advantage of the ELISe facility, in addition to the analysis of elec-
916 trons, is the possibility also to fully analyze recoils and target fragments after
917 reactions. They are moving with the stored ion beam towards the first bending
918 section in the ion path following the intersection of the two storage rings. The
919 section is subsequently also used as magnetic spectrometer for the recoils.

920 The most attractive as well as challenging features of the proposed concept
921 are:

- 922 • The ELISe project pioneers electron scattering off radioactive nuclei for
923 nuclear structure studies while making use of well established heavy-ion
924 storage-ring techniques.
- 925 • The versatile ELISe experiment, will consist of three major components
926 (i) an electron spectrometer, (ii) an in-ring detection system, and (iii) a
927 luminosity monitor, which can be extended with additional detectors for
928 specific experiments.
- 929 • These basic components have been considered in this paper. They can
930 handle a wide range of different nuclear reactions and thus address numer-
931 ous physics questions. Kinematically complete measurements where the
932 electrons, the target-like recoils with their associated gammas, are mea-
933 sured with high efficiency are facilitated due to the relativistic focussing
934 (Lorentz boost). This is quite in contrast to conventional fixed-target
935 electron-scattering experiments.
- 936 • Technologically, the requirement of high resolution combined with high ac-
937 ceptance for the electron spectrometer is most demanding. Two concepts
938 for the spectrometer have been shown here, and their properties have been
939 discussed.

940 The conceptual design of a collider experiment for nuclear structure investi-
941 gations is featured in the present paper. The envisaged solutions fulfil already
942 most of the experimental requirements posed by the physics cases. In the fu-
943 ture, a more detailed design of particular components will be presented. The
944 expected gain of information will allow to perform realistic physics simulations,
945 where ELISe's physics performance can be fully explored.

946 Acknowledgements

947 The authors acknowledge financial support from the EC via the INTAS pro-
948 gramme, grants No. 03-54-6545 and 05-1000008-8272. This work was partially
949 supported by the Hessian LOEWE initiative Helmholtz International Center for
950 FAIR.

951 References

- 952 [1] NuPECC Long Range Plan 2004,
953 http://www.nupecc.org/lrp02/long_range_plan.2004.pdf;
954 http://www.nupecc.org/pub/NuPECC_Roadmap.pdf.
- 955 [2] E. Garrido, E. Moya de Guerra, Nucl. Phys. **A650** (1999) 387.
- 956 [3] E. Garrido, E. Moya de Guerra, Phys. Lett. **B488** (2000) 68.
- 957 [4] S.N. Ershov, Yad. Fiz. **67** (2004) 1877; Phys. Atomic Nuclei **67** (2004)
958 1851.

- 959 [5] Z. Wang, Z. Ren, Phys. Rev. **C 70** (2004) 034303.
- 960 [6] S.N. Ershov, B.V. Danilin, J.S. Vaagen, Phys. Rev. **C 72** (2005) 044606.
- 961 [7] A.N. Antonov, D.N. Kadrev, M.K. Gaidarov, E. Moya de Guerra, P. Sar-
962 riguren, J.M. Udias, V.K. Lukyanov, E.V. Zemlyanaya, G.Z. Krumova,
963 Phys. Rev. **C 72** (2005) 044307.
- 964 [8] C.A. Bertulani, J. Phys. (London) **G34** (2007) 315.
- 965 [9] C.A. Bertulani, Phys. Rev. **C 75** (2007) 024606.
- 966 [10] C.A. Bertulani, Phys. Rev. **C 75** (2007) 057602.
- 967 [11] S. Karataglidis, K. Amos, Phys. Lett. **B650** (2007) 148.
- 968 [12] E. Khan, M. Grasso, J. Margueron, N. Van Giai, Nucl. Phys. **A800** (2008)
969 37;
- 970 [13] X. Roca-Maza, M. Centelles, F. Salvat, X. Viñas, Phys. Rev. **C 78** (2008)
971 044332.
- 972 [14] M. Grasso, L. Gaudefroy, E. Khan, T. Niksic, J. Piekarewicz, O. Sorlin,
973 N. Van Giai, D. Vretenar, Phys. Rev. **C 79** (2009) 034318.
- 974 [15] Yu.Ts. Oganessian, O.N. Malyshev, I.N. Meshkov, V.V. Parkhomchuk,
975 P. Pokorný, A.A. Sery, S.V. Stepantsov, Ye.A. Syresin, G.M. Ter-Akopian,
976 V.A. Timakov, Z. Phys. **A341** (1992) 217.
- 977 [16] T. Katayama, T. Suda, and I. Tanihata, Phys. Scr. **T 104** (2003) 129.
- 978 [17] G. Münzenberg, J. Friese, H. Geissel, I. Meshkov, G. Schrieder, E. Syresin,
979 Nucl. Phys. **A626** (1997) 249.
- 980 [18] I. Meshkov, G. Münzenberg, G. Schrieder, E. Syresin, G.M. Ter Akopian,
981 Nucl. Inst. Meth. **A391** (1997) 224.
- 982 [19] L.V. Chulkov, G. Münzenberg, G. Schrieder, H. Simon, Phys. Scr. **T104**
983 (2003) 144.
- 984 [20] H. Simon, Nucl. Phys. **A787** (2007) 102.
- 985 [21] FAIR - Facility for Antiproton and Ion Research,
986 http://www.gsi.de/fair/index_e.html.
- 987 [22] T. Suda, M. Wakasugi, Prog. Part. Nucl. Phys. **55** (2005) 417.
- 988 [23] A. Richter, Nucl. Phys. **A751** (2005) 3c.
- 989 [24] B. Jonson, Phys. Rep. **389** (2004) 1.
- 990 [25] T.W. Donnelly, J.D. Walecka, Ann. Rev. Nucl. Part. Sci. **25** (1975) 329.

- 991 [26] E. Moya de Guerra, Phys. Rep. **138** (1986) 293.
- 992 [27] J. Heisenberg, H.P. Blok, Ann. Rev. Nucl. Part. Sci. **33** (1983) 569.
- 993 [28] M. N. Harakeh and A. van der Woude, Giant Resonances, (Clarendon Press,
994 Oxford, 2001).
- 995 [29] D. Drechsel, M.M. Giannini, Rep. Prog. Phys. **52** (1989) 1083.
- 996 [30] D.R. Yennie, D.G. Ravenhall, and R.N. Wilson, Phys. Rev. **95** (1954) 500
997 (and references therein).
- 998 [31] H. de Vries, C.W. de Jager, C. de Vries, At. Data Nucl. Data Tables **36**
999 (1987) 495.
- 1000 [32] G. Fricke, C. Bernhardt, K. Heilig, L.A. Schaller, L. Schellenberg,
1001 E.B. Shera, C.W. de Jager, At. Data Nucl. Data Tables **60** (1995) 177.
- 1002 [33] J. Friedrich, N. Voegler, Nucl. Phys. **A373** (1982) 192.
- 1003 [34] I. Angeli, R.J. Lombard, Z. Phys. **A 324** (1986) 299.
- 1004 [35] J. Friedrich, N. Voegler, P.-G. Reinhard, Nucl. Phys. **A459** (1986) 10.
- 1005 [36] G.S. Anagnostatos, A.N. Antonov, P. Ginis, J. Giapitzakis, M.K. Gaidarov,
1006 J. Phys. (London) **G25** (1999) 69.
- 1007 [37] M. Bender, K. Rutz, P.-G. Reinhard, J.A. Maruhn, W. Greiner, Phys. Rev.
1008 **C 60** (1999) 034304.
- 1009 [38] J. Decharge, J.-F. Berger, K. Dietrich, M.S. Weiss, Phys. Lett. **B451** (1999)
1010 275.
- 1011 [39] A.V. Afanasjev, S. Frauendorf, Phys. Rev. **C 71** (2005) 024308.
- 1012 [40] W.A. Richter, B.A. Brown, Phys. Rev. **C 67** (2003) 034317.
- 1013 [41] J. Friedrich, N. Voegler, Phys. Rev. Lett. **47** (1981) 1385.
- 1014 [42] P. Sarriguren, E. Moya de Guerra, and A. Escuderos, Nucl. Phys. **A658**
1015 (1999) 13; Phys. Rev. **C 64** (2001) 064306.
- 1016 [43] V.K. Lukyanov, E.V. Zemlyanaya, D.N. Kadrev, A.N. Antonov,
1017 K. Spasova, G.S. Anagnostatos, and J. Giapitzakis, Particles and Nuclei,
1018 Letters, No. 2[111] (2002) 5; Bull. Rus. Acad. Sci., Phys. **67** (2003) 790.
- 1019 [44] M. Nishimura, E. Moya de Guerra, and D.W.L. Sprung, Nucl. Phys. **A435**
1020 (1985) 523 ; J.M. Udias, M.Sc. Thesis, Universidad Autonoma de Madrid
1021 (unpublished) (1987).
- 1022 [45] T. de Forest, Jr. and J.D. Walecka, Adv. Phys. **15** (1966) 1.

- 1023 [46] G.D. Alkhazov, V.V. Anisovich, and P.E. Volkovyckii, *Diffractional Inter-*
1024 *action of Hadrons with Nuclei at High Energies*, Nauka, Leningrad (1991)
1025 94.
- 1026 [47] V.V. Burov and V.K. Lukyanov, Preprint JINR (1977) R4-11098, Dubna;
1027 V.V. Burov, D.N. Kadrev, V.K. Lukyanov, and Yu.S. Pol', Phys. At. Nu-
1028 clei **61** No.4 (1998) 525.
- 1029 [48] J. Friedrich and Th. Walcher, Eur. Phys. J. **A17** (2003) 607.
- 1030 [49] G.G. Simon, Ch. Schmitt, F. Borkowski, and V.H. Walther,
1031 Nucl. Phys. **A333** (1980) 381.
- 1032 [50] S. Galster, H. Klein, J. Moritz, K.H. Schmidt, D. Wegener, and J. Bleck-
1033 wenn, Nucl. Phys. **B32** (1971) 221.
- 1034 [51] H. Chandra and G. Sauer, Phys. Rev. **C 13** (1976) 245.
- 1035 [52] G.R. Satchler, Nucl. Phys. **A472** (1987) 215.
- 1036 [53] A. Krasznahorkay, H. Akimune, A.M. van den Berg, N. Blasi, S. Brand-
1037 denburg, M. Csatlos, M. Fujiwara, J. Gulyas, M.N. Harakeh, M. Hunyadi,
1038 M. de Hoo, Z. Mate, D. Sohler, S.Y. van der Werf, H.J. Wörtche, L. Zolnai,
1039 Nucl. Phys. **A731** (2004) 224.
- 1040 [54] K. Langanke, G. Martinez-Pinedo, P. von Neumann-Cosel, A. Richter,
1041 Phys. Rev. Lett. **93** (2004) 202501.
- 1042 [55] U. Zurmühl, P. Rullhusen, F. Smend, M. Schumacher, H.G. Börner,
1043 S.A. Kerr, Phys. Lett. **B 114** (1982) 99; Z. Phys. **A314** (1983) 171.
- 1044 [56] N. Tsoneva, H. Lenske, Prog. Part. Nucl. Phys., **59** (2007) 317.
- 1045 [57] S. Goriely, Phys. Lett. **B460** (1998) 136.
- 1046 [58] J.J. Cowan, F.-K. Thielemann, J.W. Truran, Phys. Rep. **208** (1991) 267.
- 1047 [59] Th. Weber, R.D. Heil, U. Kneissl, W. Wilke, Th. Kihm, K.T. Knöpfle,
1048 H.J. Emrich, Nucl. Phys. **A510** (1990) 1.
- 1049 [60] P.K.A. de Witt Huberts, J. Phys. **G16** (1990) 507.
- 1050 [61] J. Wesseling, C.W. de Jager, L. Lapikas, H. de Vries, M.N. Harakeh,
1051 N. Kalantar-Nayestanaki, L.W. Fagg, R.A. Lindgren, D. Van Neck,
1052 Nucl. Phys. **A547** (1992) 519.
- 1053 [62] G.J. Kramer, H.P. Blok, L. Lapikas, Nucl. Phys. **A679** (2001) 267.
- 1054 [63] D. Van Neck, M. Waroquier, J. Ryckebusch, Nucl. Phys. **A530** (1991) 347.
- 1055 [64] V.R. Pandharipande, I. Sick, and P.K.A. de Witt Huberts, Rev. Mod. Phys.
1056 **69** (1997) 981.

- 1057 [65] T. Otsuka, T. Suzuki, R. Fujimoto, H. Grawe, and Y. Akaishi,
1058 Phys. Rev. Lett. **95** (2005) 232502.
- 1059 [66] O. Benhar, D. Day, I. Sick, Rev. Mod. Phys. **80** (2008) 189.
- 1060 [67] C. Barbieri, D. Rohe, I. Sick, L. Lapikas, Phys. Lett. **B608** (2005) 47.
- 1061 [68] D. Rohe, A1 and A3 collaboration, Eur. Phys. J. **A28** (2006) 29.
- 1062 [69] J.D. Bjorken, S.K. Mtingwa, Particle Accelerators **13** (1983) 115.
- 1063 [70] E.L. Saldin, E.A. Schneidmiller, M.V. Yurkov, Nucl. Inst. Meth. **A375**
1064 (1996) 336.
- 1065 [71] M.V. Ricciardi, S. Lukić, A. Kelić, K.-H. Schmidt, M. Veselsky,
1066 Eur. Phys. J. Spec. Top. **150** (2007) 321.
- 1067 [72] H. Geissel, H. Weick, M. Winkler, G. Münzenberg, V. Chichkine, M. Yavor,
1068 T. Aumann, K.H. Behr, M. Böhmer, A. Brünle, K. Burkard, J. Benlliure,
1069 D. Cortina-Gil, L. Chulkov, A. Dael, J.-E. Ducret, H. Emling, B. Franczak,
1070 J. Friese, B. Gastineau, J. Gerl, R. Gernhäuser, M. Hellström, B. Jonson,
1071 J. Kojouharova, R. Kulesa, B. Kindler, N. Kurz, B. Lommel, W. Mit-
1072 tig, G. Moritz, C. Mühle, J.A. Nolen, G. Nyman, P. Roussel-Chomaz,
1073 C. Scheidenberger, K.-H. Schmidt, G. Schrieder, B.M. Sherrill, H. Si-
1074 mon, K. Sümmerer, N.A. Tahir, V. Vysotsky, H. Wollnik and A.F. Zeller,
1075 Nucl. Inst. Meth. **B204** (2003) 71.
- 1076 [73] K.-H. Schmidt, E. Hanelt, H. Geissel, G. Münzenberg, J.P. Dufour ,
1077 Nucl. Inst. Meth. **A260** (1987) 287.
- 1078 [74] C. J. Benesh, B. C. Cook, and J. P. Vary, Phys. Rev. **C 40** (1998) 1198.
- 1079 [75] C. Scheidenberger, H. Geissel, H.H. Mikkelsen, F. Nickel, T. Brohm, H. Fol-
1080 ger, H. Irnich, A. Magel, M.F. Mohar, G. Münzenberg, M. Pfützner,
1081 E. Roeckl, I. Schall, D. Schardt, K.-H. Schmidt, W. Schwab, M. Steiner,
1082 Th. Stöhlker, K. Sümmerer, D.J. Vieira, B. Voss, and M. We-
1083 ber, Phys. Rev. Lett. **73** (1994) 50; C. Scheidenberger, H. Geis-
1084 sel, H.H. Mikkelsen, F. Nickel, S. Czajkowski, H. Folger, H. Irnich,
1085 G. Münzenberg, W. Schwab, Th. Stöhlker, T. Suzuki, and B. Voss,
1086 Phys. Rev. Lett. **77** (1996) 3987; N. Iwasa, H. Geissel, G. Münzenberg,
1087 C. Scheidenberger, Th. Schwab, H. Wollnik, Nucl. Inst. Meth. **B126** (1997)
1088 284.
- 1089 [76] S.Y.F. Chu, L.P. Ekström and R.B. Firestone The Lund/LBNL Nuclear
1090 Data Search Version 2.0, February (1999),
1091 <http://nucldata.nuclear.lu.se/nucldata/toi/listnuc.asp?sql=&A1=1& A2=238>.
- 1092 [77] M. Steck, C. Dimopoulou, A. Dolinskii, F. Nolden, Proceedings of PAC07,
1093 Albuquerque, New Mexico, USA (2007) 1425.

- 1094 [78] J. Eichler, Th. Stöhlker, Phys. Rep. **439** (2007) 1.
- 1095 [79] Th. Stöhlker, T. Ludziejewski, H. Reich, F. Bosch, R.W. Dunford, J. Eich-
1096 ller, B. Franzke, C. Kozhuharov, G. Menzel, P.H. Mokler, F. Nolden, P. Ry-
1097 muza, Z. Stachura, M. Steck, P. Swiat, A. Warczak, and T. Winkler,
1098 Phys. Rev. **A 58** (1998) 2043.
- 1099 [80] J. Eichler and Th. Stöhlker, Hyperfine Int. **114** (1998) 277.
- 1100 [81] MEFIT B. Dreher, K. Merle, MEFCAL, University of Mainz, unpub-
1101 lished.
- 1102 [82] H. Diesener, U. Helm, G. Herbert, V. Huck, P. von Neumann-Cosel, C. Ran-
1103 gacharyulu, A. Richter, G. Schrieder, A. Stascheck, A. Stiller, J. Rycke-
1104 busch, J. Carter, Phys. Rev. Lett. **72** (1994) 1994; H. Diesener, U. Helm,
1105 P. von Neumann-Cosel, A. Richter, G. Schrieder, A. Stascheck, A. Stiller,
1106 J. Carter, Nucl. Phys. **A696** (2001) 272.
- 1107 [83] K.I. Blomqvist, W.U. Boeglin, R. Böhm, M. Distler, R. Edelhoff,
1108 J. Friedrich, R. Geiges, P. Jennewein, M. Kahrau, M. Korn, H. Kramer,
1109 K.W. Krygier, V. Kunde, A. Liesenfeld, H. Merkel, K. Merle, U. Müller,
1110 R. Neuhausen, E.A.J.M. Offermann, Th. Pospischil, A.W. Richter, G. Ros-
1111 ner, P. Sauer, S. Schardt, H. Schmieden, A. Wagner, Th. Walcher, S. Wolf,
1112 Nucl. Inst. Meth. **A403** (1998) 263.
- 1113 [84] W. Brooks and CLAS Collaboration, Nucl. Phys. **A663** (2000) 1077.
- 1114 [85] J. Friese, for the HADES collaboration, Nucl. Phys. **A654** (1999) 1017c.
- 1115 [86] The BLAST Collaboration, Technical Design Report (1997),
1116 <http://blast.lns.mit.edu/BlastNotes/>; R. Alarcon and BLAST Collabora-
1117 tion, Nucl. Phys. **A663** (2000) 1111.
- 1118 [87] The BELLE Collaboration, KEK Progress Report 2000-4,
1119 <http://beauty.bk.tsukuba.ac.jp/belle/nim/>; Nucl. Inst. Meth. **A479** (2002)
1120 117.
- 1121 [88] Rare Isotope Physics at Storage Rings,
1122 Int. Workshop, 2002, Hirschegg, Austria,
1123 <http://www-win.gsi.de/frs/meetings/hirschegg/Talks/Thursday/Blomquist.pdf>;
1124 <http://www-win.gsi.de/frs/meetings/hirschegg/Talks/Thursday/Kato.pdf>.
- 1125 [89] V. Bondarenko, B. Dolgoshein, V. Grigoriev, O. Kondratiev, A. Medvedev,
1126 S. Pavlenko, M. Potekhin, A. Romaniouk, V. Sosnovtsev, V. Tcherniatine,
1127 S. Muraviev, Nucl. Inst. Meth. **A327** (1993) 386.
- 1128 [90] J.V. Allaby, W.W. Ash, H.R. Band, L.A. Baksay, H.T. Blume, M. Bosman,
1129 T. Camporesi, G.B. Chadwick, S.H. Clearwater, R.W. Coombes,
1130 M.C. Delfino, R. de Sangro, W.L. Faissler, E. Fernández, W.T. Ford,
1131 M.W. Gettner, G.P. Goderre, Y. Goldschmidt-Clermont, B. Gottschalk,

- 1132 D.E. Groom, B.K. Heltsley, R.B. Hurst, J.R. Johnson, H.S. Kaye,
1133 K.H. Lau, T.L. Lavine, H.Y. Lee, R.E. Leedy, S.P. Leung, I. Lippi,
1134 E.C. Loh, H.L. Lynch, A. Marini, J.S. Marsh, T. Maruyama, R.L. Messner,
1135 O.A. Mayer, S.J. Michalowski, S. Morcos, J.H. Moromisato, R.M. Morse,
1136 L.J. Moss, F. Muller, H.N. Nelson, I. Peruzzi, M. Piccolo, R. Prepost,
1137 J. Pyrlik, N. Qi, A.L. Read, Jr., K. Rich, D.M. Ritson, F. Ronga,
1138 L.J. Rosenberg, W.D. Shambroom, J.C. Sleeman, J.G. Smith, J.P. Venuti,
1139 P.G. Verdini, E. von Goeler, H.B. Wald, R. Weinstein, D.E. Wisner, and
1140 R.W. Zdarko, Nucl. Inst. Meth. **A281**(1989) 291.
- 1141 [91] A1 collaboration, <http://wwwa1.kph.uni-mainz.de/A1/vdc.html>.
- 1142 [92] V. Kouznetsov, A. Lapik, S. Churikova, B. Girolami, D. Karapetiantz,
1143 Yu. Malyukin, V. Nedorezov, A. Turinge, Yu. Vorobiev, V. Abramov,
1144 A. D'Angelo, D. Moricciani, L. Nicoletti, Yu. Ranyuk, C. Schaerf,
1145 Nucl. Inst. Meth. **A487** (2002) 396.
- 1146 [93] H.W. Koch, J.W. Motz, Rev. Mod. Phys. **31** (1959) 920.
- 1147 [94] C.J. Bocchetta, A. Wrulich, Nucl. Inst. Meth. **278** (1989) 807.
- 1148 [95] K. Mengel, R. Novotny, W. Doring, V. Metag, R. Beck, H. Ströher, IEEE
1149 Trans. Nucl. Sci. **45** (1998) 681.
- 1150 [96] A.S. Brogna, S. Buzzetti, W. Dabrowski, T. Fiutowski, B. Gebauer,
1151 M. Klein, C.J. Schmidt, H.K. Soltveit, R. Szczygiel, U. Trunk
1152 Nucl. Inst. Meth. **A568** (2006) 301.
- 1153 [97] H.G. Essel, J. Hoffmann, N. Kurz, R.S. Mayer, W. Ott, D. Schall,
1154 IEEE Trans. Nucl. Sci. **43** (1996) 132;
1155 H.G. Essel, N. Kurz, IEEE Trans. Nucl. Sci. **47** (2000) 337.
- 1156 [98] Synergy Group for Front-End Electron-
1157 ics, Data Acquisition and Controls (SGFDC)
1158 <http://www.gsi.de/fair/experiments/NUSTAR/WGs/FEE-DAQ/>.
- 1159 [99] FAIR Baseline Technical Report Eds., H.H. Gutbrod, I. Augustin,
1160 H. Eickhoff, K.-D. Groß, W.F. Henning, D. Krämer, G. Walter, (2006)
1161 <http://www.gsi.de/fair/reports/btr.html>.

Referee #1

>{1}

We have discussed the text (again) with experts in the field of electron scattering. We follow the suggestion of our referee and have rewritten the elastic scattering paragraph accordingly.

>{2}

>The authors insist on their "azimuthal-polar"-nomenclature - for what?
>In lines [597] the nomenclature "azimuthal-polar" refers to the scattering
>process and, without any problem, they could replace here "polar angle"
>by "scattering angle".

After careful reading the referee's remarks regarding the coordinate system(s) in this and previous communications, we come to the conclusions that the referee is not appreciating that we are using two different coordinate systems, a polar coordinate system for the scattering process and a rectangular coordinate system for the spectrometer, both indicated by their respective symmetries.

We agree with the referee's previous statement that the polar coordinate system (with polar and azimuthal coordinates) is appropriate for the scattering process where the polar angle is the scattering angle. We formulate our kinematics (see Table 3) in this system as usually done. This answers the question of the referee: 'The authors insist on their "azimuthal-polar"-nomenclature - for what?'

>In lines [615] to [629] they use the nomenclature "vertical" and "horizontal".

Considering the previous statement of the referee: 'The focussing of a spectrometer, however, does not know about them (referring to the polar and azimuthal coordinates). The spectrometer only knows about "dispersive" and "non dispersive" or "in plane" and "out of plane" angles.'

Of course, the spectrometer does not know about this, as the referee points out. We are using a different coordinate system for the spectrometer as mentioned above. The rectangular coordinate system with a 'horizontal' and 'vertical' coordinate, defined by the angles at the entrance of the spectrometer, is clearly introduced in lines [615] -- [629] and is commonly used. These are the same coordinates that the referee calls 'in plane/out of plane', another accepted notation. We, therefore, see nothing wrong with our notation. The suggested use of 'dispersive/non dispersive' does not work here, because the ELISE spectrometer has both a horizontal (PD) and a vertical (VM) dispersion component, using a curvilinear coordinate system as being commonly used in ion-optics.

>In lines [631] to [638] they use the term "polar angle" again as synonym
>for (horizontal) scattering angle.

We are discussing here the need to measure at smaller polar (= scattering) angles in cylindrical symmetry, and how this is achieved using a horizontally slim Panofsky quadrupole as illustrated in Fig. 8. So here, we describe the

scattering process in the spirit of the referee and hereafter refer to constraints in our optical system.

>In line [667] they write "polar scattering angle".

This was obviously written with the intent to suggest the equality of polar angle and the scattering angle. We will make changes to clarify at the beginning of our manuscript that the polar angle is the scattering angle.

>The decisive sentence is in line [670ff]: "Electrons that are elastically
>scattered to the same polar angle but with different azimuthal angles are
>focused in the focal plane of the spectrometer." Do they really think here
>of the same "azimuthal angle" as the one they are thinking of in line [598]
>and which can go up to 2π ? If that is really the case, then I don't
>understand, how this azimuthal angle can be focussed by the spectrometer,
>if the polar angle is only 10° .
>I rather suppose that they are thinking here of the vertical angle, the
>nomenclature they have used in between. Or is it, that I don't understand
>the action of the pre-deflection magnet?

The notion of horizontal focus is the first order property $R_{12} = 0$ of an ion-optical system from target (tgt) to focal plane (fp) with $x_{fp} = R_{12} \cdot x_{tgt}$, with x = horizontal position. Like most spectrometers also this one will be carefully design and aligned to decouple the horizontal and vertical planes, Therefore, the azimuthal angle will not affect the horizontal properties. So the statement is correct. Everybody who takes data at and near 0 degree will see the (horizontal) focus for all polar (scattering) angles. This is shown e.g. in Fig 7 in Phys. Rev. C 75 (2007) 034310 by Fujita et al.. We will support this statement by an additional Figure that we will send by email to the editor. Therefore, replacing 'azimuthal' with 'vertical', as the referee suggests, would not make sense. The main purpose of the pre-deflector is not the focusing property, but to provide at its exit parallel central rays.

One last remark should be made. The referee misunderstands our expertise by writing in his previous email 'When the authors will start to analyse data, they will (hopefully) realize the difference. Till then, there will be much time left and they might leave the text as it is, though I think they better change their nomenclature (and, may be, their way to look at the angles'.

Those of us who are analyzing spectrometer data all the time at and near 0 degree are reconstructing the scattering angle from the coordinates of the detectors to be able to derive correct cross section angular distributions to be compared to the theory and models. In this article our discussion on the basis of extensive Monte-Carlo simulations is concerned with the precision of the spatial and angular measurements that are required to be able to make the transformation precisely between the measured coordinates and the scattering angle and of course to provide the high resolution.

We think our manuscript in respect to coordinate systems and ion-optics is correct and we cannot help the referee with any substantial modification as explained. In the process of clarifying this, we have found that we can improve in some cases the use of our notations for the sake of clarity. These modifications are:

Line [377] Insert the sentence: The scattering process is described in a polar coordinate system with the axis along the electron beam axis where the polar angle is the scattering angle θ .

Line [599]: Repl. 'in polar angle' by 'in scattering angle'

Line [631]: Repl. 'a polar angle' by 'a scattering angle'

Line [632]: Repl. 'In order to increase the polar-angle range, the ...' by 'In order to allow measurements at small scattering angles, the ...'

Line [638]: Repl. 'minimal polar angle' by 'minimal scattering angle'

Line [655]: Repl. 'a range of polar angles' by 'a range of scattering angles'

Line [658]: Repl. 'range of polar angles' by 'range of scattering angles'

Line [667]: Repl. 'for polar scattering angles' by 'for scattering angles'

Line [813]: Repl.: 'minimum polar angle' by 'minimum scattering angle'

>{3}

"transition" changed to "state"

>{4}

We have clarified the role of the exponential tail according to the referee's comment.

>{5}

We thank the referee for his criticism here. We have chosen a better example, namely the one we beared originally in mind when discussing this for ELISE's physics case.

Referee #2:

We thank the referee for his constructive remarks and have removed the errors that were pointed out.

- * Line 552: typo: 'density'
- * Lines 667 and 675. In line 667 the polar scattering angle ranges from 10 to 60 degree. But in line 675 an upper angle of 62.82 degree is given which is outside the above range. I guess that the angles given in 667 are approximate values. This should be stated.
- * Line 693 and 697: I propose to change 'z' to 'z(IP)' to be consistent with the label on the vertical axis of Fig. 11 (right panel)
- * Figure 14, caption: 'Showers' should be replaced by 'Shower' (only one shower created by one gamma ray is shown)
- * Line 871: For the same reason I propose to delete 'distribution'
- * Line 976: delete 'future.'
- * Lines 985 and 987: inconsistent: once 'Ann.', once 'Annu.'
- * Lines 986, 1039: no comma after journal
- * Line 1013: for consistency the page nr. should appear after the year
- * Line 1061: period after 'J'

1 The Electron-Ion Scattering experiment ELISe at the
2 International Facility for Antiproton and Ion Research
3 (FAIR) - a conceptual design study

4 A.N. Antonov, M.K. Gaidarov, M.V. Ivanov, D.N. Kadrev

5 *INRNE-BAS Sofia - Bulgaria*

6 M. Aïche, G. Barreau, S. Czajkowski, B. Jurado

7 *Centre d'Etudes Nucléaires Bordeaux-Gradingnan (CENBG) - France*

8 G. Belier, A. Chatillon, T. Granier, J. Taieb

9 *CEA Bruyères-le-Châtel - France*

10 D. Doré, A. Letourneaux, D. Ridikas, E. Dupont, E. Berthoumieux,
11 S. Panebianco

12 *CEA Saclay - France*

13 F. Reymund, C. Schmitt

14 *GANIL Caen - France*

15 L. Audouin, E. Khan, L. Tassan-Got

16 *IPN Orsay - France*

17 T. Aumann, P. Beller[†], K. Boretzky, A. Dolinskii, P. Egelhof, H. Emling,
18 B. Franzke, H. Geissel, A. Kelic-Heil, O. Kester, N. Kurz, Y. Litvinov,
19 G. Münzenberg, F. Nolden, K.-H. Schmidt, H. Simon, M. Steck, H. Weick

20 *GSI Darmstadt - Germany*

21 J. Enders, N. Pietralla, A. Richter, G. Schrieder

22 *TU Darmstadt - Germany*

23 A. Zilges

24 *University of Cologne - Germany*

25 M.O. Distler, H. Merkel, U. Müller

26 *Johannes Gutenberg University of Mainz - Germany*

27 A. Junghans

28 *FZ Dresden - Germany*

Email address: H.Simon@gsi.de (H. Simon)

29
30
31
32
33
34
35
36
37
38
39
40
41
42
43
44
45
46
47
48
49
50
51
52
53
54
55
56
57
58
59

H. Lenske

Justus-Liebig University Giessen - Germany

M. Fujiwara

RCNP Osaka - Japan

T. Suda

RIKEN - Japan

S. Kato

Yamagata University - Japan

T. Adachi, S. Hamieh, M.N. Harakeh, N. Kalantar-Nayestanaki, H. Wörtche

KVI, University of Groningen - The Netherlands

G.P.A. Berg

KVI, University of Groningen - The Netherlands &

Department of Physics and JINA, University of Notre Dame , USA

I.A. Koop, P.V. Logatchov, A.V. Otboev, V.V. Parkhomchuk, D.N. Shatilov,
P.Y. Shatunov, Y.M. Shatunov, S.V. Shiyankov, D.I. Shvartz, A.N. Skrinsky

BINP Novosibirsk - Russia

L.V. Chulkov, B.V. Danilin[†], A.A. Korshennikov, E.A. Kuzmin,
A.A. Ogloblin, V.A. Volkov

RRC Kurchatov Institute Moscow - Russia

Y. Grishkin, V.P. Lisin, A.N. Mushkarenkov, V. Nedorezov, A.L. Polonski,
N.V. Rudnev, A.A. Turlin

INR Moscow - Russia

A. Artukh, S.N. Ershov, A. Fomichev, M. Golovkov, A.V. Gorshkov,
L. Grigorenko, S. Klygin, S. Krupko, I.N. Meshkov, A. Rodin, Y. Sereda,
I. Seleznev, S. Sidorchuk, E. Syresin, S. Stepantsov, G. Ter-Akopian,
Y. Teterev, A.N. Vorontsov

JINR Dubna - Russia

S.P. Kamerdzhiev, E.V. Litvinova

IPPE Obninsk - Russia

S. Karataglidis

Rhodes University - Faculty of Science - South Africa

60 R. Alvarez Rodriguez, M.J.G. Borge, C. Fernandez Ramirez, E. Garrido,
61 P. Sarriguren, J.R. Vignote

62 *CSIC Madrid - Spain*

63 L.M. Fraile Prieto, J. Lopez Herraiz, E. Moya de Guera, J. Udias-Moinelo

64 *Complutense University of Madrid - Spain*

65 J.E. Amaro Soriano, A.M. Lallena Rojo

66 *Granada University - Spain*

67 J.A. Caballero

68 *Seville University - Spain*

69 H.T. Johansson, B. Jonson, T. Nilsson, G. Nyman, M. Zhukov

70 *Chalmers University of Technology - Sweden*

71 V. Avdeichikov

72 *Lund University - Sweden*

73 K. Hencken, J. Jourdan, B. Krusche, T. Rauscher, D. Kiselev, D. Trautmann

74 *University of Basel - Switzerland*

75 J. Al-Khalili, W. Catford, R. Johnson, P. Stevenson

76 *University of Surrey - United Kingdom*

77 C. Barton, D. Jenkins

78 *University of York - United Kingdom*

79 R. Lemmon

80 *CCLRC Daresbury - United Kingdom*

81 M. Chartier

82 *University of Liverpool - United Kingdom*

83 D. Cullen

84 *University of Manchester - United Kingdom*

85 C.A. Bertulani

86 *Texas A&M University Commerce - USA*

87 A. Heinz

88 *Yale University - USA*

89 **Abstract**

The electron-ion scattering experiment ELISe is part of the installations envisaged at the new experimental storage ring at the international Facility for Antiproton and Ion Research (FAIR) in Darmstadt, Germany. It offers a unique opportunity to use electrons as probe in investigations of the structure of exotic nuclei. The conceptual design and the scientific challenges of ELISe are presented.

90 *Keywords:* eA collider, electron scattering, nuclei far off stability

91 *PACS:* 29.27.-a, 25.30.Bf, 25.30.Dh, 21.10.Ft, 29.20.Dh, 29.30.-h

92 **1. Introduction**

93 The Facility for Antiproton and Ion Research (FAIR) is scientifically and
94 technically one of the most ambitious projects worldwide. It has a broad sci-
95 entific scope allowing forefront research in different sub-disciplines of physics.
96 Because of its great potential for discoveries, the FAIR project has been given
97 highest priority in the NuPECC Long-Range Plan 2004 [1]. One of the sci-
98 entific pillars of FAIR is nuclear-structure physics and nuclear astrophysics with
99 radioactive ion beams. The proposed electron-ion collider (eA Collider) con-
100 sisting of the New Experimental Storage Ring (NESR) and the Electron and
101 Antiproton Ring (EAR) will allow a range of novel studies with stored and
102 cooled beams.

103 The use of electrons as probe provides a powerful tool for examining nuclear
104 structure. The most reliable picture of nuclei originates in electron scatter-
105 ing. The increasing number of publications devoted to theoretical treatments of
106 electron scattering off exotic nuclei [2, 3, 4, 5, 6, 7, 8, 9, 10, 11, 12, 13, 14] sup-
107 ports this assertion and underlines the usefulness of an electron-ion scattering
108 setup for unstable nuclei. However, up to now, this technique is still restricted
109 to stable isotopes. The Electron-Ion Scattering experiment (ELISe) aims at
110 an extension of this powerful method to radioactive nuclei outside the valley
111 of stability. ELISe will be a unique and unprecedented tool for precise mea-
112 surements of nuclear-charge distributions, transition charge and current matrix
113 elements, and spectroscopic factors. This capability will contribute to a variety
114 of high-quality nuclear-structure data that will become available at FAIR.

115 A first technical proposal for an electron-ion collider was made almost twenty
116 years ago at the Joint Institute for Nuclear Research (Dubna) [15]. The ideas
117 of this proposal have been incorporated in and further developed at the RIKEN
118 Rare-Isotope Beam Factory (RIBF) for the so-called Multi-USE Experimental
119 Storage rings (MUSES) [16], as well as at the planned eA collider at FAIR,
120 under the name ELISe [17, 18, 19, 20, 21]. However, none of these projects
121 has been realized up to now. For the RIBF, an alternative setup called SCRIT
122 (Self-Contained Radioactive Ion Target) has been proposed [22]. In SCRIT a

123 circulating beam of electrons scatters off ions stored in a trap. Within foresee-
124 able future, ELISe could be the first and only eA collider for radioactive ion
125 beams worldwide. The ELISe setup provides easy access to different types of
126 electron-nucleus reactions in experiments where scattered electrons are detected
127 in coincidence with reaction products.

128 A cooled beam consisting of radioactive ions stored in the NESR will be
129 brought to collision with an intense electron beam circulating in EAR at the
130 interaction point (IP). Here, a magnetic spectrometer for the detection of scat-
131 tered electrons as well as detector systems for the measurements of reaction
132 products are to be installed.

133 This paper is organized as follows. It describes the physics case for ELISe and
134 explains the conditions and requirements for performing different experiments.
135 We explain the difference between fixed target and colliding beam kinematics
136 and outline the planned design and predicted performance of the eA collider.
137 The major components of ELISe, being planned as multi-purpose setup for these
138 experiments, i.e. an electron and in-ring spectrometer, as well as a luminosity
139 monitor, are characterized and viable concepts for their design are presented.

140 **2. Research objectives**

141 The central goal in nuclear physics is the construction of a theoretical frame-
142 work capable of describing consistently all nuclear systems from the deuteron
143 two-body case to infinite nuclear matter, going through every finite nucleus
144 with its many degrees of freedom and modes of excitation and decay. This
145 ambition is also the driving force for experimental investigations of nuclei near
146 the limits of stability. In the past two decades, substantial progress towards
147 this goal has been made due to the progress in developments of radioactive
148 beams. Intensive studies of the structure of nuclei near the drip lines are car-
149 ried out at several laboratories as GSI in Darmstadt (Germany), GANIL in
150 Caen (France), ISOLDE at CERN (Switzerland), JINR in Dubna (Russia),
151 NSCL at Michigan State University (USA) and RIKEN (Japan). The studies
152 involve nucleus-nucleus or nucleon-nucleus interactions as well as decay studies
153 and different means to determine their ground state properties. Building on
154 the great progress in the experimental and theoretical investigations (see, for
155 example, the reviews [23, 24]), novel experimental methods and observables will
156 most certainly enhance the opportunities leading to a better understanding of
157 the structure of nuclei near the limits of stability and in general.

158 Electron scattering, as in ELISe, offers unique and widely recognized ad-
159 vantages for the study of nuclear structure (see reviews [25, 26, 27, 28, 29]).
160 Interactions with electrons are well described by the most accurate theory in
161 physics - quantum electrodynamics (QED). The coupling is weak, so that mul-
162 tiple scattering effects are strongly suppressed, such that perturbations of the
163 initial state of the nucleus are minimal. The ability to vary momentum and
164 energy transferred to the nucleus, independently, allows mappings of spatial dis-
165 tributions of the constituent particles. Since electrons are point particles, they
166 offer excellent spatial resolution, and can additionally be tuned to the scale of a

167 process under study. Electron scattering, as it will be performed at ELISE, will
 168 thus add important new observables to investigate radioactive nuclear species.

169 To mention selected physics aspects (see also Table 1), these experiments
 170 will give access to

- 171 • charge-density distributions, in particular root-mean-square (r.m.s.) radii,
 172 of exotic nuclei from elastic electron scattering,
- 173 • new specific collective modes of excitation with selectivity to multipolarities
 174 via inelastic electron scattering, and
- 175 • internal nucleon-nucleon correlations and nuclear structure from quasi-free
 176 scattering, such as nucleon ($e, e'N$) or cluster ($e, e'c$) knockout.

177 *2.1. Elastic electron scattering: charge density distributions, charge radii*

178 Neglecting Coulomb distortion, i. e. in first order Born approximation (BA),
 179 the cross section for the scattering of an electron off a nucleus is given by

$$d\sigma/d\Omega = d\sigma/d\Omega_{\text{Mott}} F^2(q). \quad (1)$$

180 Here $d\sigma/d\Omega_{\text{Mott}}$ is the cross section in BA for the scattering off a point nu-
 181 cleus with spin zero and $F(q)$ is the form factor, which contains the information
 182 about the nuclear charge distribution $\rho(r)$. To be specific: The form factor is
 183 the Fourier transform of the latter.

184 Since BA is not sufficiently precise for the scattering off nuclei with larger Z ,
 185 the cross section has to be calculated by solving the Dirac equation numerically
 186 with the Coulomb potential from $\rho(r)$, for which an ansatz has to be made for
 187 this purpose. The common method is the calculation of the phase shifts of the
 188 electron wave in the Coulomb potential of $\rho(r)$ [30], it is therefore called "phase
 189 shift" or, thinking of the distorted electron waves, "DW" method.

190 The charge distribution is determined from measured cross sections by fitting
 191 the free parameters of the ansatz for $\rho(r)$ to the data. Several aspects of the
 192 information gained by such experiment are easier to catch by looking at the
 193 form factor (some details of how one gets it will be discussed in section 4.2).

194 The existing information on charge densities obtained from electron scatter-
 195 ing experiments for more than 300 nuclides is reviewed in [31, 32]. These data,
 196 confined to the valley of stability, show oscillations in r.m.s. radii, surface thick-
 197 nesses, and interior densities as a function of atomic number [33, 34]. The r.m.s.
 198 charge radius, can be extracted in a model-independent way from experimental
 199 data at low q from the expansion

$$F_{\text{ch}}(q) \sim 1 - \frac{\langle r^2 \rangle}{3!} q^2 + \frac{\langle r^4 \rangle}{5!} q^4 + \dots \quad (2)$$

200 The surface thickness, defined as the distance where $\rho_{\text{ch}}(r)$ drops from 90% to
 201 10% of its central value, is also accessible from the extracted form factor. For
 202 unstable nuclei, no data on the shapes of the nuclear surfaces exist, and here
 203 ELISE could provide a first insight. A central-density depression was observed

204 in several nuclei [35], even including light nuclei [36]. Such a depression is pre-
 205 dicted for proton-rich [12, 14] and superheavy [37, 38, 39] nuclei. The origin of
 206 this is due to Coulomb effect, the underlying shell and single particle structure
 207 as well as short-range correlations (see for example Ref. [35, 40] and references
 208 therein). The systematics of the charge-density distributions with the inclusion
 209 of nuclei having extreme proton-neutron asymmetry forms a basis for investiga-
 210 tions addressing both the structure of nuclei and the properties of bulk nuclear
 211 matter. An example of the latter is the determination of nuclear compressibility
 212 from experimental nuclear radii and binding energies [41].

213 The most realistic description of elastic electron-scattering cross sections can
 214 be achieved by solving the Dirac equation, and performing an exact phase-shift
 215 analysis [30]. This method has been chosen, e.g. in Ref. [7]. Using the DW
 216 method, the modulus of the charge form factor can be determined from the
 217 differential cross section. Its sensitivity to changes in the charge distribution
 218 is demonstrated in Fig. 1, taken from Ref. [7], where Ni isotopes are shown
 219 as example. The proton densities presented in Fig. 1 were obtained from self-
 220 consistent HF+BCS mean-field calculations with effective NN interactions in
 221 a large harmonic-oscillator basis [42] by using a density-dependent Skyrme pa-
 222 rameterization. In the same figure, the squared moduli of charge form factors,
 223 which are obtained from solving the Dirac equation numerically, are presented.
 224 Following this prescription, electron scattering is computed in the presence of a
 225 Coulomb potential induced by the charge distribution of a given nucleus. The
 226 intrinsic charge distribution of the neutron is included into these calculations.
 227 Two codes were used for the numerical evaluation of the form factors: the first is
 228 taken from Ref. [43] which follows Ref. [30] and the second has been discussed in
 229 Ref. [44]. The results of both calculations were found to be in good agreement.
 230 The nuclear charge form factor $F_{ch}(q)$ has been calculated as follows

$$F_{ch}(q) = \left[F_{point,p}(q)G_{Ep}(q) + \frac{N}{Z}F_{point,n}(q)G_{En}(q) \right] F_{c.m.}(q), \quad (3)$$

231 where $F_{point,p}(q)$ and $F_{point,n}(q)$ denote the form factors related to the point-like
 232 proton and neutron densities $\rho_{point,p}(\mathbf{r})$ and $\rho_{point,n}(\mathbf{r})$, respectively [7]. These
 233 densities correspond to wave functions where the positions \mathbf{r} of the nucleons are
 234 defined with respect to the center of the potential in the laboratory system. In
 235 order to let $F_{ch}(q)$ correspond to the density distributions in the center-of-mass
 236 coordinate system, a factor $F_{c.m.}(q)$ is introduced (e.g. [45, 46, 47]) in two
 237 commonly used ways:

$$F_{c.m.}(q) = e^{(qR)^2/6A}, \quad (4)$$

238 where R stands for the root-mean square radius of the nucleus, or

$$F_{c.m.}(q) = e^{(qb)^2/4A}, \quad (5)$$

239 where b denotes the harmonic-oscillator parameter. For shell-model potentials
 240 different from harmonic-oscillator, Eqs. (4) and (5) are approximations.

241 Equation (3) with a c.m. correction of form (4) [47] was used to compute
 242 the modulus squared of the form factor that can be extracted also from experi-
 243 mental data. In Eq. (3) $G_{Ep}(q)$ and $G_{En}(q)$ denote Sachs proton and neutron
 244 electric form factors, respectively, and are taken from one of the most recent
 245 phenomenological parameterizations [48]. Actually, there is no significant dif-
 246 ference between this recent parameterization and the most traditional one of
 247 Refs. [49, 50, 51] for the momentum-transfer range considered in this work
 248 ($q < 4 \text{ fm}^{-1}$).

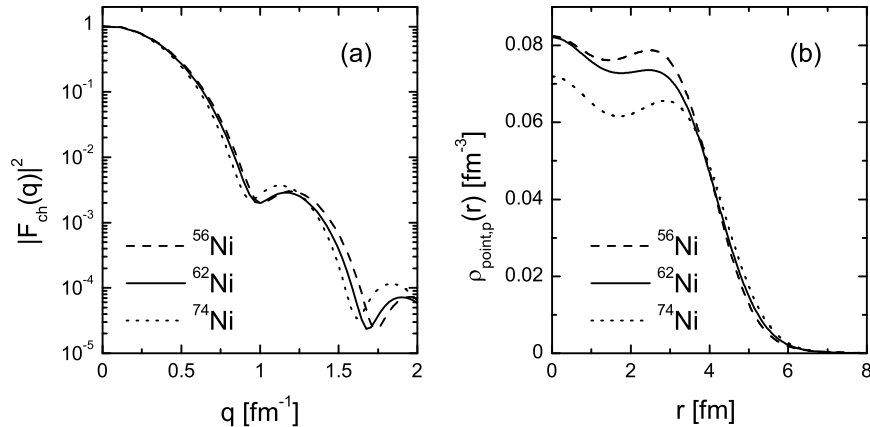


Figure 1: Modulus squared of charge form factors (panel (a)) calculated by solving the Dirac equation with HF+BCS proton densities (panel (b)) for the unstable doubly-magic ^{56}Ni , stable ^{62}Ni and unstable ^{74}Ni isotopes [7]. In the calculation of the moduli, the intrinsic charge distribution of the neutron was taken into account; see text for more details.

249 In general, it has been found that with increasing number of neutrons in a
 250 given isotopic chain the the minima of the curves of the charge form factor are
 251 shifted towards smaller values of the momentum transfer [7]. This is due mainly
 252 to the enhancement of the proton densities in the peripheral region and to a
 253 minor extent to the contribution from the charge distribution of the neutrons
 254 themselves. By accounting for the Coulomb distortion of the electron waves, a
 255 filling of the Born zeros is observed when the DW method is used (in contrast
 256 to plane-wave Born approximation).

257 As evident from Eq. (2), the r.m.s. radius is accessible from measurements
 258 at very low q -values where the cross sections are large. An accurate determi-
 259 nation of the charge distributions to e.g. extract the surface thickness from
 260 measured differential cross sections, requires a high precision measurement in a
 261 wide region of transferred momentum, at least up to the second maximum. As
 262 a further example, we quote the formation of so-called bubbles in exotic nuclei
 263 as discussed in Ref. [12], where the depletion of the central part of the charge
 264 distribution is attributed to a depopulation of s -states. It is also argued that

265 cross-section measurements to the second form-factor minimum, already pro-
266 vide information on the depletion of the central density. The data obtainable
267 with ELISE can provide for the first time precise information on the charge dis-
268 tribution of radioactive nuclei through form-factor measurements. These data
269 could subsequently be used to benchmark theoretical models for the structure
270 of exotic nuclei.

271 *2.2. Inelastic scattering: giant resonances, decay channels, astrophysical appli-* 272 *cations*

273 Inelastic electron scattering has proven to be a powerful tool for studying
274 properties of excited states of nuclei, in particular their spins, parities, and
275 the strength and structure of the transition densities connecting the ground
276 and excited states (see e.g. Ref. [25]). Although important information also is
277 available from other types of experiments, as for example, hadron scattering,
278 pickup and transfer reactions, charge-exchange reactions, the electron-scattering
279 method has unique features. This is the only method which can be used to
280 determine the detailed spatial distributions of the charge transition densities
281 for a variety of single-particle and collective transitions. These investigations
282 provide a stringent test of the nuclear many-body wave functions [26, 27].

283 Due to its strong selectivity, collective and strong single-particle excitations
284 can be studied particularly well in electron scattering. Electric and magnetic
285 giant multipole resonances are of special interest, and several of them have been
286 discovered and studied using electron scattering (see Ref. [28] and references
287 therein).

288 When approaching the neutron drip-line, there is a characteristic increase in
289 the difference between neutron and proton density distributions. Apart from di-
290 rect measurements using elastic scattering as described in the last section, where
291 electron and hadron scattering results are combined to extract the neutron-skin
292 density distribution, also complementary indirect methods are available. The
293 difference in radii of the neutron and proton density distributions is accessi-
294 ble via studies of giant dipole resonances (GDR) by inelastic scattering of an
295 isoscalar probe or spin- dipole resonances by charge-exchange reactions. The
296 cross section of these processes strongly depends on the relative neutron-skin
297 thickness [52, 53]. This quantity is of great importance due to direct relations
298 between the neutron-skin thickness and properties of the nuclear matter EOS
299 such as the symmetry-energy coefficient and the nuclear incompressibility. The
300 energy of the isoscalar giant monopole-resonance can be used to deduce the
301 compressibility of nuclear matter, which is directly related to the curvature of
302 the EOS. Hence data from inelastic electron scattering can provide an indepen-
303 dent test of this quantity in addition to those obtained from the nuclear radius
304 (elastic scattering) and the binding energy (see Ref. [41]). Magnetic dipole exci-
305 tations (M1) arise due to changes in the spin structure of the nucleus and orbital
306 angular motion of its constituents. Along with decay studies, the measured M1
307 distributions from electron scattering could provide information about the nu-
308 clear Gamow-Teller strength distribution. The latter is important for reliably
309 extracting inelastic neutrino-nucleus cross sections [54], which are important

310 in certain astrophysical scenarios, such as neutron stars or core-collapse super-
311 novae.

312 The low-energy dipole strength located close to the particle-emission thresh-
313 old is a general feature in many isospin-asymmetric nuclei [55]. This mode is
314 known as the Pygmy Dipole Resonance (PDR), and has been explained as being
315 generated by oscillations of weakly bound neutrons with respect to the isospin
316 symmetric core in neutron-rich nuclei (see Review [56]). Thus, in exotic nuclei
317 the PDR modes should be especially pronounced.

318 The origin of approximately one half of the nuclides heavier than iron ob-
319 served in nature is explained by the r-process. The existence of pygmy reso-
320 nances has important implications on theoretical predictions of radiative neutron-
321 capture rates in the r-process nucleosynthesis, and consequently on the calcu-
322 lated elemental abundance distribution in the universe. This was studied using
323 calculations and fits to the properties of neutron-rich nuclei involved in this
324 process [57]. The inclusion of the PDR increases the r-process abundance-
325 distributions for nuclei around $A = 130$ by about two orders of magnitude
326 (Fig. 6 in [57]) as compared with the case where only the GDR was taken into
327 account. The result of the calculations strongly depends on the competition
328 between the open decay channels.

329 In heavy nuclei, the r-process path is expected to be limited by fission, and
330 the fission process is treated only very schematically in network calculations.
331 Therefore electro-induced fission giving access to a multipole decomposition of
332 the fission cross sections will allow to refine models of the fission process, to
333 study the nuclear structure involved, and to serve as an improved input for r-
334 process calculations [58] since fission is one of the decay channels of the excited
335 nucleus. ELISe will be an ideal experiment for electro-fission studies. Mea-
336 surements of coincidences between the scattered electron and the nuclear decay
337 products represent the most powerful tool available for precise determinations
338 of multipole excitation functions even when the resonance strength is spread
339 over a wide excitation energy range [59]. The proton and neutron numbers of
340 fission fragments and their kinetic energies as a function of the excitation energy
341 can be determined. Such complete experimental information will enable, for the
342 first time, studies of the influences of neutron and proton shells as well as of
343 pairing correlations on fission dynamics. Also, fission barriers of exotic nuclei
344 can be determined precisely.

345 *2.3. Quasi-free scattering (QFS): shell structure, spectral functions, spectro-* 346 *scopic factors*

347 High-resolution exclusive ($e, e'p$) experiments offer the possibility to study
348 individual proton orbits [60, 61, 62]. In Ref. [61] the momentum distribution for
349 'single'-particle states were thus determined. These were fitted by combinations
350 of bound-state wave-functions generated in a Woods-Saxon potential. Thereby,
351 the r.m.s. charge radii and the depletion of the spectroscopic factors could be de-
352 termined. This can be used to observe knockout from regions inside the nucleus
353 with essentially different densities. The observed spectroscopic strength for va-
354 lence shells, obtained with ($e, e'p$) reactions, are surprisingly small, sometimes

355 by 30-50%, compared to values of shell model calculations. It is believed that
 356 this is due to effects of short-range correlations [63, 64]. For asymmetric nuclei
 357 neutron-proton interactions lead to a reordering of shells [65]. It is therefore
 358 important also to characterize deeper lying levels. Measured momentum dis-
 359 tributions will help to identify the angular momentum and quantum numbers
 360 of the involved shells. Effects of final-state interactions and meson-exchange
 361 currents can be substantially reduced by choosing parallel kinematics [67, 68].
 362 The quasi-free ($e, e' p$) scattering-condition $Q^2/2m\omega_0 \approx 1$ in the eA collider¹–
 363 where Q denotes the four momentum transfer and ω_0 the energy loss– can be
 364 realized already at moderately forward scattering angles between 50° and 60° .
 365 Exclusive measurements should therefore be possible for light elements, where
 366 the achievable luminosities are close to $10^{29} \text{ cm}^{-2}\text{s}^{-1}$, as will be shown later in
 367 this paper. Occupation probabilities and spectroscopic factors can be obtained
 368 in the region of resolved states. Another access to correlations in the nuclear
 369 interior is provided by cluster knock out ($e, e'c$) [3] that yields information on
 370 momentum distributions and cluster spectroscopic factors of clusters inside nu-
 371 clei.

372 In inclusive electron scattering in the quasi-free region, an average over all
 373 available orbits can be measured [66] by the shape of the obtained spectrum.
 374 Inclusive measurements are likely to be feasible for medium and heavy nuclei at
 375 achievable luminosities of $10^{28} \text{ cm}^{-2}\text{s}^{-1}$.

376 3. Kinematics of colliding beams

377 This section describes the kinematics of colliding beams and the design pa-
 378 rameters of the electron spectrometer. It is compared to a conventional labo-
 379 ratory system where the electron beam strikes a fixed target. The scattering
 380 process is described in a polar coordinate system with the axis along the elec-
 381 tron beam axis where the polar angle is the scattering angle θ . In the following,
 382 this system is referred to as kinematics F. The boosted center-of-mass (c.m.) of
 383 the colliding beams into the laboratory frame leads to kinematical conditions
 384 that are very different compared to conventional experiments.

385 The equations in this section are calculated in the limit of zero electron mass.
 386 In this limit the total energy of the electron is equal to its kinetic energy and
 387 momentum ($E_e = T_e = p_e$)². The numerical estimates given in this section
 388 assume counter-propagating i.e. colliding beams of 0.74 GeV/nucleon ions and
 389 0.5 GeV electrons (referred to as kinematics C). The energy of electrons in
 390 kinematics F corresponding to that of colliding beam kinematics in the c.m. is

¹For the simulation calculation (QFS on ^{12}C), going beyond the scope of this work, ω_0 was taken to be 135 MeV. Protons are then emitted in backward direction in a small cone with angles ranging from 160° to 165° . The required proton resolution for resolving states varies from about 1 % to 3 % at 300 MeV and 800 MeV, respectively. The $A - 1$ -Fragments fall within the acceptance of the in-ring spectrometer, described later in this paper.

²Natural units $c = 1$, $\hbar = 1$ are used in the following.

Table 1: Required luminosities for different studies. The achievable values predicted for the ELISE setup will be discussed in section 4 on page 14. The given values are based on rate estimates for – at most – 4 week measurements.

Reaction	Deduced quantity	Target nuclei	Luminosity $\text{cm}^{-2}\text{s}^{-1}$
elastic scattering at small q	r.m.s. charge radii	light	10^{24}
		medium	
first minimum in elastic form-factor	density distribution with 2 parameters	light	10^{28}
		medium	10^{26}
		heavy	10^{24}
second minimum in elastic form-factor	density distribution with 3 parameters	medium	10^{29}
		heavy	10^{26}
giant resonances	position, width, strength, decays	medium	10^{28}
		heavy	10^{28}
quasi-elastic scattering	spectroscopic factors, spectral function, momentum distributions	light	10^{29}

391 given by

$$T_e(F) = \sqrt{\frac{1+\beta}{1-\beta}} T_e(C), \quad (6)$$

392 where $\beta = p_A/E_A$ is the ion velocity. Thus, a 0.5 GeV electron in kinematics C
393 corresponds to a 1.64 GeV electron in kinematics F.

394 Table 2 gives the kinematical equations for two types of kinematics for an
395 electron scattering experiment. It can be shown that while the energy of elasti-
396 cally scattered electrons in kinematics F is almost independent of the scattering
397 angle, the electron energy in kinematics C depends strongly on scattering angle
398 and increases from $p_{e'} = p_e$ to $p_{e'} \approx (1+\beta)/(1-\beta)p_e$ when the angle increases
399 from 0° to 180° , i.e. from 0.5 GeV at zero degree to ≈ 5 GeV in backward
400 direction. Furthermore, while in kinematics F the energy separation between
401 elastically and inelastically scattered electrons is approximately equal to the
402 excitation energy (E^*) of the recoiling ion, in kinematics C this separation is
403 reduced by a factor of $\sqrt{(1-\beta)/(1+\beta)} \approx 0.3$.

404 These two features of kinematics C make it difficult to resolve elastically and
405 inelastically scattered electrons³.

³Table 2 demonstrates that the separation between elastic and inelastic peaks in the spec-
trum is much larger in the case of co-propagating beams. However, several other parameters
are not in favor of this geometry. For example, the length \mathcal{L} of interaction zone (IZ) is deter-
mined by $\mathcal{L} \approx l/(1\pm\beta)$, where l is the ion-bunch length, + corresponds to counter-propagating
beams and – to co-propagating beams. For co-propagating beams $\mathcal{L} = 50$ cm, which is ten

Table 2: Kinematics of colliding beams. Here, p_e , $p_{e'}$ are the momenta of incoming and scattered electrons, θ is the electron scattering angle relative to the electron beam direction, $\beta = p_A/E_A$, $\delta = \sqrt{(1-\beta)/(1+\beta)}$, $E_A = \sqrt{M^2 + p_A^2}$ is the total energy of incident ions, and E^* the excitation energy of the recoil ion.

F	C
Conventional kinematics ($\beta = 0$)	Counter-propagating beams ($\beta > 0$)
Scattered electron momentum	
$p_{e'} = \frac{p_e - E^*}{1 + 2\frac{p_e}{M} \sin^2 \frac{\theta}{2}}$	$p_{e'} = \frac{p_e - \delta E^*}{1 + 2\frac{p_e - p_A}{M} \delta \sin^2 \frac{\theta}{2}}$
Momentum transfer	
$q^2 = \frac{4p_e^2 \sin^2 \frac{\theta}{2}}{1 + 2\frac{p_e}{M} \sin^2 \frac{\theta}{2}}$	$q^2 = \frac{4p_e^2 \sin^2 \frac{\theta}{2}}{1 + 2\delta\frac{p_e - p_A}{M} \sin^2 \frac{\theta}{2}}$
Resolution (momentum dependence)	
$\Delta E^* \approx - \left(1 + 2\frac{p_e}{M} \sin^2 \frac{\theta}{2} \right) \Delta p_{e'}$	$\Delta E^* \approx - \left(\frac{1}{\delta} + 2\frac{p_e - p_A}{M} \sin^2 \frac{\theta}{2} \right) \Delta p_{e'}$
Resolution (angular dependence)	
$\Delta E^* \approx - \frac{p_e p_{e'}}{M} \sin \theta \Delta \theta$	$\Delta E^* \approx - \frac{(p_e - p_A) p_{e'}}{M} \sin \theta \Delta \theta$

Table 3: Comparison of colliding beam and conventional fixed-target kinematics. Calculations were performed assuming counter-propagating beams of 0.74 GeV/nucleon ^{50}Co and 0.5 GeV electrons. In fixed-target kinematics this is equivalent to a 1.642 GeV electron beam. Here, θ and $p_{e'}$ are the scattering angle and the scattered-electron momentum. The quantities $\frac{\partial E^*}{\partial \theta} \Delta \theta$ and $\frac{\partial E^*}{\partial p} \Delta p$ show the sensitivity of the excitation energy determination to the uncertainties in the scattering angle and in the scattered-electron momentum ($\Delta \theta = 1$ mrad and $\frac{\Delta p}{p} = 10^{-4}$).

q GeV/c	Kinematics C				Kinematics F			
	θ deg.	$p_{e'}$ GeV/c	$\frac{\partial E^*}{\partial \theta} \Delta \theta$ MeV	$\frac{\partial E^*}{\partial p} \Delta p$ MeV	θ deg.	$p_{e'}$ GeV/c	$\frac{\partial E^*}{\partial \theta} \Delta \theta$ MeV	$\frac{\partial E^*}{\partial p} \Delta p$ MeV
0.1	11.4	0.504	0.15	-0.16	3.5	1.642	-0.004	-0.16
0.2	22.7	0.518	0.30	-0.16	7.0	1.642	-0.007	-0.16
0.3	33.5	0.540	0.44	-0.16	10.5	1.642	-0.010	-0.16
0.4	43.9	0.572	0.59	-0.16	14.0	1.642	-0.014	-0.16
0.5	53.7	0.613	0.73	-0.16	17.5	1.642	-0.017	-0.16
0.6	62.8	0.662	0.87	-0.16	21.1	1.642	-0.021	-0.16

406

The strong variation of the scattered electron energy with angle results in

times larger than for counter-propagating beams.

407 an extreme sensitivity to the uncertainty in the polar angle determination. It is
 408 shown in Table 3, to be a factor of 40 larger for a ^{50}Co beam colliding with 0.5
 409 GeV electrons than in a fixed-target kinematics with equivalent electron energy
 410 (1.64 GeV). This factor increases to about 400 for beams of ^{132}Sn . The sensi-
 411 tivity to the uncertainty in absolute value of the scattered electron momentum
 412 is about the same in both systems.

413 The colliding beam kinematics, however, allows identifying the residual nucle-
 414 us in coincidence with the scattered electron. Reaction products, including
 415 nucleons and γ -rays, can be detected using specific sub-detector systems. In
 416 addition, the detector setup allows to identify A and Z for the fragments, as
 417 shown in section 6. Their momenta and energies can be determined and the
 418 reaction kinematics can be reconstructed. This, in turn, allows a unique classi-
 419 fication of the observed reaction. In addition, the use of the coincidence method
 420 results in a strong reduction of the unavoidable radiative background seen in
 421 conventional inclusive electron-scattering experiments.

422 4. Conceptual design of the electron-nucleus collider at NESR

423 The conceptual layout of the collider facility is presented in Fig. 2. It consists
 424 of two rings with different circumferences: the electron ring EAR with electron
 425 energies between 0.2 and 0.5 GeV, and the ion ring NESR, which will operate
 426 at a set of discrete energies between 0.2 GeV/nucleon up to 0.74 GeV/nucleon.
 427 The electron ring is filled with electrons from a pulsed linac. NESR is supplied
 428 with pre-cooled fragment beams from a dedicated Collector Ring (CR) which is
 429 capable of cooling the secondary beams stochastically to primary beam quality
 430 within approximately 1.5 s.

431 The electron ring is placed outside the main ion ring, so that a bypass beam
 432 line connects NESR with EAR and provides sufficient space for the electron spec-
 433 trometer and a recoil detector system. The ion and electron beam trajectories
 434 intersect at an interaction point (IP) around which the electron spectrometer
 435 as well as auxiliary detectors for measuring the reaction products are placed.
 436 The IP is also viewed along the straight section through bore holes in the dipole
 437 magnets, that allow for installing the luminosity monitor described in section 7.

438 4.1. General considerations

439 The main parameters for the two rings and a hypothetical neutron-rich ura-
 440 nium isotope, with $A/Z = 2.7$ and kinetic energy 0.74 GeV/nucleon (this energy
 441 corresponds to a velocity $\beta_A = 0.8303$ and a rigidity of 12.5 Tm), are listed in
 442 Table 4. The ratio between the revolution frequencies of electrons and ions n
 443 should be an integer. Beam-beam effects require that n is as small as possible.
 444 An acceptable value for the highest ion energy 0.74 GeV/nucleon is $n = 5$. Then
 445 a discrete set of other possible energies is: 0.3587 GeV/nucleon ($n = 6$), 0.2254
 446 GeV/nucleon ($n = 7$). If the circumference of the NESR orbit is taken to be
 447 222.916 m, then 53.693 m are required for the circumference of the EAR. For
 448 the proposed beam-optics both beams are flat at IP, with horizontal beam sizes

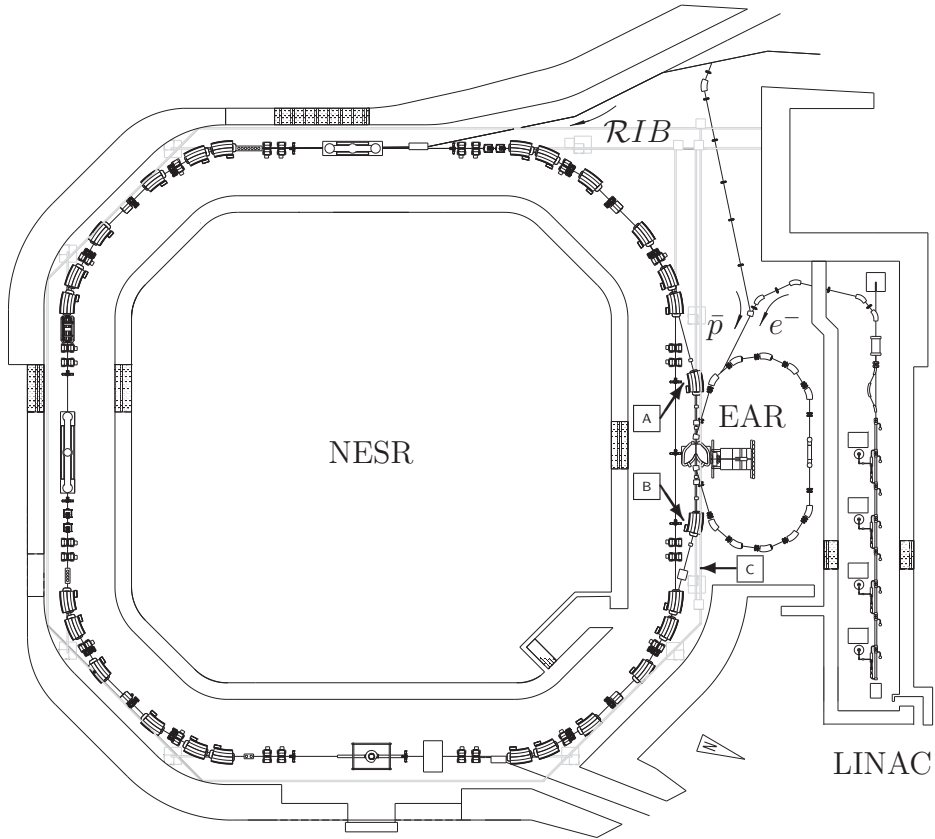


Figure 2: Schematic layout of the New Experimental Storage Ring (NESR, circumference 222.9 m) for Rare Isotope Beams (RIB) and the Electron Antiproton Ring (EAR, circumference 53.7 m). Electrons with energies ranging from 125 MeV to 500 MeV will be provided by an electron linac and stored in the EAR. Antiprotons can be directed from a dedicated collector ring (not shown) into the EAR via a separate beam line. The intersection between EAR and NESR is equipped with an electron spectrometer setup which will be discussed in the following. The free space opposing the spectrometer can be equipped with experiment specific detectors. The arrow at [C] points to the place where an optical bench is situated, from which the intersection can be viewed through a 10 cm hole in the dipole magnet. A luminosity monitor, based on bremsstrahlung detection, discussed in section 7, and LASER installations for atomic physics experiments can be installed here. For a detailed discussion of the bypass section ([A]-[B]) see text.

449 of $\sigma_x = 210 \mu\text{m}$ and $220 \mu\text{m}$ and vertical beam sizes of $\sigma_y = 85 \mu\text{m}$ and $87 \mu\text{m}$
 450 for the EAR and NESR, respectively.

451 The momentum spread of the electron beam at the interaction zone restricts
 452 the achievable resolution for the transferred energy and momentum in electron
 453 scattering experiments considerably. The momentum spread of the beam is
 454 shown in Fig. 3 as function of the electron energy. It depends mainly on two

Table 4: General parameters of the electron-nucleus collider assuming a 0.74 GeV/nucleon uranium beam.

	units	EAR	NESR
Circumference	m	53.693	222.916
Bending Radius, R	m	1.75	8.125
Maximum energy	GeV, GeV/nucleon	0.5	0.74
Revolution frequency, F_e, F_A	MHz	5.585	1.117
Number of bunches, n_e, n_A		8	40
Bunch population, N_e, N_A	particles	$5 \cdot 10^{10}$	$0.86 \cdot 10^7$
Bunch length, σ_s	cm	4	15
Beam size at IP, $\sigma_{x,y}$	μm	210; 85	220; 87
Momentum spread, $\frac{\Delta p}{p}$	%	$3.6 \cdot 10^{-2}$	$4 \cdot 10^{-2}$
Beam divergence at IP, $\sigma_{x0,y0}$	mrad	0.22; 0.58	0.22; 0.58
Beta function at IP, $\beta_{x,y}$	cm	100; 15	100; 15
Laslett tune shift, $\Delta\nu$			0.08
Luminosity	$\text{cm}^{-2}\text{s}^{-1}$	10^{28}	

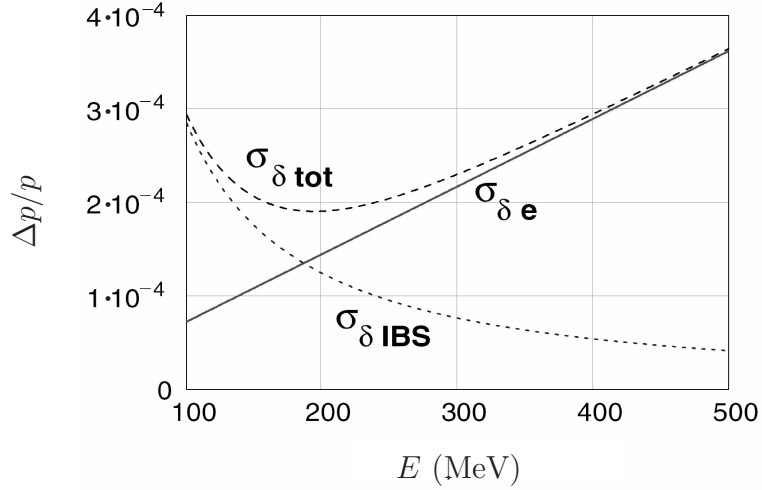


Figure 3: Dependence of the electron-beam momentum spread $\frac{\Delta p}{p}$ on the electron-beam energy E . Here $\sigma_{\delta e}$ denotes the contribution to the momentum spread from statistical fluctuations due to synchrotron radiation, $\sigma_{\delta IBS}$ is caused by intra-beam scattering, and $\sigma_{\delta tot}$ denotes the total momentum spread.

455 effects: (i) intra-beam scattering (IBS) and (ii) statistical fluctuations due to
456 synchrotron radiation. IBS is an effect where collisions between particles bring
457 charged particles closer to thermal equilibrium in a bunch and generally causes
458 the beam size and the beam-energy spread to grow. This effect limits as well

Table 5: Luminosities L for 0.74 GeV/nucleon ion beams for several reference nuclei. Here, $T_{1/2}$ is the half-life of the nucleus at rest, τ its total life time, and N the total number of ions stored in the NESR storage ring.

Element	$T_{1/2}$, s	τ , s	N	L , $\text{cm}^{-2}\text{s}^{-1}$
^{11}Be	13.8	35.6	$2.1 \cdot 10^{10}$	$2.4 \cdot 10^{29}$
^{35}Ar	1.75	4.5	$8.5 \cdot 10^7$	$1.7 \cdot 10^{27}$
^{55}Ni	0.21	0.5	$2.0 \cdot 10^7$	$4.0 \cdot 10^{27}$
^{71}Ni	2.56	6.5	$4.3 \cdot 10^7$	$1.1 \cdot 10^{27}$
^{93}Kr	1.29	3.3	$6.6 \cdot 10^6$	$1.8 \cdot 10^{28}$
^{132}Sn	39.7	68.2	$1.2 \cdot 10^9$	$1.9 \cdot 10^{28}$
^{133}Sn	1.4	3.5	$7.3 \cdot 10^6$	$2.0 \cdot 10^{26}$
^{224}Fr	199	59.2	$3.2 \cdot 10^8$	$8.6 \cdot 10^{27}$
^{238}U	10^{17}	60	$6.0 \cdot 10^{10}$	$1.0 \cdot 10^{28}$

459 luminosity and lifetime. IBS gives a relationship between the size of the beam
460 and the number of particles it contains, and leads therefore to a limit for the
461 maximally achievable luminosity [69]. The emission of quanta in synchrotron
462 radiation is a Poisson process. This process leads to a decrease of the mean
463 energy of electrons due to radiation losses [70] and to an increase of the energy
464 spread in a bunch caused by statistical fluctuations.

465 Assuming transverse Gaussian distributions for the bunches, the luminosity
466 (L) in a collider is given by

$$L = F_e n_e \frac{N_e N_A}{4\pi\sigma_x\sigma_y}. \quad (7)$$

467 Thus, options for a substantial increase of luminosity include the reduction of
468 beam sizes at the interaction zone $\sigma_{x,y}$ and/or an increase of bunch population
469 (N_e , N_A), number of colliding bunches n_e (or n_A) and revolution frequencies
470 F_e (or F_A). However, the decrease of $\sigma_{x,y}$ or an increase of N_e , N_A unavoid-
471 ably also increases the intra-beam scattering, and beam-beam forces which lead
472 to collective (coherent) and incoherent beam-beam instabilities and thus to a
473 reduction of the luminosity. In the case of a very intense ion beam, the space-
474 charge effect results in an upper limit of the luminosity $L_{\text{sp.ch.}}$, which does not
475 depend on the number of ions in the bunches, is given by

$$L_{\text{sp.ch.}} = F_e n_e \frac{A}{Z^2} \frac{N_e \Delta\nu \gamma^3 \beta^2}{4\pi r_p \sqrt{\beta_x \beta_y}} \frac{2\sqrt{2\pi}\sigma_s}{R}, \quad (8)$$

476 where r_p is the classical proton radius, β and γ are the Lorentz factors. For the
477 other variables, see definitions in Table 4.

478 Apart from the above-mentioned limitations leading to a flat plateau of
479 maximally achievable luminosities, as can be seen in Fig. 4, the production and
480 preparation of secondary beams strongly influence the total number of unsta-
481 ble isotopes available for experimental studies at the outer part of the nuclear

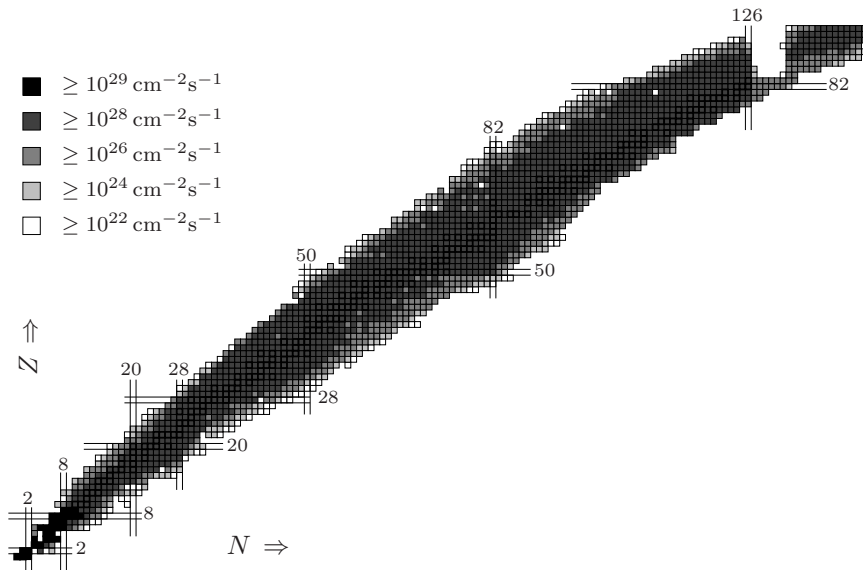


Figure 4: Maximum achievable luminosities for individual 0.74 GeV/nucleon ion beams at the interaction zone. Shown is the luminosity as function of the charge Z and the neutron number N according to the grey scale code shown in the upper left corner. Stable isotopes and magic numbers are labeled and distinguished by extended lines. A central plateau is visible, which drops rapidly at the edges where the most unstable and short-lived nuclei that can be studied with ELISE are situated. These luminosities comfortably suit to the requirements given in Table 1 on page 12 for a wide range of isotopes far from the valley of beta-stability. The simulation calculation takes fully into account, (i) production and separation process, (ii) transport through separator and beam lines, (iii) cooling and storage in the storage rings, and (iv) decay losses. For details, see text.

482 landscape. Table 5 shows a selection of the the numerical results as depicted
 483 also in Fig. 4.

484 (i) We start with an optimized production scheme, taking the maximum for
 485 the yield [71] and including the acceptance of the Super FRagment Separator
 486 (Super-FRS) [72] for fission and fragmentation reactions, whilst the available
 487 primary beams are varied. The mass-resolution [73] in the separator depends
 488 on the choice of the niobium degraders that are used in order to distinguish
 489 differently charged ions using the $B\rho-\Delta E-B\rho$ method in the Super-FRS via
 490 the expression:

$$(x|\delta_m) = -\frac{D_i}{M_i} \cdot \frac{d}{r_i} \cdot \frac{L_m}{\lambda}, \quad (9)$$

491 where $(x|\delta_m)$ is the variation of the position with ion mass, e.g. on a slit
 492 system, D_i denotes the dispersion, M_i the magnification and d/r_i the normalized
 493 degrader thickness for a given stage of the separator. The quantity L_m/λ relates
 494 to the stopping power of the degrader material. The degrader thickness is then

495 optimized with respect to the losses expected from electromagnetic dissociation
 496 and nuclear reactions in the degrader material with an iterative procedure. The
 497 total electromagnetic dissociation cross section is approximated using a model
 498 where particular nuclei disintegrate via excitation to their giant dipole resonance
 499 (GDR). The GDR resonance energy is taken from a parameterization [28] that
 500 is based on experimental data. To calculate the cross section, we use 120% of
 501 the Thomas-Reiche-Kuhn sum rule and the computed number of virtual E1-
 502 photons. For that, the minimal impact parameter b_{min} , which is also used
 503 to estimate the nuclear cross section, is obtained from the systematics [74] by
 504 Benesh, Cook and Vary.

505 (ii) Subsequently, the transport and injection efficiency into the CR-ring
 506 is taken into account by using a parameterization that is extracted from vari-
 507 ous ion-optical simulation calculations [75] and depends on production process,
 508 mass, and charge of the secondary beam particle.

509 (iii) Finally, nuclear and atomic life times are taken into account in order to
 510 provide a reliable prediction of the number of cooled ions in the NESR storage
 511 ring. Cooling and preparation of ions in the NESR is designed to take place in
 512 at most two synchrotron (SIS100/300) cycle times, i.e. within 1.3 or 2.6 seconds.
 513 The nuclear losses have been computed taking the information available from
 514 the Lund/LBNL [76] database. The appropriate time dilation is taken into
 515 account. For longer-lived ions (10 s to minutes) it is possible to further increase
 516 intensity by stacking, i.e. injecting several cycles from the synchrotron into the
 517 storage ring in case the production yield is limiting the number of stored ions.
 518 Different stacking methods and associated parameters are still being studied
 519 [77] and have not yet been included into the simulation calculation.

520 (iv) Atomic processes in the storage ring, when ions interact with electrons
 521 of the electron cooler and the rest gas, are another important source of losses to
 522 be taken into account. Electron capture from the electron cooler in particular
 523 radiative recombination for fully stripped ions and the recombination processes
 524 (Non Resonant electron Capture, NRC and Resonant Electron Capture, REC)
 525 due to interaction with rest gas electrons can be calculated [78, 79, 80] with
 526 good precision. Losses also occur when the charge state and, therefor, the
 527 magnetic rigidity of the ions change so that they fall outside of the acceptance
 528 of recirculating ions. The total life time τ in the ring is given by

$$\frac{1}{\tau} = \frac{1}{\tau_{\text{nuclear}}} + \frac{1}{\tau_{\text{atomic}}} \quad , \quad (10)$$

529 where τ_{nuclear} is the nuclear lifetime, see (iii), and τ_{atomic} is the atomic lifetime.
 530 Numerical values for τ for selected isotopes can be found in Table 5 on page 17.

531 4.2. Physics performance: elastic scattering

532 As an example what can be achieved with ELISE, the results of two simula-
 533 tions are shown in Fig. 5 for two the stable nuclei, ^{12}C and ^{208}Pb , which have
 534 very large differences in their charge-density distributions.

535 The Fourier-Bessel parameters with which the "true" cross sections are cal-
 536 culated are taken from [31]. These cross sections were obtained with the code

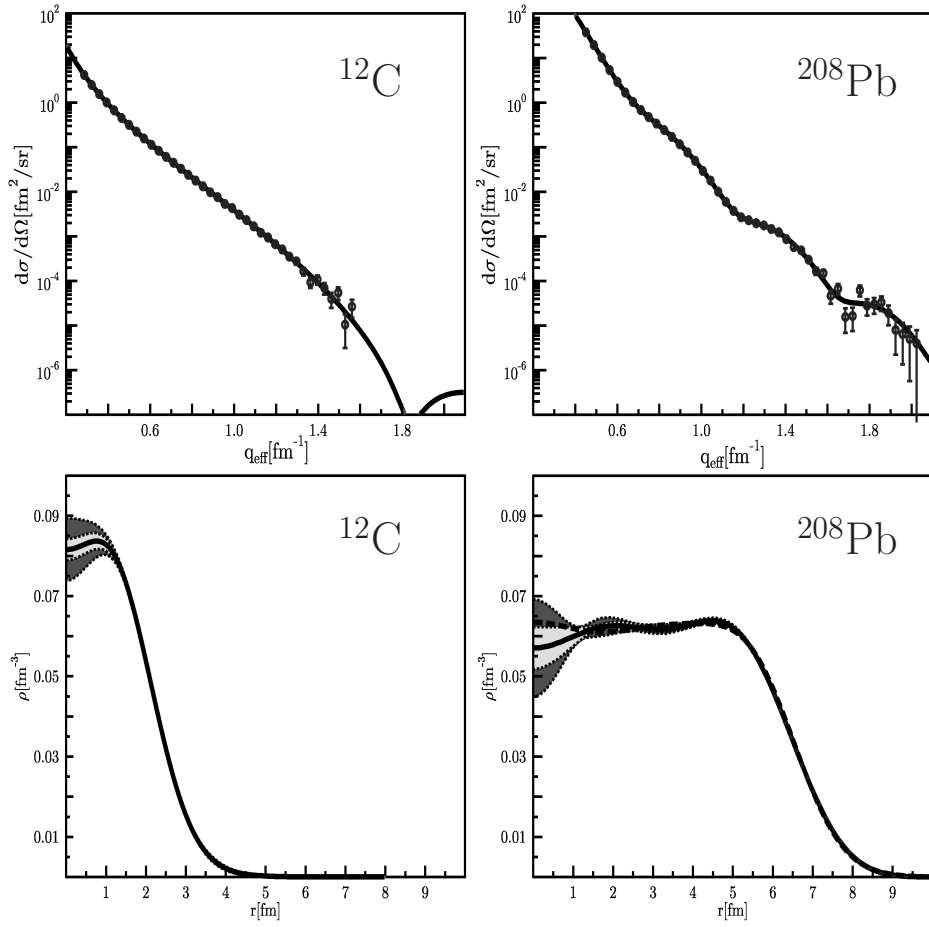


Figure 5: Results of the simulations for two hypothetical measurements to obtain the charge-density distributions of ^{12}C and ^{208}Pb with a luminosity of $10^{28} \text{ cm}^{-2}\text{s}^{-1}$, a solid angle of 100 msr and a running time of 4 weeks. The curves in the upper panels present the "true" cross sections obtained from the known parameters. The data are simulated data points generated around the curve with their statistical errors. In the lower panels, the corresponding charge-density distributions (solid curve) obtained from the simulated data are shown with the corresponding error bands. The dashed curve in the lower-right panel shows the initial charge distribution for reference. For the carbon case both curves are indistinguishable. See text for further details.

537 MEFICAL [81] that uses a distorted-wave approach. They were subsequently
 538 randomized with the expected statistics for a 4 week run, and with a luminosity
 539 of $10^{28} \text{ cm}^{-2}\text{s}^{-1}$ assuming a solid angle of 100 msr to obtain the "experimental"
 540 data points shown in the figure. These points were then fitted using the code
 541 MEFIT [81]. The output of this code is the parameters of the charge-density
 542 distribution. In the fit, an exponential fall-off as upper limit for the cross section

543 outside the measured region was assumed.

544 The inner-shaded areas in the lower panels of the figure result from the "sta-
545 tistical" uncertainties of the measurement and the outer-shaded areas represent
546 the fact that one does not measure to infinite momentum transfers and thus
547 creates an error in the Fourier transform. The results of the fit (solid curve)
548 can be compared directly with the original distributions used to generate the
549 "data" (dashed curve). As can be seen in the figure, with a modest solid angle
550 of 100 msr, a running time of 4 weeks, and a luminosity of $10^{28} \text{ cm}^{-2}\text{s}^{-1}$, one
551 can already have results for charge-density distributions which can be compared
552 to results of theoretical models.

553 The sensitivity of the simulated experiment indicated by the given error
554 band should be compared to the theoretical predictions presented by Grasso et
555 al. [14], where e.g. a central depletion by 50% in the nucleus ^{34}Si is expected
556 due to its particular nuclear structure. The shown result would clearly allow to
557 confirm or abandon such a forecast.

558 *4.3. Bypass design*

559 The bypass region is shown in detail in Fig. 6. The arrangement of magnetic
560 elements is symmetric with respect to the interaction point. The first two dipoles
561 are placed symmetrically around the IP at a distance of 1.9 m, leaving enough
562 space for installing the electron spectrometer. Both are used to separate the
563 orbits of ions and electrons. As electrons and ions have opposite electric charges
564 and move in opposite directions both orbits are deflected to the left by the
565 separation dipoles. The magnetic field in the dipoles has to be adapted to the
566 energy of the electron beam in order to bend the electrons to a fixed angle
567 (16.5°) before entering the EAR. The bending angle for ions depends on the
568 ion-beam energy and varies between 0.8° and 3.0° . Just in front of the bending
569 magnets two pick-up systems are installed in order to measure the beams orbits.
570 Two additional dipoles are placed exclusively in the ion path, allowing for an
571 orbit correction depending on the particular electron and ion beam energies.
572 The following quadrupole doublets combine the beta-functions in the IP and
573 in the ring and focus into the adjacent large dipole stages. These subsequently
574 bend the ions by 15° , and eventually, the ion trajectory unites with the original
575 ion orbit in the NESR.

576 The bypass is exclusively used in the collider mode. In this case, as shown
577 in Fig. 12 on page 30, the two last NESR magnets of NESRs dipole triplets in
578 the arcs are switched off in order to direct the ions into the bypass region. The
579 straight sections connecting the NESR with the EAR provide about 7 meters of
580 free space. The section before the interaction zone at position **B** in Fig. 6 will
581 be used to install an additional RF-cavity exclusively used for the preparation
582 of bunches for the collider mode. The section following position **A** is part of
583 the in-ring spectrometer setup described in section 6 on page 29.

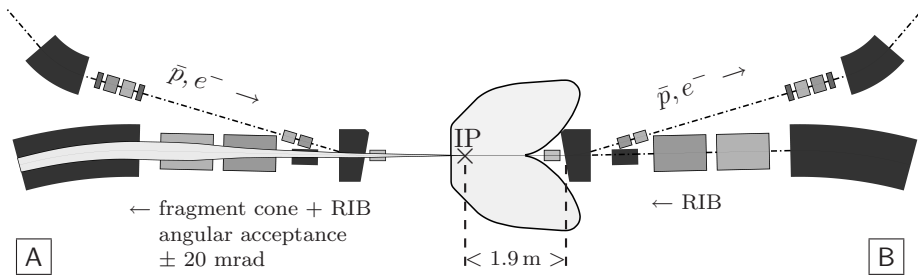


Figure 6: Interaction zone with the interaction point IP in the bypass section of the NESR. The labels **A** and **B** correspond to those in Fig. 2 on page 15. The bore holes along the beam axis for the viewports in the large dipole stages have been omitted in the drawing. Fragments emerging from the interaction zone are transported to a 7 m long straight section after the dipole (at position **A**) providing a sufficiently long time-of-flight path for the in-ring detectors system (see section 6).

584 5. Electron spectrometer

585 5.1. Challenges to be met

586 The technological challenge for the eA collider results from the simultaneous
 587 requirement for large acceptance and high momentum resolution. In addition,
 588 the spectrometer should allow for tracking the position of the reaction vertex
 589 inside the reaction zone. Existing magnetic spectrometers only partially fulfill
 590 these specifications. For instance, the electron spectrometers at the universities
 591 of Darmstadt [82] and Mainz [83] and at the research center TJNAF [84] meet
 592 the requirements with respect to momentum and angular resolution. They
 593 can handle reaction zones extending up to 10 cm, but only have a moderate
 594 acceptance of < 40 msr.

595 Existing toroidal and solenoidal spectrometers, e.g. HADES [85], BLAST [86]
 596 and BELLE [87], that cover 2π in azimuthal angle ϕ , provide the required ac-
 597 ceptance but only modest resolution. The main limitations for the resolution
 598 arise from energy and angular straggling of electrons in the tracking detectors.
 599 A large-acceptance spectrometer has advantages, but further research and devel-
 600 opment are needed for a suitable design, which can satisfy both experimental
 601 requirements as discussed above. Due to the fact that differential cross sections
 602 for electron scattering decrease rapidly with the angle of the scattered electron,
 603 an ideal electron spectrometer should cover 2π in azimuthal angle but needs
 604 to provide a moderate acceptance in scattering angle of about $\theta = 10^\circ - 20^\circ$
 605 only. The considerations have shown that magnetic dipole-based spectrometers
 606 designed for the collider with an acceptance up to about 100 msr can be built
 607 at a reasonable cost [88].

608 5.2. Large-angle dipole spectrometer

609 5.2.1. Spectrometer with large azimuthal acceptance

610 The restricted luminosity of the collider can be partially compensated by a
 611 large acceptance of the electron spectrometer. We consider first a spectrom-

612 eter with an extraordinarily large azimuthal acceptance, being compared to
 613 typical magnetic spectrometer installations. A spectrometer consisting of two
 614 quadrupoles and one dipole (QQD type) is a promising candidate for this pur-
 615 pose. The layout for such a spectrometer is shown in Fig. 7. The first quadrupole
 616 magnet with large aperture is located as close as possible to the IP.

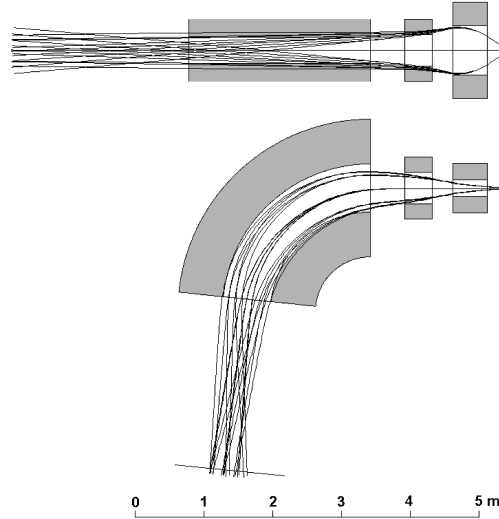


Figure 7: Side view (top) and top view (bottom) of the QQD-spectrometer with large azimuthal acceptance.

617 The rectangular aperture of the first quadrupole magnet is 72 cm in vertical
 618 and 24 cm in horizontal direction. The field gradient is 8.1 T/m. Because
 619 of the very high current density ($\approx 70 \text{ A/mm}^2$) reached, the coils have to be
 620 super-conducting. A very large acceptance in vertical angles $\approx \pm 34^\circ$ is achieved
 621 due to the strong vertical focusing force of the quadrupole. However, the first
 622 quadrupole magnet defocuses the horizontal motion. In order to compensate
 623 this effect, a second quadrupole magnet focusing horizontally and defocusing
 624 vertically is installed. This quadrupole magnet is a normal-conducting type
 625 with a field gradient of about 1.7 T/m. The dipole magnet placed downstream
 626 from the two quadrupole magnets analyzes the scattered electron momentum.
 627 For an arbitrarily chosen bending angle of the dipole magnet, the electron rays
 628 can be focused both horizontally and vertically at the focal plane by tuning the
 629 strengths of the quadrupole magnets.

630 The result of a ray-tracing calculation is shown in Fig. 7: 27 rays with 3
 631 magnetic rigidities (1.9, 2.0, and 2.1 Tm), for 3 horizontal angles ($+4^\circ$, 0° , and
 632 -4°) and 3 vertical angles ($+34^\circ$, 0° , and -34°) are shown. The acceptance
 633 exceeds 1200 mrad for the central momentum, but it is smaller at both edges
 634 of the momentum range. The horizontal angular acceptance is about 200 mrad.

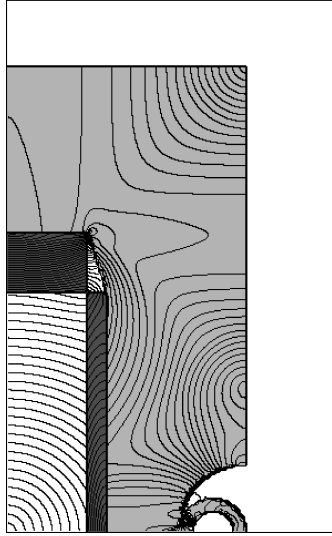


Figure 8: Three-dimensional magnetic field calculation for the first super-conducting Panofsky quadrupole of the QD-spectrometer with large azimuthal acceptance. Contours of the field strength are shown in 0.1 Tesla steps. The quality of the quadrupole field is demonstrated by their equidistant and concentric appearance.

635 The spectrometer, as shown in Fig. 7, is optimized for measurements around a
 636 scattering angle of 90° , but can also be rotated around the IP to cover smaller
 637 angles. In order to allow measurements at smaller scattering angles, the first
 638 quadrupole magnet is made as slim as possible. For these requirements, a super-
 639 conducting Panofsky magnet, employing current sheets bound by iron, rather
 640 than shaped pole faces to establish the field, is the most suitable selection. A
 641 quarter of the first quadrupole magnet is shown in Fig. 8. The trimming of
 642 the side yoke is shown, which provides space for the beam pipe when QD
 643 spectrometer is set at the minimal scattering angle of 50° . The most forward
 644 angle achievable with the QD spectrometer depends on a compact magnetic
 645 shield. In the considered design, two cylindrical layers of magnetic shield cover
 646 the vacuum pipe of the colliding beams. The outer and inner radii of the shield
 647 are assumed to be 40 mm and 20 mm, respectively. The outer and inner shell
 648 thicknesses are then 13 mm and 5 mm, respectively. The shield suppresses
 649 the penetration of magnetic field through the side yoke of the magnet. A two-
 650 dimensional calculation shows that the detrimental magnetic field along the
 651 beam line is most serious at the front face of the quadrupole magnet where the
 652 conductor is not shielded by the yoke of the magnet in contrast to the side face.
 653 Without magnetic shield, the magnetic flux density at the nearest position to
 654 the pipe was calculated to be about 0.4 T. With the double-layered cylindrical
 655 shield, the field strength could be reduced to a safe value of about 0.003 T.

656 The performance of the spectrometer can be summarized as follows:

- 657 • The spectrometer provides an extraordinarily large vertical angle accep-
658 tance of 1200 mrad.
 - 659 • The acceptance in horizontal angle is about 200 mrad.
 - 660 • The spectrometer can be used for measurements in a range of scattering
661 angles from about 50° to more than 100° .
- 662 Selected properties of the magnetic elements are given in Table 6.

Table 6: Some properties of the elements for the QQD spectrometer with large azimuthal acceptance.

First quadrupole magnet			
horizontal aperture	24 cm	vertical aperture	72 cm
yoke width	72 cm	yoke height	140 cm
length	50 cm	field gradient	8.1 T/m
Second quadrupole magnet			
bore diameter	46 cm	field gradient	1.7 T/m
length	40 cm		
Dipole magnet			
gap	38 cm	bending angle	84°
mean orbit radius	180 cm	magnetic field	1.0 T

663 *5.2.2. Spectrometer with a large range of scattering angles.*

664 The second, more versatile system under consideration is an electron spec-
665 trometer composed of a deflection magnet (DM) where two vertical dipole mag-
666 nets (VM) can be placed symmetrically on both sides of the DM. The spectrom-
667 eter is schematically shown in Fig. 9 (only one VM is shown in this figure). The
668 DM magnet can be seen as a pair of dipoles with an opposite magnetic field
669 that are coupled together. The DM acceptance in vertical angle is ± 150 mrad.
670 The specific shape of DM ensures a deflection of the scattered electron in the
671 horizontal plane towards $\approx 90^\circ - \theta_{e'}$ i.e. perpendicular to the beam axis, for
672 scattering angles $\theta_{e'}$ ranging from about 10° to 60° . The inner regions can be
673 kept field free by appropriate shielding to avoid interference with the circulating
674 beams. Initially the pre-deflection system (DM) will be followed by the vertical
675 dipole spectrometer (VM) at the side of the DM facing inside the EAR. Elec-
676 trons that are elastically scattered to the same polar angle but with different
677 azimuthal angles are focused in the focal plane of the spectrometer. Calculated
678 trajectories for 500 MeV electrons elastically scattered off a 0.74 GeV/nucleon,
679 $A = 100$ ion, with transferred momenta of 400 and 600 MeV/c (43.91° and
680 62.82°), and assuming a 2 T field and a gap width of 25 cm for the VM, are
681 shown in Fig. 9. The VMs is equipped with two-dimensional coordinate detector
682 systems and a scintillator array. All detectors and foils are located outside the

683 vacuum chamber of the magnet system in order to minimize distortions from
 684 straggling.

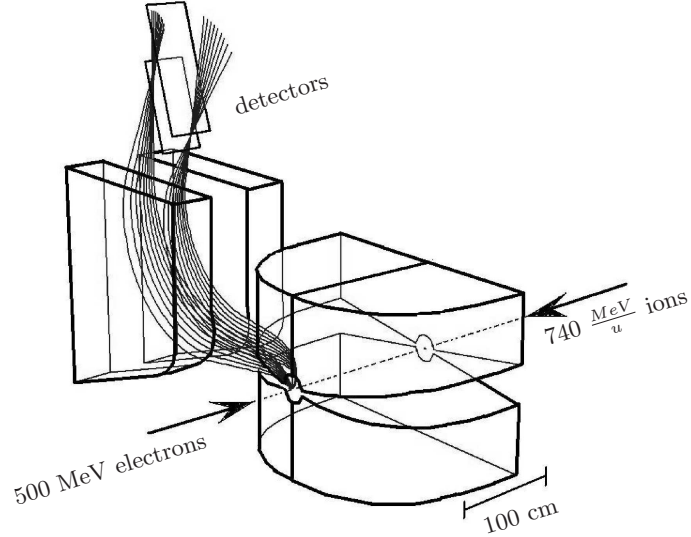


Figure 9: Schematic view of the electron spectrometer consisting of a pre-deflection magnet and a vertical-dipole spectrometer. Trajectories are shown for 500 MeV electrons elastically scattered off 0.74 GeV/nucleon, $A=100$ ions with a momentum transfer of 400 and 600 MeV/c (43.91° and 62.82°), respectively. The focal plane detectors are located outside the vacuum chamber of the magnet system.

685 Full three-dimensional Monte Carlo simulations have been performed to estimate the achievable resolution of the proposed spectrometer. The calculations
 686 were made in two steps. During the first stage, electron trajectories were generated according to the design parameters for momentum spread and beam size
 687 of the electron beam. Aiming at a pure characterization of the spectrometer no cross sections were taken into account in the simulations. The coordinates
 688 of electron-trajectory intersections with the detector planes were subsequently determined. The obtained hit coordinates were distributed randomly according
 689 to the response function of the detectors also including the angular and energy straggling of electrons in the materials. These results were stored as sequential
 690 vectors. The vectors were then used as input for the second stage where a back-tracking routine was applied in order to reconstruct the electron energy $T_{e'}$,
 691 the polar angle $\theta_{e'}$, the azimuthal angle $\varphi_{e'}$ and the position of the interaction point along the z -axis $z(IP)$. For this procedure, the x and y -coordinates of the
 692 interaction point were taken to be zero. Further simulations have shown that the result remains nearly the same if the small transverse extent of the electron
 693 beam (see Table 4) is also taken into account. The result of these studies is that all parameters $T_{e'}$, $\theta_{e'}$, $\varphi_{e'}$ and $z(IP)$ can be reconstructed with satisfying
 694 accuracy from the four parameters of the hits in the two planes of focal-plane detectors. These results are shown in Figs. 10 and 11 for the case of a large
 695 momentum transfer (between 400 MeV/c and 600 MeV/c) where the kinematics
 696
 697
 698
 699
 700
 701
 702
 703
 704
 705

706 for colliding beams is most unfavorable for the reconstruction.

707 Disentangling elastic and inelastic scattering in colliding beam kinematics is
 708 challenging. The angular range of electrons passing through the VM is about
 709 20° for energies between 560 and 660 MeV. The difficulty is to resolve the peaks
 710 separated by only a few hundred keV. This is illustrated in Fig. 10 (left panel)
 711 where the thickness of the displayed line is determined by the energy difference
 712 of electrons scattered elastically or inelastically with $E^* = 1.5, 3.0$ MeV.

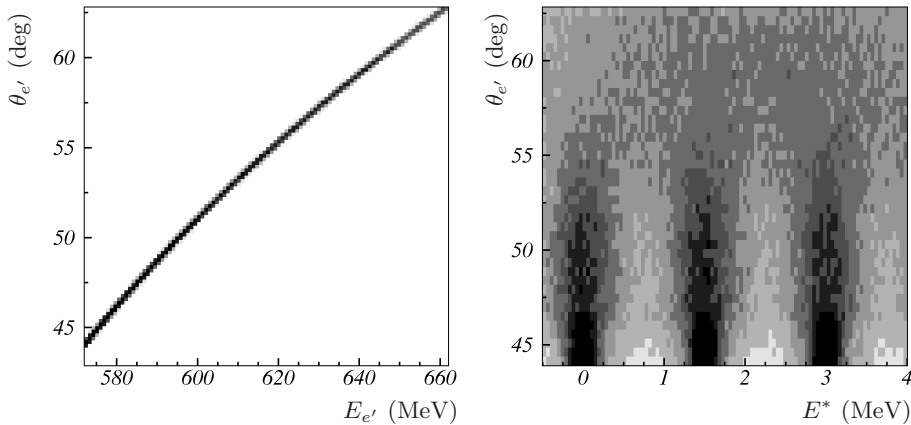


Figure 10: Left panel: Angle versus energy-range covered for a particular setting of the vertical dipole. The curve is obtained in Monte Carlo simulations where 500 MeV electrons scatter off 0.74 GeV/nucleon ions with $A = 100$. Elastic and inelastic ($E^* = 1.5, 3.0$ MeV) scattering events contribute to the observed seemingly unresolved line. The presented range in scattering angles poses the worst case scenario for reconstructing the excitation energy. Right panel: Polar angle dependence of the recovered excitation energy. A back-tracking routine was used for the reconstruction. Distortions due to momentum spread in the beam, finite beam size, straggling effects and position resolutions of the detectors are present.

713 In order to account for the extent of the interaction zone $\sigma_z \approx 5$ cm, the first
 714 two-dimensional coordinate detector is put in the plane where the trajectories
 715 with different azimuthal angles constitute a focus for a given polar angle. The
 716 second detector is placed in parallel to the first detector at a distance of 50 cm.
 717 The spatial resolution of the first detector is assumed to have a Gaussian dis-
 718 tribution with a standard deviation of $50 \mu\text{m}$. This detector and the separation
 719 foil result in an angular straggling of 1 mrad. The resolution of the detector
 720 at the second plane is taken to be $100 \mu\text{m}$. The calculations demonstrate the
 721 possibility to satisfy all experimental requirements with this spectrometer setup
 722 (see also Fig. 11).

723 5.3. Coordinate detectors

724 The use of coordinate detectors based on straw tubes [89] has several ad-
 725 vantages. Cross talk is minimized, since the cells are isolated from each other.
 726 A channel with a broken sense wire can easily be switched off without turning

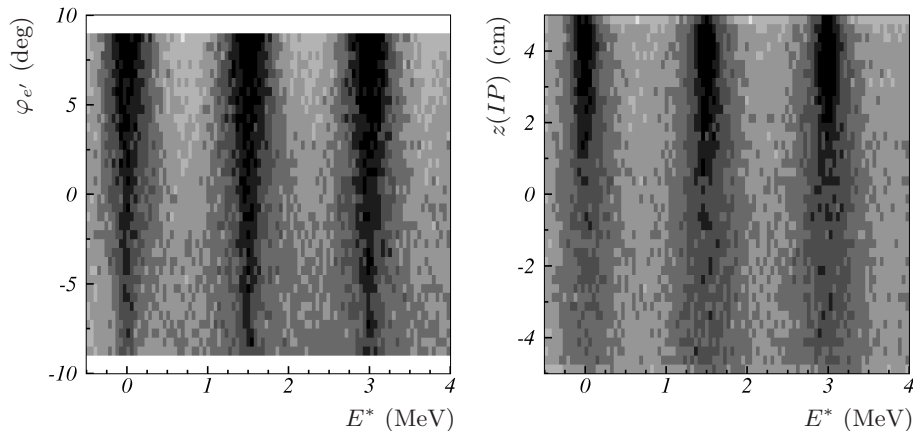


Figure 11: Left panel: Dependence of the reconstructed excitation energy on azimuthal angle. Right panel: Dependence of the reconstructed excitation energy on the position of the interaction point. Parameters of Monte Carlo calculations are the same as in Fig. 10. The picture shows a clear dependence of the achievable E^* resolution on $z(IP)$ position and $\varphi_{e'}$ angle.

727 off all channels. Straw tubes can be designed to withstand pressure and can be
 728 placed in vacuum. The inner pressure not only keeps tubes round and inflexible
 729 but also results in better resolution. The resolution of tracks is almost indepen-
 730 dent of the incident angle and angular corrections are not necessary when the
 731 drift distance is calculated from the drift time, as with usual drift chambers.

732 A prototype straw-tube assembly has been built and put into operation at
 733 the GSI detector laboratory. The prototype design is based on Kapton tubes
 734 covered with a $0.2 \mu\text{m}$ aluminum layer. The tubes are 60 cm in length and
 735 feature a 7.5 mm inner diameter and a total tube-wall thickness of $126 \mu\text{m}$. The
 736 tubes are filled with Ar/CO₂ (80%/20%) at atmospheric pressure and operate
 737 at 1850 V. Detailed studies are currently in progress. Straw tubes filled with
 738 quench gases can be operated at even higher pressure ($\approx 4 \text{ atm}$) and a higher
 739 voltage ($\approx 4 \text{ kV}$); see Ref. [90]. Saturated streams in this mode are initiated
 740 with high efficiency by a single electron with a gain factor of about $5 \cdot 10^5$. The
 741 achieved average spatial resolution of a single tube is $50 \mu\text{m}$ [90].

742 The second position-sensitive detector system under consideration is the use
 743 of vertical drift chambers instead of two layers of x, y -coordinate detectors.
 744 These chambers allow to measure two coordinates of the electron trajectory
 745 crossing the detector plane (x, y) as well as polar and azimuthal angles (θ, ϕ)
 746 of the electron trajectory. Existing chambers provide a resolution close to the
 747 requirements: $\delta x < 100 \mu\text{m}$, $\delta y < 200 \mu\text{m}$, $\delta\theta < 0.3 \text{ mrad}$, $\delta\phi < 1 \text{ mrad}$. Such
 748 a system is routinely used at the MAMI facility [91] and at TU Darmstadt.
 749 Therefore, the already existing designs could be easily adapted to meet the
 750 requirements of the ELISE experiment.

751 It is foreseen to place a plastic scintillation system after the focal plane

752 of the spectrometer. This system consists of 2 modules (plastic scintillation
753 bars, $120 \times 10 \times 4 \text{ cm}^3$) viewed by two photomultiplier tubes from opposite
754 sides coupled with optical pads to the attached light guides. The expected
755 intrinsic time resolution will thus be about 0.1 - 0.2 ns. The bunch timing
756 signals of the NESR will be used for time-of-flight measurements. It is already
757 sufficient to use only one module to detect scattered electrons. The second
758 module is introduced in order to decrease background. The scintillation bars can
759 be manufactured from NE-102 material. Such systems have been successfully
760 used in different experiments to measure electrons with high efficiency and good
761 timing resolution [92].

762 6. In-ring detectors

763 The detection of reaction products is another task required of the ELISE
764 facility. A detector setup placed behind the straight bypass section ($\boxed{\text{A}}-\boxed{\text{B}}$, see
765 Fig. 2) using the first bending dipole as spectrometer magnet for heavy ions is
766 foreseen to be used for this task. The detectors will operate in coincidence with
767 the scattered electrons. They will allow to disentangle different reaction chan-
768 nels in the case of inelastic scattering experiments (e.g. excitation of particle
769 unstable states, quasi-free scattering, electro-fission) and provide means to clean
770 the electron energy spectra from radiative tails originating from other reaction
771 channels.

772 Cooled heavy-ion beams circulate in the NESR with a momentum spread of
773 $\Delta p/p \approx 10^{-4}$ and with an emittance of about $1\pi \text{ mm mrad}$. The design and
774 settings of the magnetic devices are thus governed by the requirement to keep
775 a high-quality ion beam stored. Therefore, the degrees of freedom in building
776 a large acceptance system for the ions emerging from the interaction zone are
777 rather limited. The current design for the bypass shown in Fig. 6 on page 22
778 allows for the detection of fragments in a $\pm 20 \text{ mrad}$ cone which is sufficient
779 for performing the most demanding electro-fission experiments, thanks to the
780 kinematical forward focusing.

781 A possible version of the in-ring detector layout is shown in Fig. 12 together
782 with trajectories calculated for fragments with different magnetic rigidities in
783 steps of 1%.

- 784 • The detector array at position 1 in Fig. 12 allows for the reaction tagging
785 by particle identification for ions (e.g. $(e, e'n)$ via $(e, e'^{A-1}Z)$).
- 786 • The two arrays at positions 2 and 3 provide in addition a fragment track-
787 ing with moderate momentum resolution (by time-of-flight measurements,
788 and with an acceptance $\Delta B\rho/B\rho \approx \pm 7\%$). The obtained resolution is
789 high enough to identify also fission fragments with their large momentum
790 spread.
- 791 • The detector array at position 4 implements the same tasks with even
792 better resolution but further reduced acceptance.

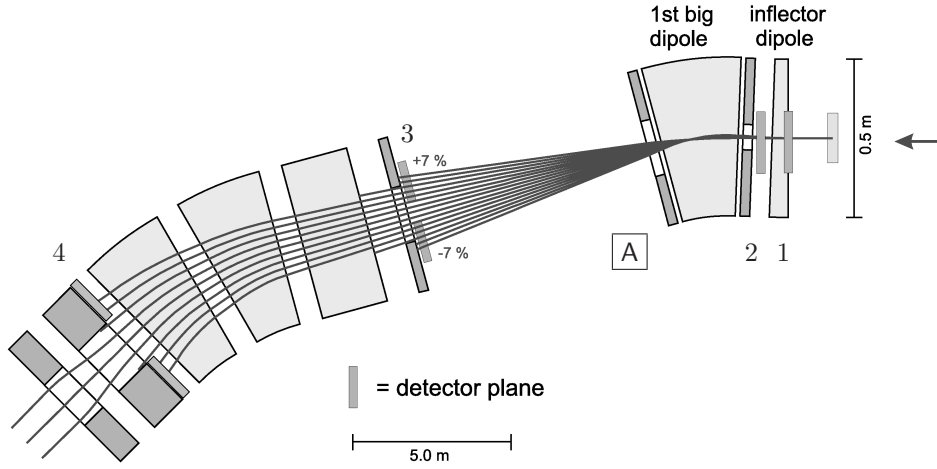


Figure 12: Ion trajectories calculated for different magnetic rigidities through the first bending and adjacent straight section behind the interaction zone. These trajectories are shown for 7 steps of 1% deviation in magnetic rigidity in positive and negative direction from the nominal magnetic rigidity of the circulating beam, respectively. Label **A** refers to the position shown in the previous setup figures 2 and 6.

793 Simulation calculations show, that a resolution of $\Delta p \approx 20 \text{ MeV}/c$, cor-
 794 responding to about 0.5 MeV missing energy resolution, can be achieved for
 795 both longitudinal and transverse momenta in the case of quasi-free scattering
 796 (e,e'p) for a 500 MeV electron beam interacting with 740 MeV/nucleon oxygen
 797 isotopes. In addition, a time-of-flight resolution of 35ps FWHM is needed to
 798 separate fission fragments by mass reliably. First measurements have shown,
 799 that this time resolution can be reached by using quenched scintillator material
 800 viewed with fast photomultipliers.

801 Detectors located near the circulating beam in the first two planes (1 and 2 in
 802 Fig. 12) should be UHV compatible and should be thin enough in order to avoid
 803 distortions caused by multiple scattering inside the detector material. The first
 804 choice is an array of 100 μm thick CVD (chemical vapor deposition) diamond
 805 micro-strip detectors. Alternatively, 100 μm thick silicon detectors would also
 806 meet the requirements, however, they are more sensitive to irradiation. Both
 807 detector types can provide 0.1 mm resolution for the ion hit positions. Compared
 808 to Si-based detectors, a diamond detector has excellent merits in terms of high
 809 radiation resistance, low leakage current, high operation temperature and high
 810 chemical inertia. The expected resolutions for these assemblies are $\Delta p/p \approx$
 811 10^{-3} and 1 mrad for the momentum and angle measurements, respectively, in
 812 accordance with the previously shown example.

813 Since the detectors can only be positioned after the beam preparation dur-
 814 ing setup or cooling phase in the NESR is completed, the detector arrays are
 815 subdivided into two parts, each one mounted on a remotely controlled driving
 816 device. They are designed to be removable in vertical direction and the range

817 is kept adjustable according to the beam emittance. Scattered ions can then be
818 detected starting from a minimum scattering angle of about 1 mrad.

819 A halo around the ion beam stored in the NESR could potentially damage
820 the detectors. Another source of radiation are beam ions leaving the orbit after
821 scattering off the counter-propagating electrons or ions that undergo atomic
822 charge-changing reactions in the rest gas. Calculations have shown that for a
823 luminosity of $10^{29} \text{ cm}^{-2}\text{s}^{-1}$ the count rate, normalized to the detector area, will
824 not exceed $10^4 \text{ cm}^{-2}\text{s}^{-1}$ for detectors placed at a distance of 10 mm from the
825 NESR beam axis. This estimate means that neither the diamond nor the silicon
826 detectors will show any essential damage even after three years of continuous
827 operation.

828 The existing experimental storage ring (ESR) at GSI is equipped with gas de-
829 tectors, scintillators, silicon-strip detector arrays, and diamond detectors. The
830 experience obtained during operation of ESR will be used and existing tech-
831 niques will be extended to satisfy the specific demands of the eA collider.

832 7. Luminosity monitor

833 Elastic electron scattering is always accompanied by the process of brems-
834 strahlung, involving emission of photons. A radiative tail of lower-energy elec-
835 trons appears in the electron energy spectrum, e.g. due to bremsstrahlung, lead-
836 ing to an extension of the electron energy spectrum below the elastic scattering
837 peak [93]. Bremsstrahlung is therefore commonly used to monitor luminos-
838 ity. The angular and energy distributions of the bremsstrahlung are shown in
839 Fig. 13. The narrow angular distribution ($\Delta\theta_\gamma \approx 1/\gamma_e$ rad) allows for diagnostic
840 and adjustment of the electron beam position.

841 The presence of rest gas in NESR, even on a level of $3 \cdot 10^{-11}$ mbar, is a source
842 of $500 N_\gamma/\text{s}$ background bremsstrahlung of photons with energies larger than
843 100 MeV for the electron-beam parameters given in Table 4. As can be seen
844 in Fig. 13 in panel 2, the effect of screening by orbital electrons leads to strong
845 changes in the bremsstrahlung spectrum. This effect allows in principle for a
846 correction for the rest-gas background contribution by precise measurements of
847 the shape of the γ -spectra. Bremsstrahlung intensities of γ -rays with energies
848 larger than 100 MeV are given in Table 7 for several reference nuclei with a
849 kinetic energy of 0.74 GeV/nucleon. In this table, L_B denotes the luminosity
850 where the γ -ray background due to the rest-gas becomes equal to the amount
851 of bremsstrahlung caused by the presence of the ion beam. We neglect the
852 ionization of the residual gas in the vacuum chamber by the circulating electron
853 bunches. The ionization creates positive ions which under certain circumstances
854 become trapped in the potential well of the stored electron beam [94]. The effect
855 is suppressed due to the counter-propagating beam of positive ions moving along
856 the same trajectory.

857 For the luminosity measurement using bremsstrahlung a system capable of
858 detecting high energy photons is needed. The PbWO_4 crystal is distinguished by
859 its fast decay time (6/30 ns at 440/530 nm), a high density (8.28 g/cm^3) and its
860 radiation hardness. Thus, it is an excellent γ -detector also due to its favorable

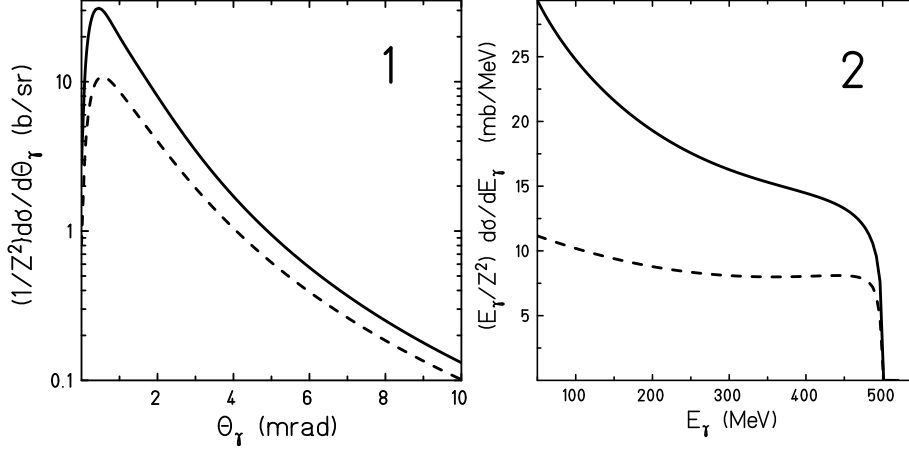


Figure 13: Angular (panel 1) and energy (panel 2) distributions of bremsstrahlung emitted by the electron beam. The distributions are given for scattering off 0.74 GeV/nucleon ions (solid curve) and on rest-gas nuclei (dashed curve). In the latter case, the effect of the screening of the nucleus by atomic electrons is taken into account.

Table 7: Bremsstrahlung intensity for γ -rays with energies higher than 100 MeV (ion beam kinetic energy 0.74 GeV/nucleon). Here, σ_B is the cross section for producing bremsstrahlung at the given conditions, and L_B is the value where the γ -background caused by rest-gas in the storage ring becomes equal to the amount of bremsstrahlung induced by the ion beam.

Ion beam	Luminosity $\text{cm}^{-2} \text{s}^{-1}$	σ_B barn	Yield N_γ 10^3s^{-1}	L_B $\text{cm}^{-2} \text{s}^{-1}$
^{11}Be	$2.4 \cdot 10^{29}$	0.48	115.2	$1.1 \cdot 10^{27}$
^{35}Ar	$1.7 \cdot 10^{27}$	9.7	16.5	$5.3 \cdot 10^{25}$
^{55}Ni	$4.0 \cdot 10^{27}$	23	94.1	$2.2 \cdot 10^{25}$
^{71}Ni	$1.1 \cdot 10^{27}$	23	25.9	$2.2 \cdot 10^{25}$
^{93}Kr	$1.8 \cdot 10^{28}$	38	700	$1.3 \cdot 10^{25}$
^{132}Sn	$1.9 \cdot 10^{28}$	75	1425	$7.0 \cdot 10^{24}$
^{133}Sn	$2.0 \cdot 10^{26}$	75	15.0	$7.0 \cdot 10^{24}$
^{224}Fr	$8.6 \cdot 10^{27}$	227	1953	$2.3 \cdot 10^{24}$
^{238}U	$1.0 \cdot 10^{28}$	254	2539	$2.0 \cdot 10^{24}$

861 optical, physical and chemical properties, accounting for its long- term stability.
862 The radiation length (x_0) of the crystal is less than 1 cm, where x_0 is linked
863 to the total energy loss $E(x)$ by $E(x) = E_0 \exp(-x/x_0)$. A material thickness
864 corresponding to $20x_0$ is sufficient to absorb about 99% of the induced showers.
865 The crystals are characterized by a very small Molière radius (≈ 2 cm) which
866 describes the transverse extension of the showers due to multiple scattering

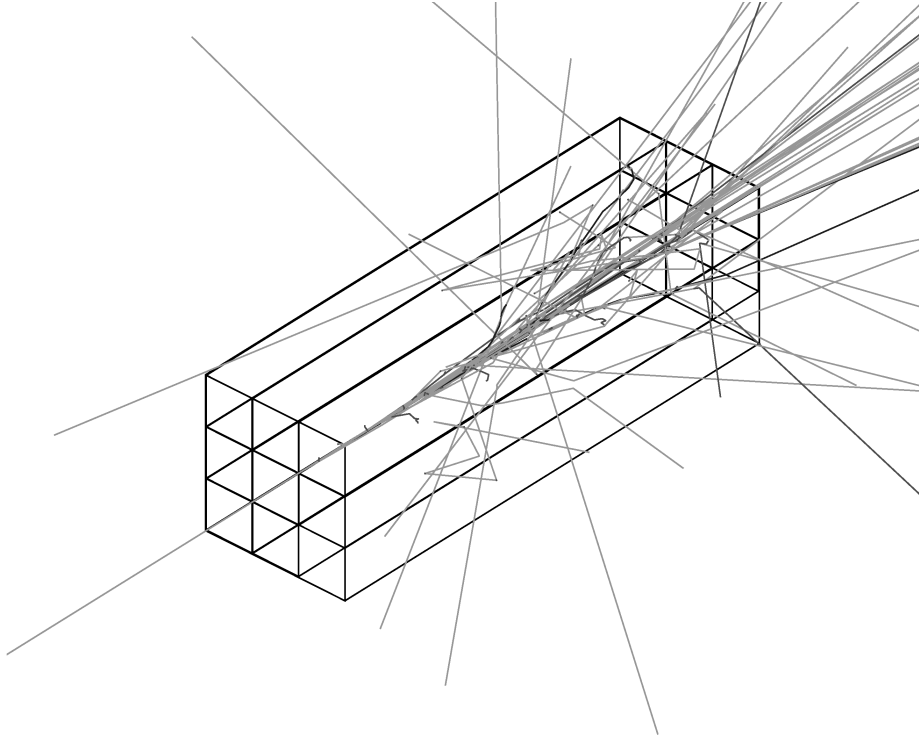


Figure 14: Shower created in a stack of 3×3 PbWO_4 crystals by one 300-MeV-gamma ray (GEANT4 simulation calculation). The geometry used for the calculations is the same as described in the text.

867 of low energy electrons inside the material. More than 99% of the shower is
 868 situated within 3 Moliere radii bounds. The application of these detectors for
 869 γ -spectroscopy from tens of MeV up to several hundred MeV with good energy
 870 ($\sigma_E/E = (1.7/\sqrt{E[\text{GeV}]} + 0.6)\%$) and spatial resolution ($\sigma_{x,y} \leq 5$ mm) is
 871 feasible [95].

872 The luminosity monitor will be built as a 3×3 matrix of PbWO_4 scintillators
 873 ($20 \times 20 \times 200$ mm³), and placed about 8–10 m from the interaction point (see
 874 Fig. 2 on page 15, [C]). The bremsstrahlung beam then illuminates mainly
 875 the central cell of the matrix. The detector array covers the dominant part of
 876 the radiation cone. A simulated shower created by one 300-MeV-gamma ray
 877 is shown in Fig. 14. An Avalanche Photo Diode (APD) readout is currently
 878 foreseen which achieves a suitable energy resolution, if the diode is being cooled
 879 down to a well stabilized ($\Delta T = 0.1^\circ\text{C}$) temperature.

880 8. Data acquisition and handling

881 There are several specific demands on the ELISe data acquisition and online
882 analysis, as the experiment is an integral part of the NESR/EAR accelerator
883 complex. The detection system in the ELISe experiment will be used to monitor
884 the achieved beam quality, and to optimize the beam settings accordingly. A
885 strong coupling to the accelerator control system requires stable operation of
886 the detector systems with their associated slow-control components and online
887 analysis. Furthermore, it is mandatory that these systems can be operated
888 without detailed knowledge about their components by the accelerator staff.
889 Since ELISe will act as a data source for the accelerator controls, we foresee
890 strict compliance to the given interfaces and timing definitions and will provide
891 pre-analysis, e.g., profile, luminosity and emittance information.

892 At the same time, the experimental data treatment will require complete
893 event-wise data recording at the highest possible rates in the electron tracking
894 system. The tracker will be read out by dedicated front-end electronics (e.g.
895 [96]) coupled to a flexible (FPGA, DSP, CPU based) readout system that will
896 perform the first analysis steps on-line. In such a way, a considerable data reduction
897 coming from this fixed installation within the experiment can be achieved.
898 We plan to run a trigger-less, data-driven system. The front-end acquisition
899 system will also allow for further data and background reduction by using local
900 trigger information in order to define regions of interest in the data stream.
901 The concept for the actual data readout, event building, transfer and long-term
902 storage is based on a scalable and standardized system (e.g. [97]) provided by
903 GSI/FAIR, see also [98].

904 9. Summary

905 The proposed electron-ion collider will provide a unique experimental facility
906 for FAIR. The ELISe experiment is part of the core program [99] of the FAIR
907 facility.

908 It becomes feasible due to the intense pulsed beams from the FAIR syn-
909 chrotrons, allowing for an optimized storage-ring operation. Luminosity esti-
910 mates have been presented in this paper and the collider kinematics has been
911 discussed. It turns out that the large center-of-mass energy for the electrons
912 leads to small center-of-mass angles for a particularly chosen momentum trans-
913 fer. The expected cross sections are thus sizable and will largely compensate
914 the seemingly poor luminosities achievable for collider experiments.

915 A major advantage of the ELISe facility, in addition to the analysis of elec-
916 trons, is the possibility also to fully analyze recoils and target fragments after
917 reactions. They are moving with the stored ion beam towards the first bending
918 section in the ion path following the intersection of the two storage rings. The
919 section is subsequently also used as magnetic spectrometer for the recoils.

920 The most attractive as well as challenging features of the proposed concept
921 are:

- 922 • The ELISe project pioneers electron scattering off radioactive nuclei for
923 nuclear structure studies while making use of well established heavy-ion
924 storage-ring techniques.
- 925 • The versatile ELISe experiment, will consist of three major components
926 (i) an electron spectrometer, (ii) an in-ring detection system, and (iii) a
927 luminosity monitor, which can be extended with additional detectors for
928 specific experiments.
- 929 • These basic components have been considered in this paper. They can
930 handle a wide range of different nuclear reactions and thus address numer-
931 ous physics questions. Kinematically complete measurements where the
932 electrons, the target-like recoils with their associated gammas, are mea-
933 sured with high efficiency are facilitated due to the relativistic focussing
934 (Lorentz boost). This is quite in contrast to conventional fixed-target
935 electron-scattering experiments.
- 936 • Technologically, the requirement of high resolution combined with high ac-
937 ceptance for the electron spectrometer is most demanding. Two concepts
938 for the spectrometer have been shown here, and their properties have been
939 discussed.

940 The conceptual design of a collider experiment for nuclear structure investi-
941 gations is featured in the present paper. The envisaged solutions fulfil already
942 most of the experimental requirements posed by the physics cases. In the fu-
943 ture, a more detailed design of particular components will be presented. The
944 expected gain of information will allow to perform realistic physics simulations,
945 where ELISe's physics performance can be fully explored.

946 Acknowledgements

947 The authors acknowledge financial support from the EC via the INTAS pro-
948 gramme, grants No. 03-54-6545 and 05-1000008-8272. This work was partially
949 supported by the Hessian LOEWE initiative Helmholtz International Center for
950 FAIR.

951 References

- 952 [1] NuPECC Long Range Plan 2004,
953 http://www.nupecc.org/lrp02/long_range_plan.2004.pdf;
954 http://www.nupecc.org/pub/NuPECC_Roadmap.pdf.
- 955 [2] E. Garrido, E. Moya de Guerra, Nucl. Phys. **A650** (1999) 387.
- 956 [3] E. Garrido, E. Moya de Guerra, Phys. Lett. **B488** (2000) 68.
- 957 [4] S.N. Ershov, Yad. Fiz. **67** (2004) 1877; Phys. Atomic Nuclei **67** (2004)
958 1851.

- 959 [5] Z. Wang, Z. Ren, Phys. Rev. **C 70** (2004) 034303.
- 960 [6] S.N. Ershov, B.V. Danilin, J.S. Vaagen, Phys. Rev. **C 72** (2005) 044606.
- 961 [7] A.N. Antonov, D.N. Kadrev, M.K. Gaidarov, E. Moya de Guerra, P. Sar-
962 riguren, J.M. Udias, V.K. Lukyanov, E.V. Zemlyanaya, G.Z. Krumova,
963 Phys. Rev. **C 72** (2005) 044307.
- 964 [8] C.A. Bertulani, J. Phys. (London) **G34** (2007) 315.
- 965 [9] C.A. Bertulani, Phys. Rev. **C 75** (2007) 024606.
- 966 [10] C.A. Bertulani, Phys. Rev. **C 75** (2007) 057602.
- 967 [11] S. Karataglidis, K. Amos, Phys. Lett. **B650** (2007) 148.
- 968 [12] E. Khan, M. Grasso, J. Margueron, N. Van Giai, Nucl. Phys. **A800** (2008)
969 37;
- 970 [13] X. Roca-Maza, M. Centelles, F. Salvat, X. Viñas, Phys. Rev. **C 78** (2008)
971 044332.
- 972 [14] M. Grasso, L. Gaudefroy, E. Khan, T. Niksic, J. Piekarewicz, O. Sorlin,
973 N. Van Giai, D. Vretenar, Phys. Rev. **C 79** (2009) 034318.
- 974 [15] Yu.Ts. Oganessian, O.N. Malyshev, I.N. Meshkov, V.V. Parkhomchuk,
975 P. Pokorný, A.A. Sery, S.V. Stepantsov, Ye.A. Syresin, G.M. Ter-Akopian,
976 V.A. Timakov, Z. Phys. **A341** (1992) 217.
- 977 [16] T. Katayama, T. Suda, and I. Tanihata, Phys. Scr. **T 104** (2003) 129.
- 978 [17] G. Münzenberg, J. Friese, H. Geissel, I. Meshkov, G. Schrieder, E. Syresin,
979 Nucl. Phys. **A626** (1997) 249.
- 980 [18] I. Meshkov, G. Münzenberg, G. Schrieder, E. Syresin, G.M. Ter Akopian,
981 Nucl. Inst. Meth. **A391** (1997) 224.
- 982 [19] L.V. Chulkov, G. Münzenberg, G. Schrieder, H. Simon, Phys. Scr. **T104**
983 (2003) 144.
- 984 [20] H. Simon, Nucl. Phys. **A787** (2007) 102.
- 985 [21] FAIR - Facility for Antiproton and Ion Research,
986 http://www.gsi.de/fair/index_e.html.
- 987 [22] T. Suda, M. Wakasugi, Prog. Part. Nucl. Phys. **55** (2005) 417.
- 988 [23] A. Richter, Nucl. Phys. **A751** (2005) 3c.
- 989 [24] B. Jonson, Phys. Rep. **389** (2004) 1.
- 990 [25] T.W. Donnelly, J.D. Walecka, Ann. Rev. Nucl. Part. Sci. **25** (1975) 329.

- 991 [26] E. Moya de Guerra, Phys. Rep. **138** (1986) 293.
- 992 [27] J. Heisenberg, H.P. Blok, Ann. Rev. Nucl. Part. Sci. **33** (1983) 569.
- 993 [28] M. N. Harakeh and A. van der Woude, Giant Resonances, (Clarendon Press,
994 Oxford, 2001).
- 995 [29] D. Drechsel, M.M. Giannini, Rep. Prog. Phys. **52** (1989) 1083.
- 996 [30] D.R. Yennie, D.G. Ravenhall, and R.N. Wilson, Phys. Rev. **95** (1954) 500
997 (and references therein).
- 998 [31] H. de Vries, C.W. de Jager, C. de Vries, At. Data Nucl. Data Tables **36**
999 (1987) 495.
- 1000 [32] G. Fricke, C. Bernhardt, K. Heilig, L.A. Schaller, L. Schellenberg,
1001 E.B. Shera, C.W. de Jager, At. Data Nucl. Data Tables **60** (1995) 177.
- 1002 [33] J. Friedrich, N. Voegler, Nucl. Phys. **A373** (1982) 192.
- 1003 [34] I. Angeli, R.J. Lombard, Z. Phys. **A 324** (1986) 299.
- 1004 [35] J. Friedrich, N. Voegler, P.-G. Reinhard, Nucl. Phys. **A459** (1986) 10.
- 1005 [36] G.S. Anagnostatos, A.N. Antonov, P. Ginis, J. Giapitzakis, M.K. Gaidarov,
1006 J. Phys. (London) **G25** (1999) 69.
- 1007 [37] M. Bender, K. Rutz, P.-G. Reinhard, J.A. Maruhn, W. Greiner, Phys. Rev.
1008 **C 60** (1999) 034304.
- 1009 [38] J. Decharge, J.-F. Berger, K. Dietrich, M.S. Weiss, Phys. Lett. **B451** (1999)
1010 275.
- 1011 [39] A.V. Afanasjev, S. Frauendorf, Phys. Rev. **C 71** (2005) 024308.
- 1012 [40] W.A. Richter, B.A. Brown, Phys. Rev. **C 67** (2003) 034317.
- 1013 [41] J. Friedrich, N. Voegler, Phys. Rev. Lett. **47** (1981) 1385.
- 1014 [42] P. Sarriguren, E. Moya de Guerra, and A. Escuderos, Nucl. Phys. **A658**
1015 (1999) 13; Phys. Rev. **C 64** (2001) 064306.
- 1016 [43] V.K. Lukyanov, E.V. Zemlyanaya, D.N. Kadrev, A.N. Antonov,
1017 K. Spasova, G.S. Anagnostatos, and J. Giapitzakis, Particles and Nuclei,
1018 Letters, No. 2[111] (2002) 5; Bull. Rus. Acad. Sci., Phys. **67** (2003) 790.
- 1019 [44] M. Nishimura, E. Moya de Guerra, and D.W.L. Sprung, Nucl. Phys. **A435**
1020 (1985) 523 ; J.M. Udias, M.Sc. Thesis, Universidad Autonoma de Madrid
1021 (unpublished) (1987).
- 1022 [45] T. de Forest, Jr. and J.D. Walecka, Adv. Phys. **15** (1966) 1.

- 1023 [46] G.D. Alkhazov, V.V. Anisovich, and P.E. Volkovyckii, *Diffractional Inter-*
1024 *action of Hadrons with Nuclei at High Energies*, Nauka, Leningrad (1991)
1025 94.
- 1026 [47] V.V. Burov and V.K. Lukyanov, Preprint JINR (1977) R4-11098, Dubna;
1027 V.V. Burov, D.N. Kadrev, V.K. Lukyanov, and Yu.S. Pol', Phys. At. Nu-
1028 clei **61** No.4 (1998) 525.
- 1029 [48] J. Friedrich and Th. Walcher, Eur. Phys. J. **A17** (2003) 607.
- 1030 [49] G.G. Simon, Ch. Schmitt, F. Borkowski, and V.H. Walther,
1031 Nucl. Phys. **A333** (1980) 381.
- 1032 [50] S. Galster, H. Klein, J. Moritz, K.H. Schmidt, D. Wegener, and J. Bleck-
1033 wenn, Nucl. Phys. **B32** (1971) 221.
- 1034 [51] H. Chandra and G. Sauer, Phys. Rev. **C 13** (1976) 245.
- 1035 [52] G.R. Satchler, Nucl. Phys. **A472** (1987) 215.
- 1036 [53] A. Krasznahorkay, H. Akimune, A.M. van den Berg, N. Blasi, S. Brand-
1037 denburg, M. Csatlos, M. Fujiwara, J. Gulyas, M.N. Harakeh, M. Hunyadi,
1038 M. de Hoo, Z. Mate, D. Sohler, S.Y. van der Werf, H.J. Wörtche, L. Zolnai,
1039 Nucl. Phys. **A731** (2004) 224.
- 1040 [54] K. Langanke, G. Martinez-Pinedo, P. von Neumann-Cosel, A. Richter,
1041 Phys. Rev. Lett. **93** (2004) 202501.
- 1042 [55] U. Zurmühl, P. Rullhusen, F. Smend, M. Schumacher, H.G. Börner,
1043 S.A. Kerr, Phys. Lett. **B 114** (1982) 99; Z. Phys. **A314** (1983) 171.
- 1044 [56] N. Tsoneva, H. Lenske, Prog. Part. Nucl. Phys., **59** (2007) 317.
- 1045 [57] S. Goriely, Phys. Lett. **B460** (1998) 136.
- 1046 [58] J.J. Cowan, F.-K. Thielemann, J.W. Truran, Phys. Rep. **208** (1991) 267.
- 1047 [59] Th. Weber, R.D. Heil, U. Kneissl, W. Wilke, Th. Kihm, K.T. Knöpfle,
1048 H.J. Emrich, Nucl. Phys. **A510** (1990) 1.
- 1049 [60] P.K.A. de Witt Huberts, J. Phys. **G16** (1990) 507.
- 1050 [61] J. Wesseling, C.W. de Jager, L. Lapikas, H. de Vries, M.N. Harakeh,
1051 N. Kalantar-Nayestanaki, L.W. Fagg, R.A. Lindgren, D. Van Neck,
1052 Nucl. Phys. **A547** (1992) 519.
- 1053 [62] G.J. Kramer, H.P. Blok, L. Lapikas, Nucl. Phys. **A679** (2001) 267.
- 1054 [63] D. Van Neck, M. Waroquier, J. Ryckebusch, Nucl. Phys. **A530** (1991) 347.
- 1055 [64] V.R. Pandharipande, I. Sick, and P.K.A. de Witt Huberts, Rev. Mod. Phys.
1056 **69** (1997) 981.

- 1057 [65] T. Otsuka, T. Suzuki, R. Fujimoto, H. Grawe, and Y. Akaishi,
1058 Phys. Rev. Lett. **95** (2005) 232502.
- 1059 [66] O. Benhar, D. Day, I. Sick, Rev. Mod. Phys. **80** (2008) 189.
- 1060 [67] C. Barbieri, D. Rohe, I. Sick, L. Lapikas, Phys. Lett. **B608** (2005) 47.
- 1061 [68] D. Rohe, A1 and A3 collaboration, Eur. Phys. J. **A28** (2006) 29.
- 1062 [69] J.D. Bjorken, S.K. Mtingwa, Particle Accelerators **13** (1983) 115.
- 1063 [70] E.L. Saldin, E.A. Schneidmiller, M.V. Yurkov, Nucl. Inst. Meth. **A375**
1064 (1996) 336.
- 1065 [71] M.V. Ricciardi, S. Lukić, A. Kelić, K.-H. Schmidt, M. Veselsky,
1066 Eur. Phys. J. Spec. Top. **150** (2007) 321.
- 1067 [72] H. Geissel, H. Weick, M. Winkler, G. Münzenberg, V. Chichkine, M. Yavor,
1068 T. Aumann, K.H. Behr, M. Böhmer, A. Brünle, K. Burkard, J. Benlliure,
1069 D. Cortina-Gil, L. Chulkov, A. Dael, J.-E. Ducret, H. Emling, B. Franczak,
1070 J. Friese, B. Gastineau, J. Gerl, R. Gernhäuser, M. Hellström, B. Jonson,
1071 J. Kojouharova, R. Kulesa, B. Kindler, N. Kurz, B. Lommel, W. Mit-
1072 tig, G. Moritz, C. Mühle, J.A. Nolen, G. Nyman, P. Roussel-Chomaz,
1073 C. Scheidenberger, K.-H. Schmidt, G. Schrieder, B.M. Sherrill, H. Si-
1074 mon, K. Sümmerer, N.A. Tahir, V. Vysotsky, H. Wollnik and A.F. Zeller,
1075 Nucl. Inst. Meth. **B204** (2003) 71.
- 1076 [73] K.-H. Schmidt, E. Hanelt, H. Geissel, G. Münzenberg, J.P. Dufour ,
1077 Nucl. Inst. Meth. **A260** (1987) 287.
- 1078 [74] C. J. Benesh, B. C. Cook, and J. P. Vary, Phys. Rev. **C 40** (1998) 1198.
- 1079 [75] C. Scheidenberger, H. Geissel, H.H. Mikkelsen, F. Nickel, T. Brohm, H. Fol-
1080 ger, H. Irnich, A. Magel, M.F. Mohar, G. Münzenberg, M. Pfützner,
1081 E. Roeckl, I. Schall, D. Schardt, K.-H. Schmidt, W. Schwab, M. Steiner,
1082 Th. Stöhlker, K. Sümmerer, D.J. Vieira, B. Voss, and M. We-
1083 ber, Phys. Rev. Lett. **73** (1994) 50; C. Scheidenberger, H. Geis-
1084 sel, H.H. Mikkelsen, F. Nickel, S. Czajkowski, H. Folger, H. Irnich,
1085 G. Münzenberg, W. Schwab, Th. Stöhlker, T. Suzuki, and B. Voss,
1086 Phys. Rev. Lett. **77** (1996) 3987; N. Iwasa, H. Geissel, G. Münzenberg,
1087 C. Scheidenberger, Th. Schwab, H. Wollnik, Nucl. Inst. Meth. **B126** (1997)
1088 284.
- 1089 [76] S.Y.F. Chu, L.P. Ekström and R.B. Firestone The Lund/LBNL Nuclear
1090 Data Search Version 2.0, February (1999),
1091 <http://nucldata.nuclear.lu.se/nucldata/toi/listnuc.asp?sql=&A1=1& A2=238>.
- 1092 [77] M. Steck, C. Dimopoulou, A. Dolinskii, F. Nolden, Proceedings of PAC07,
1093 Albuquerque, New Mexico, USA (2007) 1425.

- 1094 [78] J. Eichler, Th. Stöhlker, Phys. Rep. **439** (2007) 1.
- 1095 [79] Th. Stöhlker, T. Ludziejewski, H. Reich, F. Bosch, R.W. Dunford, J. Eich-
1096 ller, B. Franzke, C. Kozhuharov, G. Menzel, P.H. Mokler, F. Nolden, P. Ry-
1097 muza, Z. Stachura, M. Steck, P. Swiat, A. Warczak, and T. Winkler,
1098 Phys. Rev. **A 58** (1998) 2043.
- 1099 [80] J. Eichler and Th. Stöhlker, Hyperfine Int. **114** (1998) 277.
- 1100 [81] MEFIT B. Dreher, K. Merle, MEFCAL, University of Mainz, unpub-
1101 lished.
- 1102 [82] H. Diesener, U. Helm, G. Herbert, V. Huck, P. von Neumann-Cosel, C. Ran-
1103 gacharyulu, A. Richter, G. Schrieder, A. Stascheck, A. Stiller, J. Rycke-
1104 busch, J. Carter, Phys. Rev. Lett. **72** (1994) 1994; H. Diesener, U. Helm,
1105 P. von Neumann-Cosel, A. Richter, G. Schrieder, A. Stascheck, A. Stiller,
1106 J. Carter, Nucl. Phys. **A696** (2001) 272.
- 1107 [83] K.I. Blomqvist, W.U. Boeglin, R. Böhm, M. Distler, R. Edelhoff,
1108 J. Friedrich, R. Geiges, P. Jennewein, M. Kahrau, M. Korn, H. Kramer,
1109 K.W. Krygier, V. Kunde, A. Liesenfeld, H. Merkel, K. Merle, U. Müller,
1110 R. Neuhausen, E.A.J.M. Offermann, Th. Pospischil, A.W. Richter, G. Ros-
1111 ner, P. Sauer, S. Schardt, H. Schmieden, A. Wagner, Th. Walcher, S. Wolf,
1112 Nucl. Inst. Meth. **A403** (1998) 263.
- 1113 [84] W. Brooks and CLAS Collaboration, Nucl. Phys. **A663** (2000) 1077.
- 1114 [85] J. Friese, for the HADES collaboration, Nucl. Phys. **A654** (1999) 1017c.
- 1115 [86] The BLAST Collaboration, Technical Design Report (1997),
1116 <http://blast.lns.mit.edu/BlastNotes/>; R. Alarcon and BLAST Collabora-
1117 tion, Nucl. Phys. **A663** (2000) 1111.
- 1118 [87] The BELLE Collaboration, KEK Progress Report 2000-4,
1119 <http://beauty.bk.tsukuba.ac.jp/belle/nim/>; Nucl. Inst. Meth. **A479** (2002)
1120 117.
- 1121 [88] Rare Isotope Physics at Storage Rings,
1122 Int. Workshop, 2002, Hirschegg, Austria,
1123 <http://www-win.gsi.de/frs/meetings/hirschegg/Talks/Thursday/Blomquist.pdf>;
1124 <http://www-win.gsi.de/frs/meetings/hirschegg/Talks/Thursday/Kato.pdf>.
- 1125 [89] V. Bondarenko, B. Dolgoshein, V. Grigoriev, O. Kondratiev, A. Medvedev,
1126 S. Pavlenko, M. Potekhin, A. Romaniouk, V. Sosnovtsev, V. Tcherniatine,
1127 S. Muraviev, Nucl. Inst. Meth. **A327** (1993) 386.
- 1128 [90] J.V. Allaby, W.W. Ash, H.R. Band, L.A. Baksay, H.T. Blume, M. Bosman,
1129 T. Camporesi, G.B. Chadwick, S.H. Clearwater, R.W. Coombes,
1130 M.C. Delfino, R. de Sangro, W.L. Faissler, E. Fernández, W.T. Ford,
1131 M.W. Gettner, G.P. Goderre, Y. Goldschmidt-Clermont, B. Gottschalk,

- 1132 D.E. Groom, B.K. Heltsley, R.B. Hurst, J.R. Johnson, H.S. Kaye,
 1133 K.H. Lau, T.L. Lavine, H.Y. Lee, R.E. Leedy, S.P. Leung, I. Lippi,
 1134 E.C. Loh, H.L. Lynch, A. Marini, J.S. Marsh, T. Maruyama, R.L. Messner,
 1135 O.A. Mayer, S.J. Michalowski, S. Morcos, J.H. Moromisato, R.M. Morse,
 1136 L.J. Moss, F. Muller, H.N. Nelson, I. Peruzzi, M. Piccolo, R. Prepost,
 1137 J. Pyrlik, N. Qi, A.L. Read, Jr., K. Rich, D.M. Ritson, F. Ronga,
 1138 L.J. Rosenberg, W.D. Shambroom, J.C. Sleeman, J.G. Smith, J.P. Venuti,
 1139 P.G. Verdini, E. von Goeler, H.B. Wald, R. Weinstein, D.E. Wisner, and
 1140 R.W. Zdarko, Nucl. Inst. Meth. **A281**(1989) 291.
- 1141 [91] A1 collaboration, <http://wwwa1.kph.uni-mainz.de/A1/vdc.html>.
- 1142 [92] V. Kouznetsov, A. Lapik, S. Churikova, B. Girolami, D. Karapetiantz,
 1143 Yu. Malyukin, V. Nedorezov, A. Turinge, Yu. Vorobiev, V. Abramov,
 1144 A. D'Angelo, D. Moricciani, L. Nicoletti, Yu. Ranyuk, C. Schaerf,
 1145 Nucl. Inst. Meth. **A487** (2002) 396.
- 1146 [93] H.W. Koch, J.W. Motz, Rev. Mod. Phys. **31** (1959) 920.
- 1147 [94] C.J. Bocchetta, A. Wrulich, Nucl. Inst. Meth. **278** (1989) 807.
- 1148 [95] K. Mengel, R. Novotny, W. Doring, V. Metag, R. Beck, H. Ströher, IEEE
 1149 Trans. Nucl. Sci. **45** (1998) 681.
- 1150 [96] A.S. Brogna, S. Buzzetti, W. Dabrowski, T. Fiutowski, B. Gebauer,
 1151 M. Klein, C.J. Schmidt, H.K. Soltveit, R. Szczygiel, U. Trunk
 1152 Nucl. Inst. Meth. **A568** (2006) 301.
- 1153 [97] H.G. Essel, J. Hoffmann, N. Kurz, R.S. Mayer, W. Ott, D. Schall,
 1154 IEEE Trans. Nucl. Sci. **43** (1996) 132;
 1155 H.G. Essel, N. Kurz, IEEE Trans. Nucl. Sci. **47** (2000) 337.
- 1156 [98] Synergy Group for Front-End Electron-
 1157 ics, Data Acquisition and Controls (SGFDC)
 1158 <http://www.gsi.de/fair/experiments/NUSTAR/WGs/FEE-DAQ/>.
- 1159 [99] FAIR Baseline Technical Report Eds., H.H. Gutbrod, I. Augustin,
 1160 H. Eickhoff, K.-D. Groß, W.F. Henning, D. Krämer, G. Walter, (2006)
 1161 <http://www.gsi.de/fair/reports/btr.html>.